2013

STUDIES OF ORGANIC COMPOUNDS SPREADING OVER HIGH ENERGY SURFACES

Lingbo Lu
University of Kentucky, lingbo.lu@gmail.com

STUDENT AGREEMENT:

I represent that my thesis or dissertation and abstract are my original work. Proper attribution has been given to all outside sources. I understand that I am solely responsible for obtaining any needed copyright permissions. I have obtained and attached hereto needed written permission statements(s) from the owner(s) of each third-party copyrighted matter to be included in my work, allowing electronic distribution (if such use is not permitted by the fair use doctrine).

I hereby grant to The University of Kentucky and its agents the non-exclusive license to archive and make accessible my work in whole or in part in all forms of media, now or hereafter known. I agree that the document mentioned above may be made available immediately for worldwide access unless a preapproved embargo applies.

I retain all other ownership rights to the copyright of my work. I also retain the right to use in future works (such as articles or books) all or part of my work. I understand that I am free to register the copyright to my work.

REVIEW, APPROVAL AND ACCEPTANCE

The document mentioned above has been reviewed and accepted by the student's advisor, on behalf of the advisory committee, and by the Director of Graduate Studies (DGS), on behalf of the program; we verify that this is the final, approved version of the student's dissertation including all changes required by the advisory committee. The undersigned agree to abide by the statements above.

Lingbo Lu, Student

Dr. Yuguang Cai, Major Professor

Dr. Dong-sheng Yang, Director of Graduate Studies

STUDIES OF ORGANIC COMPOUNDS SPREADING OVER HIGH ENERGY SURFACES

DISSERTATION

A dissertation submitted in partial fulfillment of the
requirements for the degree of Doctor of Philosophy in the
College of Art and Science
at the University of Kentucky

By
Lingbo Lu

Lexington, Kentucky

Director: Dr. Yuguang Cai, Professor of Department of Chemistry

Lexington, Kentucky

2013

ABSTRACT OF DISSERTATION

STUDIES OF ORGANIC COMPOUNDS
SPREADING OVER HIGH ENERGY SURFACES

Spreading plays an important role in coating, lubrication, printing and etc. During the spreading process, a liquid thin film forms prior to the expansion of a liquid drop. This thin film is called a precursor film. It not only changes the spreading mechanism, but impacts the wettability of a liquid. Early studies on the precursor films showed the films were stacked in a terraced structure, and the radius of each layer of the films was proportional to the square root of time. Optical techniques such as ellipsometry, X-ray diffraction and X-ray reflectivity solved the conformations of liquid molecules at the interfaces. However, the conformations of the interfacial molecules have rarely been correlated with their positions at the interface. In addition, the properties of the precursor films have not been fully studied yet.

In this dissertation, two kinds of organic compounds, hexatriacontane (C36) and 1-butyl-3-methylimidazolium ([Bmim][Cl]), are proposed to be spread over octadecyltrichlorosilane partially degraded (OTSpd) patterned surfaces. Once organic molecules flow over such OTSpd surfaces, the liquids are limited within the patterned area. Characterized by atomic force microscopy (AFM), the structures and chemical identities and the formation mechanism of the precursor films are resolved thereafter.

The precursor films formed by both compounds, C36 and [Bmim][Cl], were observed in a bilayer structure in that the molecules close to the solid substrate had different orientation from the molecules close to the air. They were called parallel layers and standing-up layers, respectively. The parallel layers of C36 formed prior to the standing-up layers through the vapor phase transport. In addition, the parallel layers were found more stable thermodynamically and the standing-up layers were more stable mechanically. The frictional study of C36 showed the standing-up layers could hold 0.49GPa pressure. The orientation of [Bmim][Cl] molecules were impacted by the polarities of the solid substrates.

The achievements in this dissertation not only resolve the properties of the precursor films of two organic compounds, but provide a general method for the further studies of the precursor films.

KEYWORDS: Spreading, Precursor Film, Surface Chemistry, Patterning, Atomic Force Microscopy

Lingbo Lu

Student's Signature

8/01/2013

Date

STUDIES OF ORGANIC COMPOUNDS SPREADING OVER HIGH ENERGY SURFACES

By

Lingbo Lu

Dr. Yuguang Cai

Director of Dissertation

Dr. Dong-sheng Yang

Director of Graduate Studies

8/01/2013

ACKNOWLEDGEMENTS

My first and sincere appreciation must go to Dr. Yuguang Cai, my advisor for all I have learned from him and for his continuous help and support in all stages of this dissertation. I would also like to express my deep gratitude to my academic committee, Dr. Dong-Sheng Yang, Dr. Carolyn P. Brock and Dr. J. Todd Hastings whose guidance and suggestions were invaluable to me.

In addition, I would like to thank Dr. Wen Liu for the discussion about the principles of wetting. His expertise broadened my knowledge and inspired me.

In the end, I want to express my greatest appreciation to my parents for always believing in me, for their continuous love and for their supports in my decisions. Without them, I could not make it here.

TABLE OF CONTENTS

LIST OF TABLES

LIST OF FIGURES

Chapter One

INTRODUCTION

1.1 Background

Wetting is a key phenomenon in life. In some applications such as painting, printing and coating, complete wetting is highly desired. However, in other applications, such as oil extraction and surface protection, wetting is to be avoided. Understanding the process and the principles of wetting may help the development of specific products for those applications.

Scientifically, wetting is defined as a process that a liquid replaces another liquid that originally covers a solid substrate.[1] It was initially described with the contact angle, θ. In 1802, Young pointed out the projection of the different surface tensions acting on the contact line on the solid plane provided the equilibrium condition of the liquid drop,[2] known as Young's equation:

$$\gamma_{SV} = \gamma_{SL} + \gamma_{LV} \cos\theta \tag{1.1}$$

where γ_{SV}, γ_{SL} and γ_{LV} are the surface tensions of solid/vapor interface, solid/liquid interface and liquid/vapor interface, respectively; θ is the contact angle which is thus fixed by the nature of different phases. Although contact angles succeed in describing the wettability of liquids over solid surfaces, namely hydrophilicity and hydrophobicity, they fail to match the shapes of the liquid drops near the contact line in micro-scale.[3] In 1919, Hardy first observed that at the contact line, the liquid drop did not gradually decrease to

a monolayer of molecules, instead, there existed a thin film whose size was beyond the radius of the liquid drop.[4] He also suggested that no matter what substrate a liquid drop spread over, a one-micron thick invisible film should form prior to the expansion of the liquid.[5]

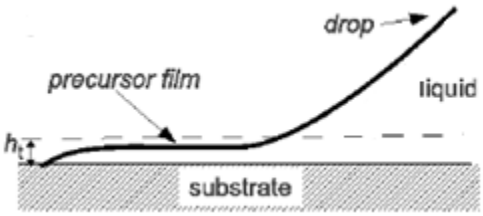

Figure 1.1. Illustration of the precursor films of a liquid drop over a solid surface.[4]

This "invisible film" was later called a precursor film as shown in Figure 1.1. Further effort on studying the wetting phenomenon made by Deryagin confirmed the existence of the precursor films.[6, 7] He proposed that a "disjoining pressure" working from 30Å to 1μm above the substrate surface resulted in thickening the film of a liquid.[3] This "disjoining pressure" was found to be van der Waals force for organic liquids and electronic interaction for water after 20 years.[8]

With the development of the optical technologies, the precursor films were, therefore, able to be systematically studied in 1960s. The thickness of the films were confirmed to be less than 1000 Å with ellipsometer and interference microscopy in 1964.[9] In 1986, Ausserre obtained an image of polydimethylsiloxane (PDMS) precursor film with polarized reflective microscopy (ellipsometric reflective microscopy).[10] He inferred that the film was about a few hundred angstroms thick. At the same time, de Gennes and his colleagues resolved the "disjoining pressure" equation and pointed out that van der Waals force strongly impacted the precursor films 800 Å above the solid substrates.[11]

Another significant discovery made by Cazabat showed that the thicknesses of the precursor films were not uniform. The films were composed of several layers of molecules, and each layer expanded at different speed. Thus, the film was in a terraced structure.[12] Such a terraced structure was later observed in various spreading experiments.[13-15]

Although pioneer works have unveiled the geometric properties and dynamic properties of various precursor films, seldom have researches focused on the structures of the precursor films on molecular level. On one aspect, the spot size of a laser beam is normally 6 orders of magnitude larger than a single molecule. It cannot be focused on single molecules. On the other aspect, the transition of the orientation of the molecules at the solid/film interface to film/liquid interface is hard to be distinguished by optical methods. Some efforts for exploring the structures of the molecules at the interfaces have been made by using X-ray techniques, but none of those results has been associated with the precursor films. The knowledge of the precursor films and the structures of the molecules at the interfaces need to be associated for further understanding the wetting processes.

1.2 Objective

The objective of my study in this dissertation is to investigate the interfacial properties of organic films nearest the solid substrates. An octadecyltrichlorosilane partially degraded (OTSpd)-patterned surface is applied and the organic molecules, hexatriacontane and 1-butyl-3methylimidazolium chloride, are spread over the patterned

surfaces. Both physical and chemical properties of the thin film are characterized by atomic force microscopy (AFM).

The solid substrates used for spreading experiments are normally silicon, graphene and gold, which are uniform and featureless. These surfaces are insufficient to extract the effects of gas phase transports from liquid flow and are incapable to reflect the different functional groups of the molecules of the precursor films. Based on the previous works, a new approach is proposed to observe the precursor films by using OTSpd-patterned surfaces and AFM. An OTSpd pattern which will be discussed in chapter three is terminated with carboxylic acid groups, which have strong affinities to organic molecules. The surface surrounding the OTSpd patterns is terminated with methyl groups that inhibit the flow of organic molecules. Thus, the gas phase transport and liquid flow would be separated.

Furthermore, OTSpd-patterned surfaces provide two different chemical identities: methyl groups terminated surfaces and carboxylic acid groups terminated surfaces. By comparing phase signals of AFM measurements, I will distinguish the orientations of the molecules of the precursor films, thus exploring the localized structures of precursor films will be explored.

Finally, the stability of precursor films is the key for their applications. Not only do the films directly contact the solid surface, but they change the surface properties that impact the liquid expansion. By annealing the samples, I will explore the movement of the liquid molecules and compare the stabilities of the different layers of the precursor films. By wiping the precursor film with an AFM tip, I will also compare the mechanical properties of the precursor films.

1.3 Organization

In this dissertation, organic compounds spreading over OTSpd patterned surfaces are studied. The main research methods and results are discussed sequentially in the following chapters. The relationship between the chapters is demonstrated in Figure 1.2.

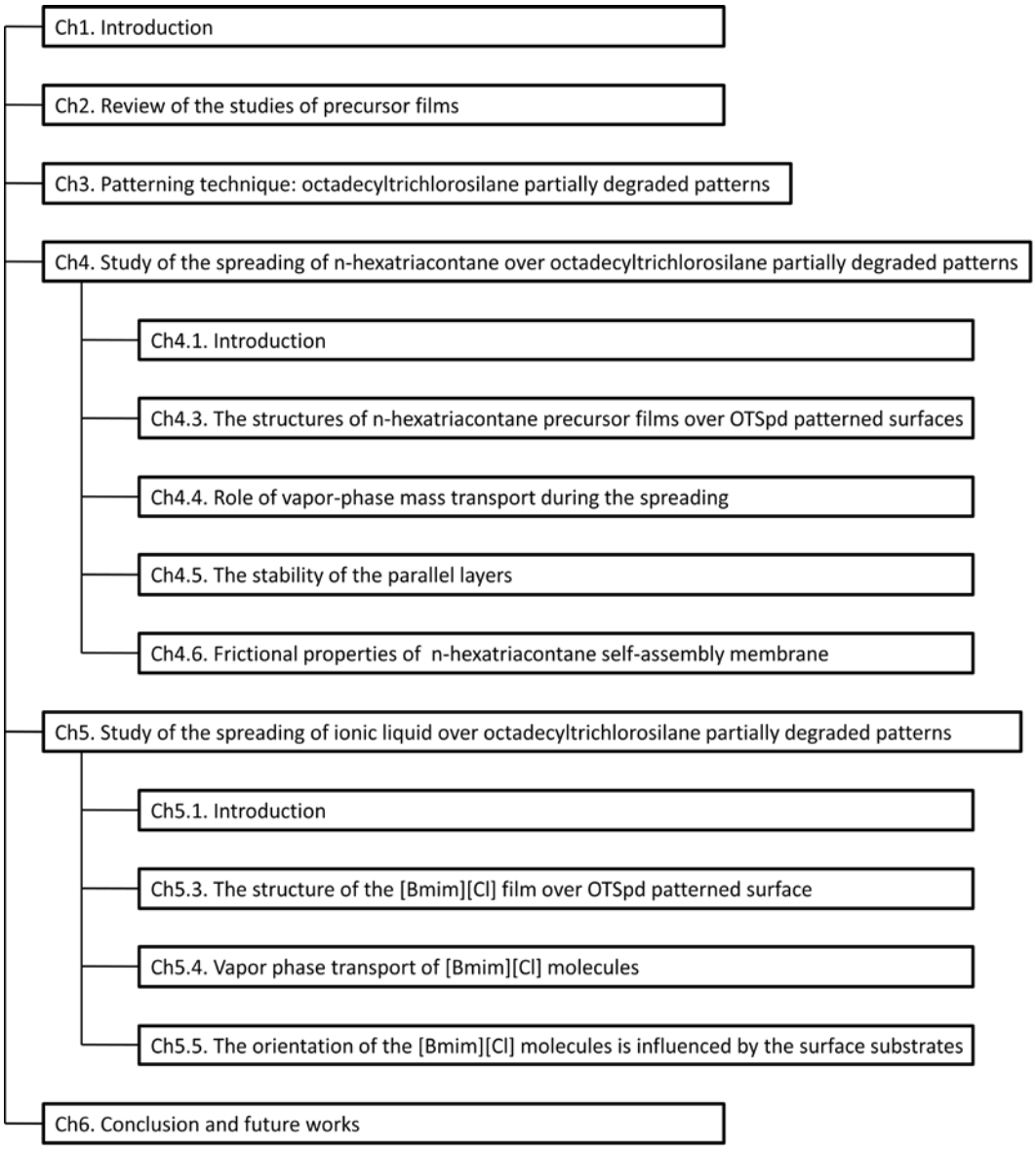

Figure 1.2. Organization of the dissertation

In Chapter 1, the research background, objective, and organization of this dissertation are presented.

In Chapter 2 some of the previous studies of precursor films are summarized with respect to different methods, and different compounds, such as alkane, polydimethylsiloxane, 1-butyl-3methylimidazolium chloride etc. The sample preparation and detection methods are included.

The preparation and characterization of OTSpd patterns are discussed in Chapter 3. OTSpd patterns are the fundamental element of this dissertation. All the spreading experiments are conducted on the patterned surfaces. An OTSpd patterned surface is made from octadecyltrichlorosilane (OTS) self-assembly membrane (SAM) by local probe oxidation lithography method. The thickness of an OTS SAM is characterized by ellipsometer and the depth of OTSpd patterns is measured by AFM. Furthermore, the terminal carboxylic acid groups of an OTSpd surface are confirmed by the reaction with 1-pyrenyldiazomethane (PDAM), which specifically binds with carboxylic acid groups.

Based on the work discussed in Chapter 3, organic liquids are to be spread over OTSpd patterns. The results are presented and discussed in Chapter 4 and Chapter 5.

In Chapter 4 n-hexatriacontane (C36) is chosen as a typical volatile compound. Based on the height measurements and phase signals, the orientations of the molecules composing the precursor films over OTSpd patterns are identified first. Then, in section 4.4, the path for the liquid flow is intentionally inhibited by OTS surface due to its low surface tension, and the role of vapor phase transport of the molecules is investigated. Finally, by heating and wiping the precursor films, the stabilities of the films are explored.

In Chapter 5 1-butyl-3methylimidazolium chloride is used as a typical nonvolatile compound. With the same approaches described in Chapter 4, the structures of the precursor films, the effects of the vapor phase transport and the mechanical properties of the precursor films are also studied. The coefficients of friction of 1-butyl-3methylimidazolium chloride surface, C36 surface and OTSpd surface are compared to address the adsorption of different compounds over the surfaces with different dipoles.

Lastly, the main discoveries are concluded in Chapter 6, and the future works for the study of precursor films are proposed.

Chapter Two

REVIEW OF THE STUDIES OF PRECURSOR FILMS

The precursor film is a thin layer of molecules that spread prior to the expansion of a liquid drop as shown in Figure 1.1. Since the precursor films change both physical properties and chemical properties of the solid substrates,[4, 11] they have drawn a lot of attention. Unfortunately, the discoverer Hardy was unable to conceive a mechanism by which the film was pushed out from the liquid drop.[5] Later, Bangham and Saweris figured out that the formation of precursor films may occur with or without the vapor of the liquid molecules.[16] Therefore, the conclusion was that the precursor films can be formed by both the diffusion of molecules along the solid surfaces[17] and the evaporation/condensation mechanism.[18]

Recently, studies are mainly focused on the dynamic properties and the geometric properties of the precursor films. The methods include theoretical evaluation, computational simulation, and experimental observation. In this chapter, I will briefly discuss the results from these methods.

2.1 Theoretical study of precursor films

The theoretical derivation of the precursor films employs the principles of fluid dynamics.[1, 3, 4, 11, 19] The geometric properties of the precursor films are governed by the mass conservation and the balance of the interfacial forces.

For a one-dimensional uniform film model, the gravitational conditions and the "disjoint pressure" are balanced with the surface tensions of the solid substrate and the liquid and the vapor at the edge of the precursor film,[1] as shown in equation 2.1:

$$G(h) + P(h) = S \tag{2.1}$$

where G describes gravitational and hydrostatic effects of the film; P describes the role of long-range forces; S is the spreading coefficient. Both G and P are the functions with respect to the thickness of the film, h.

The effects of gravitation and hydrostatics can be written as:

$$G(h) = \frac{1}{2}\rho g h^2 + \rho g h H \tag{2.2}$$

where ρ is the density difference between the liquid and the vapor, g is the gravitational acceleration, and H depends on the types of wetting. A classical equation describing the van der Waals force (Π) in terms of the gravitational parameters is shown in equation 2.3:[8, 20]

$$\Pi(h) = \rho g h + \rho g H \tag{2.3}$$

By substituting equation 2.3 to equation 2.2, I can obtain equation 2.4:

$$G(h) = h\Pi(h) - \frac{1}{2}\rho g h^2 \tag{2.4}$$

Therefore, equation 2.1 can be re-written as:

$$P(h) + h\Pi(h) - \frac{1}{2}\rho g h^2 = S \tag{2.5}$$

Normally, the thickness of a precursor film is less than 100 nm, while the value of S is much larger than 0 erg/cm^2. Thus, the gravitational term is completely negligible. Consequently, an approximation of equation 2.5 is:

$$P(h) + h\Pi(h) = S \tag{2.6}$$

Since $\Pi = -\mathrm{dP}/\mathrm{dh}$ and $P = A/(12\pi h^2)$, Π can be solved as:[1, 21]

$$\Pi(h) = \frac{A}{6\pi h^3} \tag{2.7}$$

where A is Hamaker constant. Substituting both P and Π into equation 2.6, the thickness of the film comes out to be:

$$h = \sqrt{\frac{A}{4\pi S}} \tag{2.8}$$

This result infers the thickness of the precursor film is dependent on the spreading coefficient. In particular, the bigger the spreading coefficient, the thinner and larger the precursor film.

The spreading dynamics is controlled by the Navier-Stokes momentum equation and the continuity equation. With the lubrication approximation[22, 23] that the length of the film is much larger than its thickness, the hydrodynamic properties of the film are governed by continuity equation:

$$\frac{\partial h}{\partial t} = -\frac{\partial}{\partial x}(hU) \tag{2.9}$$

and Navier-Stokes equation, equilibrium of the momentum:[4, 23-25]

$$\eta U = \frac{h^2}{3}\frac{\partial}{\partial x}\left(\gamma_{LV}\frac{\partial^2 h}{\partial x^2} + \Pi(h)\right) \tag{2.10}$$

where h is the thickness of the precursor film; γ_{LV} is the surface tension of liquid/vapor interface; η is the viscosity of the liquid; U is the spreading velocity along x-direction; Π is the "disjoint pressure".

In a simple case, the spreading of the precursor film is dominated by van der Waals force. Thus the surface tension term on the right side of equation 2.10 is ignored. Substituting the simplified equation 2.10 to equation 2.9 yields:

$$\frac{\partial h}{\partial t} = \frac{\partial}{\partial x}\left[\left(-\frac{h^3}{3\eta}\frac{\partial}{\partial h}\Pi(h)\right)\frac{\partial h}{\partial x}\right] \tag{2.11}$$

where $-\frac{h^3}{3\eta}\frac{\partial}{\partial h}\Pi(h)$ is denoted as the diffusion coefficient D(h) and D(h) is independent to the radius of the precursor film, x. Solving the equation 2.12

$$\frac{\partial h}{\partial t} = \frac{\partial}{\partial x}\left[D(h)\frac{\partial h}{\partial x}\right] \tag{2.12}$$

leads to the result of x to be proportional to $\sqrt{Dt}$.[21, 26] It means the precursor film expands with its radius proportional to the square root of time. This relationship is called $\sqrt{t}$ law.

Although these derivations conceptually describe the shape and the spreading kinetics of the precursor films, it is still hard to solve the problems of the liquids with volatile impurities and surfactants and to describe the terrace-structured precursor films observed in 1989.[12]

2.2 Computational simulation of precursor films

Monte Carlo (MC) simulations and molecular dynamics (MD) simulations are the mostly used computational methods. They estimate the mesoscopic and macroscopic properties from the motions of single molecules. In Ising's MC study,[27] he modeled the spreading process on a three-dimensional box with up to 24000 liquid particles. Each particle was impacted by its nearest-neighboring particles and the solid substrate. By changing the ratio of particle-particle interactions and particle-substrate interactions, and by keeping the thermal energy low (low vapor pressure), he found the molecules formed

a terrace-shaped precursor film and the expansion rate of each layer followed the $\sqrt{t}$ law. Moreover, by increasing the number of particles from 500 to 24000, he found out that those conclusions still held. During the same time, De Conink used MC simulations to study the influence of vapor phase condensation during the formation of precursor films. By considering the liquid/vapor and vapor/substrate interactions, his study showed that for a single liquid, the precursor film could be either uniform or in terraced structure due to different substrates.[28, 29]

Compared to MC simulations, a MD simulation includes the information of each individual molecules in the system. It allows researchers to vary the liquid molecules. As the trade-off, the MD simulations require extensive computational time and extremely large computer resources. The first successful MD simulation was done in 1991.[30] Yang chose a diatomic particle as the liquid compound and approximated the inter particle interactions as a Lennard-Jones form. The results successfully mimicked the terrace-shaped precursor film, but the radius of the film was proportional to $\sqrt{\ln(t)}$ instead of $\sqrt{t}$.[31] Further investigation by De Coninck[32, 33] pointed out if the size of the fluid molecule was too small, the molecules would be trapped for long time in the local minima of the corrugated substrate potential. He simulated two chain-like molecules consisting of 8 atoms and 16 atoms. Both results followed the $\sqrt{t}$ behavior. Other MD simulations done by Haataja focused on long chain molecules, such as polydimethylsiloxane. He found in the precursor films, polydimethylsiloxane molecules preferred orienting themselves perpendicularly to the solid substrate.[34]

2.3 Experimental methods

Experimental observation of nanometer thick films were not possible until the advent of advanced optical technologies and microscopic technologies. Ellipsometry and atomic force microscopy are two of the most common methods for the investigation of the precursor films. In this section, these two technologies will be discussed and the experimental results will be reviewed on the basis of materials.

2.3.1 Instruments

2.3.1.1 Ellipsometry

Ellipsometry is the technique that determines the dielectric properties of thin films. It measures the change in polarization, as light transmits through a thin film and bounces back. A typical elliptical polarized light is composed with a p polarized wave and an s polarized wave. The p polarized wave is parallel to the plane of incident light, while the s polarized wave is perpendicular to the plane. Once the electromagnetic wave is reflected from an interface, both its amplitude and phase change. As a result, the amplitude and phase of both p polarized wave and s polarized wave also change. An ellipsometer measures the complex reflectance ratio, ρ, which may break into two parameters, the amplitude component Ψ and the phase component Δ, shown in equation 2.13.

$$\rho = \frac{R_p}{R_s} = \tan(\Psi)\, e^{i\Delta} \tag{2.13}$$

where $\tan(\Psi)$ is the ratio of the amplitudes of the polarized lights and Δ is the difference of the phases. The reflection coefficients R_p and R_s follow Fresnel equations and are given in equation 2.14 and 2.15

$$R_s = \frac{n_1 \cos\theta_i - n_2 \cos\theta_t}{n_1 \cos\theta_i + n_2 \cos\theta_t} \tag{2.14}$$

$$R_p = \frac{n_1 \cos\theta_t - n_2 \cos\theta_i}{n_1 \cos\theta_t + n_2 \cos\theta_i} \tag{2.15}$$

where n_i is the refractive index, θ_i is the incident angle and θ_t is the transmitted angle.

For a thin film model, light reflects from both air-film interface and film-substrate interface as illustrated in Figure 2.1. Normally, the change of the amplitudes of the waves travelling through a thin film is negligible, while the change of phase is proportional to the thickness of the film. Therefore, by measuring the reflectance ratio, ρ, the change of phase, β, from the top of the film to the bottom of the film will be obtained according to equation 2.16 and 2.17.

$$R_s = \frac{r_{12}^s + r_{23}^s exp(-i2\beta)}{1 + r_{12}^s r_{23}^s exp(-i2\beta)} \tag{2.16}$$

$$R_p = \frac{r_{12}^p + r_{23}^p exp(-i2\beta)}{1 + r_{12}^p r_{23}^p exp(-i2\beta)} \tag{2.17}$$

$$\beta = 2\pi \left(\frac{d}{\lambda}\right) n_2 \cos(\phi_2) \tag{2.18}$$

By applying equation 2.18, the thickness of the film, d, in nanometer scale can be resolved.

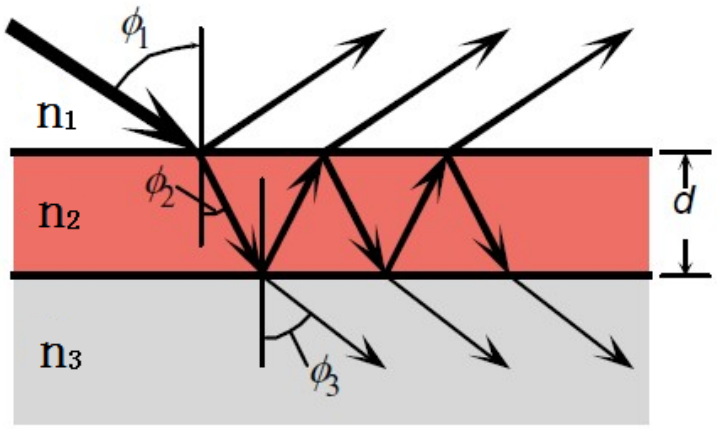

Figure 2.1. Illustration of light reflecting from the top interface and bottom interface of a film. Generally, n_1 represent the refractive index of air; n_2 is the refractive index of the thin film and n_3 is the refractive index of the solid substrate. ϕ_1 is the incident angle; ϕ_2 and ϕ_3 are the transmitted angle in the film and substrate, respectively.

Although the thickness measured by ellipsometry technique could be as accurate as 0.1Å,[35] the lateral resolution remains in the scale of micrometers. It is important to emphasize that the thickness given by ellipsometric measurement is the average thickness over the area of laser spot. In other words, it is hard to distinguish a loosely packed film from the film which is made up of several densely packed patches.

2.3.1.2 Atomic force microscopy

Atomic force microscopy (AFM) was invented in 1986.[36] It detects the surface properties by sensing the surface with a sharp tip. According to Lennard-Jones potential equation, when two neutral particles approach to each other under the distance of potential minimum, the potential grows at a rate of 10^{12}. In other words, AFM is sensitive to the local surface features.

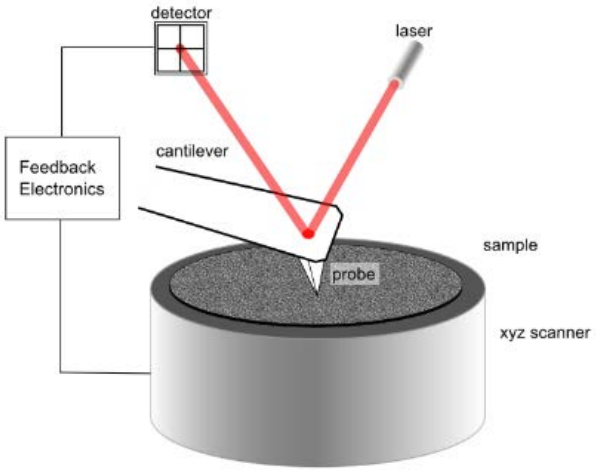

Figure 2.2. Illustration of the basic components of an AFM instrument.

Figure 2.2 illustrates the fundamental components of an AFM which consists of a four-segment photodiode, a three-dimensional scanner, a 632nm laser source, a cantilever forged with an atomic level sharp tip and the feedback electronics. During the scanning, the tip scans over the sample surface and the cantilever bends or distorts according to the change of the surface features. Consequently, the position of the laser spot reflected from the back the cantilever onto the photodiodes changes. A computer generates the resulting images by recording the signals collected from the photodiodes and the feedback electronics.

There are two scanning modes in AFM: contact mode and tapping mode. During the contact mode scanning, a tip wipes over the sample surface. The bend of the cantilever in vertical direction generates the height profile of the surface, while the distortion of the cantilever provides the frictional information. However, the motion of wiping may destroy the sample surface, especially for organic SAMs. Tapping mode, on the other hand, avoids the dragging of the tip over the surface. It makes the tip tap lightly

on the surface so that the soft surface materials are protected. Meanwhile, the interaction between the tip and the surface may result in a phase shift of the cyclical vibration of the tip so that the change of the phase is used to distinguish the chemical identities of the surface.

2.3.1.2.1 Contact mode imaging

As previously mentioned, when two neutral particles approach to each other, the potential increases rapidly below the minimal energy distance. During an AFM contact mode scanning, such repulsive force is constantly balanced by the bend of the cantilever. Therefore, the tilting angle of the back of the cantilever changes and the incident angle of the laser beam changes accordingly. Figure 2.4 illustrates the scheme of an AFM tip coming across the increase of height.

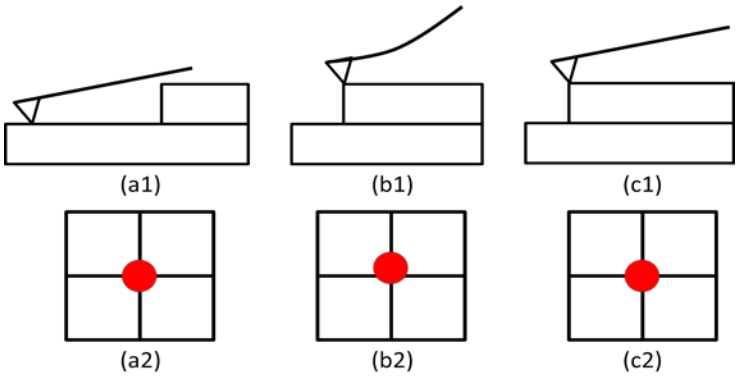

Figure 2.3. Scheme of detecting a height change by AFM (a1) the initial status of a cantilever before coming across the surface feature of a higher step; (a2) the bend of the cantilever due to a higher surface step; (a3) the cantilever restores its original status after z-direction piezo scanner adjusting the height of sample; (b1)-(b3) are the accordingly laser spots projected on photodiodes

Figure 2.3(a1) mimics a tip scanning over a flat surface. The corresponding laser spot reflected from the back of the cantilever projects onto the center of the 4-segment photodiode, Figure 2.3(b1). Here, the central position of the laser spot is set arbitrarily as the initial state. When the laser beam shines on the photodiodes, each segment generates a photocurrent that corresponds to the area of the projected laser spot. The electric circuits transfer the current signals to potential signals for computer processing. By subtracting the potentials generated by the bottom photodiodes from the potentials generated by the top photodiodes (equation 2.19), the electronics uses the difference of the potential to monitor the position of the laser spot.

$$V_{topo} = (V_{tl} + I_{tr}) - (V_{bl} + V_{br}) \tag{2.19}$$

where V_{topo} is the difference of the potential generated by the top photodiodes and the bottom photodiodes, V_{tl}, V_{tr}, V_{bl} and V_{br} are the potentials generated by top-left, top-right, bottom-left and bottom-right photodiodes, respectively. In the illustrated situation, Figure 2.3(b1), V_{topo} equals 0.

Once the tip moves right and bumps into a higher surface feature, the tip-surface distance decreases, and a repulsive force kicks in. In order to neutralize this repulsive force, the cantilever has to bend, according to Hooke's law (Figure 2.3(b1)). Consequently, the tilting angle of the cantilever decreases, which simultaneously increases the incident angle of the laser beam. With a bigger incident angle, the laser spot projected on the photodiodes moves up. Such movement increases the area of the laser spot on the top photodiodes, while decreasing the area of the spot on the bottom photodiodes, as shown in Figure 2.3(b2). As a result, the difference of the potential, V_{topo}, increases. At this stage, feedback electronics detect the change of V_{topo} and apply a direct

current to the z-direction piezo scanner. The z-direction piezo scanner shrinks and moves the sample plate down. Finally the bended cantilever recovers and the laser spot is restored to its original set point. The voltage of the direct current applied on z-direction piezo is recorded and converted to the height of the specific surface point, according to the calibration parameters. By manifesting all x,y,z direction information, a topography image is, therefore, obtained.

Besides the vertical signals correlating the height profile of the surfaces, the horizontal photocurrent changes are used to indicate the lateral interaction between the tips and the surfaces characters. As shown in Figure 2.4(a), when an AFM tip moves from left to right, the lateral interaction resists such motion and causes the distortion of the cantilever. Consequently, the shift of the laser spot projected on the photodiodes causes the difference of the potentials between the left segments and the right segments as described in equation 2.20:

$$V_{fric} = (V_{tl} + V_{bl}) - (V_{tr} + V_{br}) \tag{2.20}$$

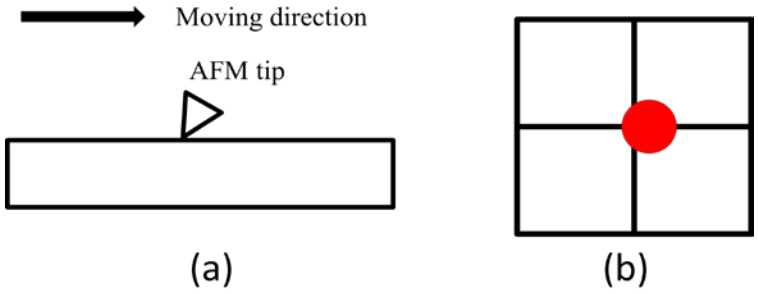

Figure 2.4. Scheme of detecting the frictional signals. (a) An AFM tip resists the movement due to friction. (b) The laser spot reflected from the back of the cantilever shifts right due to the distortion of the cantilever.

The V_{fric} values are, therefore, processed and assembled to be the friction images. Furthermore, the absolute friction values could be obtained through the intrinsic properties of the cantilever, as shown in equation 2.21:

$$F = Ak_{\varphi}\frac{V_{fric}}{L} \tag{2.21}$$

where A is the displacement coefficient that converts the friction signal value V_{fric} to the displacement of the laser spot on the photodiode, k_{φ} is the torsional spring constant, and L is the length of the cantilever.

2.3.1.2.2 Tapping mode imaging

Tapping mode imaging is achieved by applying an alternating force on the end of the cantilever. Instead of keeping the AFM tip in constant contact with the surface, tapping mode makes the tip contact the surface and bounce back to the air alternately, so that it effectively prevents the scratches during the scan and protects the interfacial materials.

Figure 2.5 illustrates the scheme of how the tapping mode detects the increase of heights. Unlike the contact mode, tapping mode monitors the change of the amplitude of a vibrating cantilever. The engaged amplitude is pre-set and kept during the scan. Once the tip comes across an increase of surface height, the amplitude decreases due to the repulsive force between the surface substance and the tip. In order to restore the amplitude back to its set point, a complementary voltage is given to the z-direction scanner to lower the sample surface. This given voltage is, therefore, recorded and converted to the height information. Along with the lateral positioning information, the heights of each scanned point are assembled to be topography images.

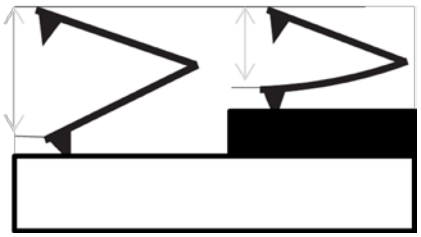

Figure 2.5. Scheme of detecting the height change by tapping mode. The amplitude of the vibrating cantilever decreases once the tip comes across the height increase.

The other information gathered in tapping mode is the phase contrast. A phase contrast is the latency of the cantilever's response to its driving force. If the AFM cantilever is vibrating under a vacuum environment, the harmonic oscillation keeps the cantilever vibrating at its resonance frequency. However, in the air, the hydrodynamics, the acoustic noise and the interfacial interaction keep the cantilever from vibrating, which is called damping force γ. Therefore, an alternating driving force is applied at one end of the cantilever to complement the energy loss. For the same reason, the tip end of the cantilever is unable to respond to such driving force instantly. Based on the difference of the energy loss, the latency varies. As shown in the blue and the green sinusoidal lines in Figure 2.6, different interfacial materials cause different energy loss, which consequently results in different latency from the tip end. By applying equation 2.22, the phase shifts of the driving force and its response are obtained:

$$\alpha = \tan^{-1}\frac{2\gamma\omega}{\omega^2 - \omega_0^2} \tag{2.22}$$

where α is the phase shift, ω is the angular frequency at the tip end, and ω_0 is the angular frequency at the cantilever end. Since the phase shifts within a phase image are collected

at the same environmental conditions, these values reflect the material characters over the surfaces.

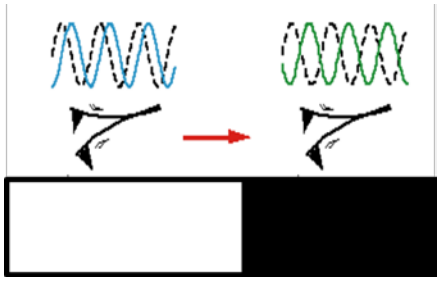

Figure 2.6. Scheme of phase change. The tip scans from the write substrate to black substrate resulting in different phase shifts.

2.3.2 Materials

2.3.2.1 Polydimethylsiloxane

Polydimethylsiloxane (PDMS) is one of the most intensively studied substances due to its inertness and high viscosity. Drevillon[37], Beaglehole[35] and Heslot[38] employed spatially resolved ellipsometry to study the spreading of PDMS over silicon wafers. Instead of observing the pancake-shaped precursor films, they detected a transition of the film into a surface gas state at which molecules moved freely over the surface. Meanwhile, the radius of such a film near molecular thickness was also detected to be around $\sqrt{D_1 t}$, where, D_1 is the diffusion coefficient.

Heslot made an effort on exploring the expansion of the films driven by the capillary force.[39] He immersed a silicon wafer vertically into the light silicon oil (PDMS). The molecules slowly "climbed up" (Figure 2.7). After 56 hours, the length of the film reached 10 mm, while the thickness of the major part of the film was about 6 Å. Since the width of a PDMS monomer was of the order of 6 Å, this result suggested the major part

of the film was composed of a monolayer of PDMS molecules laying parallel to the silicon wafer surface. In addition, the inset of Figure 2.7 showed the length of the precursor film also followed the law of the square root of time.

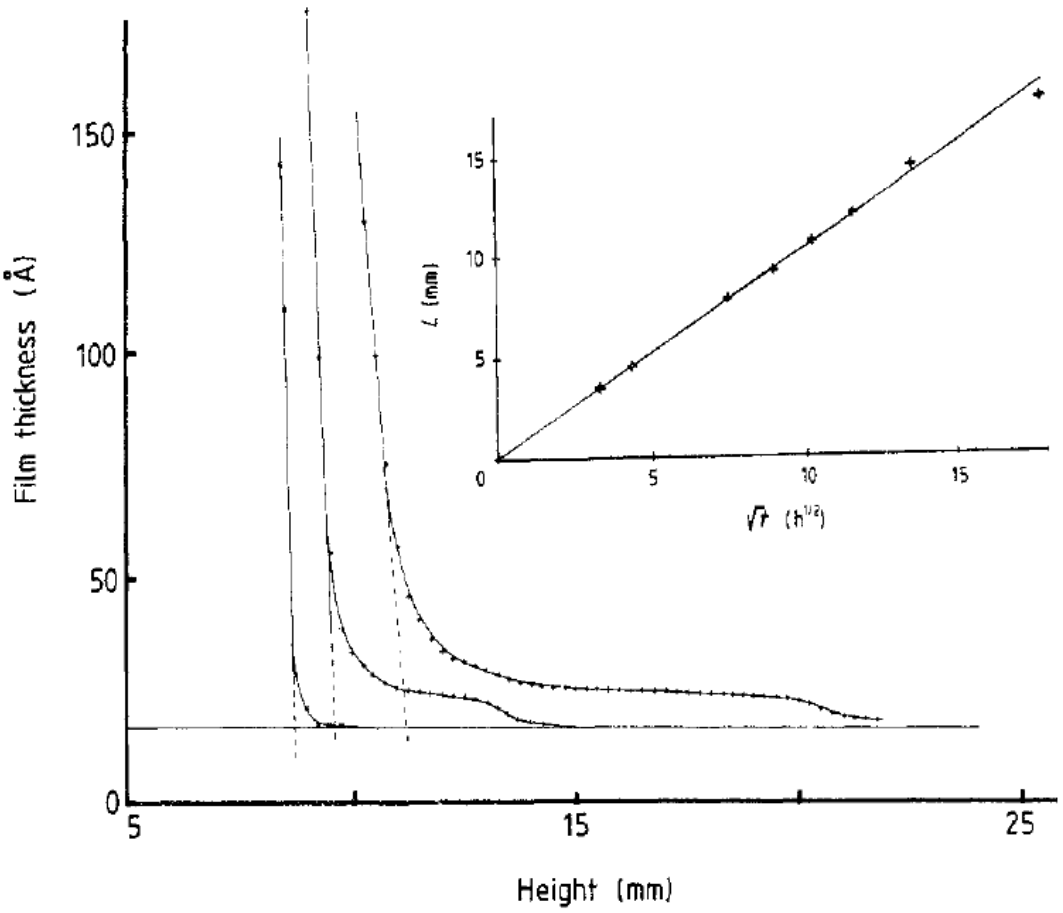

Figure 2.7. Ellipsometric results of the films rising on a vertical silicon wafer.[39] The curves from left to right represented the film developed for 10m, 10h and 56h. The inset shows the length of the films grew as a function of the square root of time.

Significant progress was made by Cazabat[12] soon after Heslot reported his results. By employing both time-resolved and spatial-resolved ellipsometry, Cazabat discovered

the "terraced wetting" phenomenon that liquid drops (PDMS) spread on a UV-ozone cleaned silicon wafer formed a series of distinct layers, as shown in Figure 2.8. As the spreading proceeded, the top layers emptied themselves into the lower ones. Each layer expanded with its own diffusion coefficient. Similar phenomena were also observed for spreading tetrakis(2-ethylhexoxy)-silane on a vertical wall.[14]

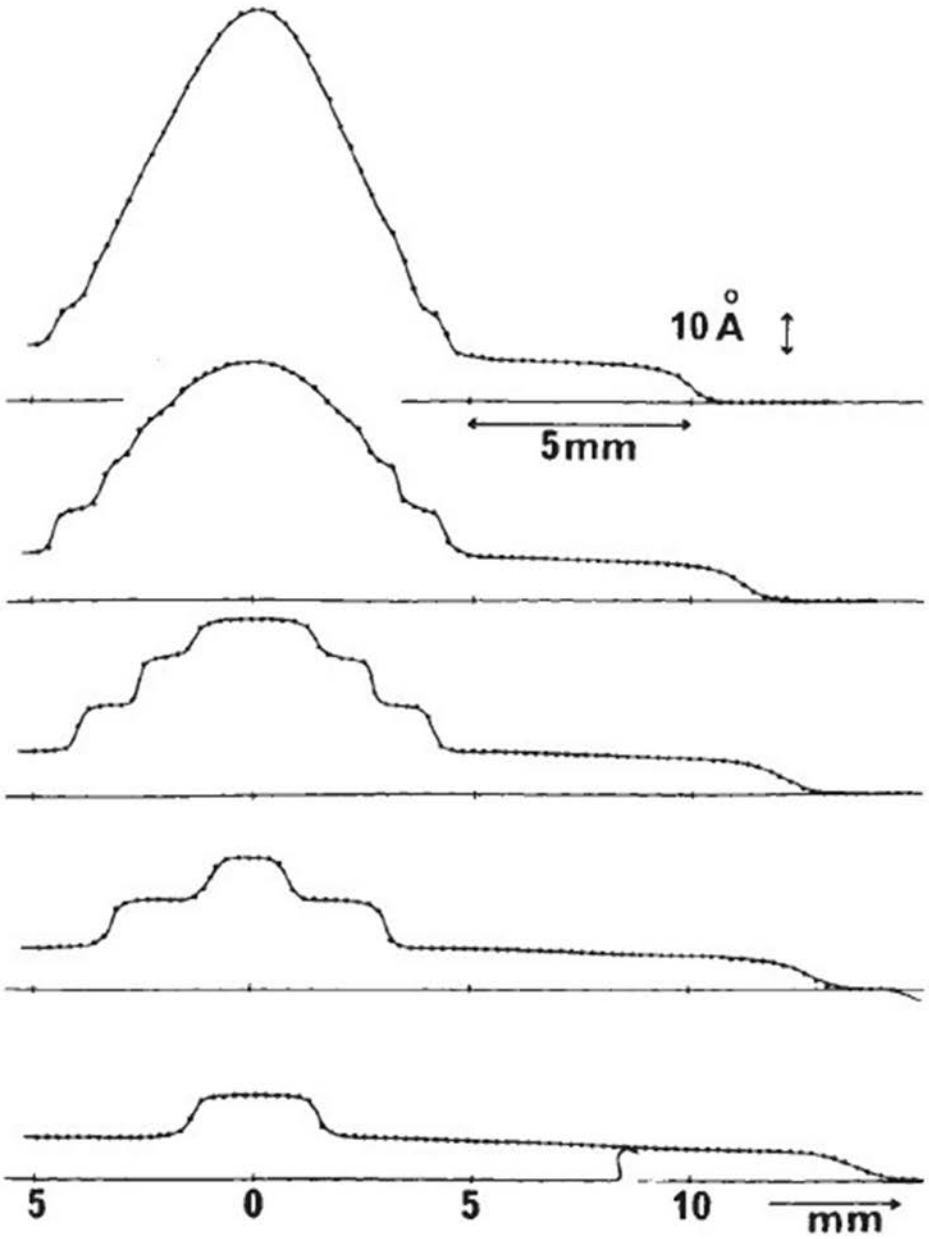

Figure 2.8. The ellipsometric thickness profile of silicon oil spreading over a silicon wafer for 71h, 83h, 118h, 144h and 168h respectively.[12]

Cazabat also explored the effects of solid substrates on precursor films.[40] He employed two kinds of surfaces: a high energy surface and a low energy surface. The high energy surface was the fresh UV-ozone cleaned silicon wafer, while the low energy

surface was coated by a monolayer of fatty acids that were terminated with double bonds. As long as the liquid drop acted as reservoir, up to 5 terraced layers were observed. As described before, when the drop started to run out of the materials, the top layer drained itself into the layer beneath itself, and all the expansion of the layers followed the $\sqrt{t}$ law. Contrary to the high energy surface, molecules spreading over the low energy surface only formed a uniform film, known as the pancake structure.

The thickness of the precursor films was not only affected by the solid substrates but also influenced by other factors. By intentionally coating trimethylsilane loosely on the wafer, Cazabat observed the noise of the height profiles of the precursor films increased.[41] Furthermore, by increasing the surface energy of solid substrates and increasing the viscosities of PDMS, the thickness of the precursor films was also increased.[41] Temperature, as an environmental factor, also directly impacted the sharpness of the edge of the precursor films, that the higher the temperature, the smoother the edge.[42]

2.3.2.2 Long-chain n-alkane

Compared to PDMS, long chain alkane, $C_{2n}H_{2n+2}$ (n>15), is simpler in structure and smaller in size. Due to the interaction of methylene group (-CH_2-), alkanes often align their carbon backbones with each other in their solid states.[43] The alignment of the molecules at the alkane/SiO_2 interface was not systematically studied until 1993. Wu proposed a phase transition of alkane from an isotropic liquid to a smectic-like ordered surface monolayer at the alkane/air interface and alkane/SiO_2 interface.[44, 45] Riegler soon confirmed such transition by ellipsometric study during the freezing process.[46] However,

by carefully comparing the melting points (T_b) of alkanes in bulk and the melting points (T_s) of alkanes at the interfaces, Riegler found that the phase transition occurred within this temperature region.[47] During the process of heating, the hemispherical drop of alkane would melt first, leaving a layer of ordered alkane monolayer on the surface at the temperatures between T_b and T_s. This layer of ordered molecules turned into liquid phase after the temperature rose above surface freezing point, T_s. The hemispherical drop, therefore, merged into the surface monolayer and formed a thicker film, as shown in Figure 2.9. Such process suggested that a monolayer of alkane molecules nearest the substrate's surface formed prior to the spreading of the alkane drop, changed the surface tension of solid/vapor interface, and eventually changed the contact angles.

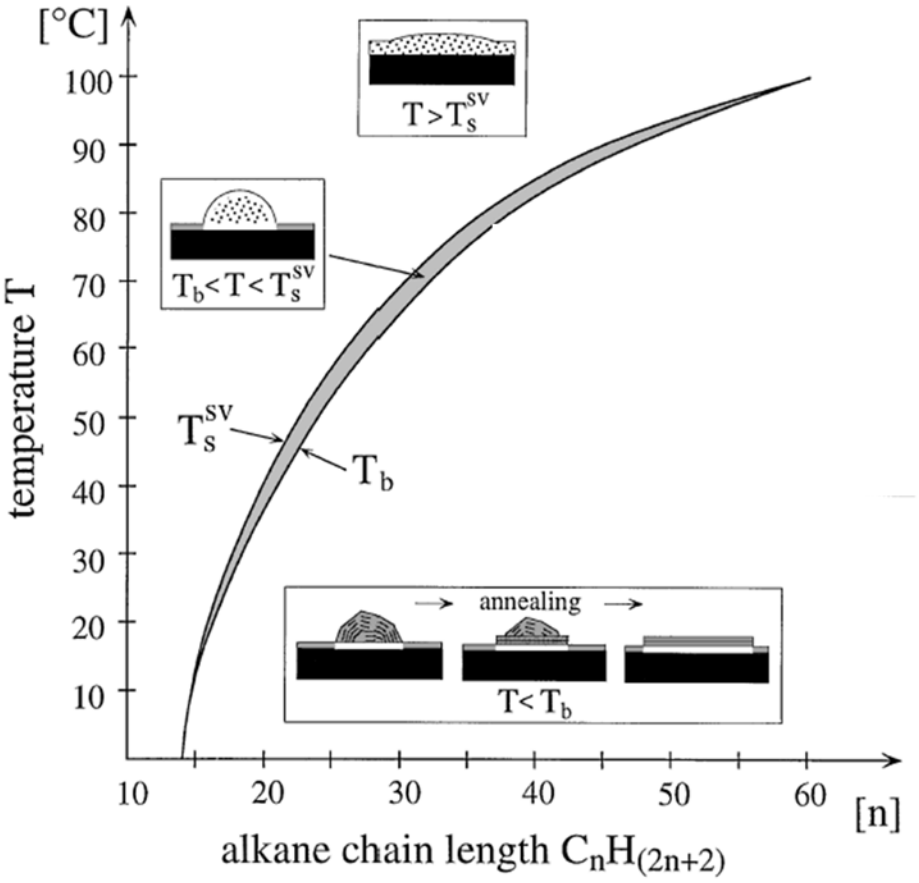

Figure 2.9. Illustration of phase transition around the bulk melting point and surface freezing point for a series of long-chain alkanes.[47] T_b is the melting point of alkane in bulk and T_s is the melting point of an alkane on surfaces, known as the surface freezing point. Above T_s, alkane on surfaces completely melts and forms a thick film. At the temperature between T_b and T_s, the hemispherical drop keeps in liquid phase, while some alkane molecules pack densely and form a thin film over the solid substrate. When the temperature is further cooled down below the T_b, all the molecules are frozen. Some of the molecules will align themselves in layers and stack themselves.

Along with the ellipsometry results and X-ray reflectivity data, Riegler proposed a monolayer model that the precursor films of long chain alkanes were formed by a monolayer of molecules. Those molecules in the precursor films stood perpendicularly to the SiO_2 surface, as shown in Figure 2.10.[48] The study of the monolayer with respect of different amount of molecules was reported in 2000.[49] In the experiments, different amounts of the triacontane (C30) molecules were placed on the silicon wafers to distinct two scenarios: excess coverage (Figure 2.11(a)) and submonolayer coverage (Figure 2.11(b)). For the excess coverage scenario, the number of C30 molecules was more than enough to cover the silicon wafer surface. Once the wafer was cooled below the surface freezing point T_s of C30, C30 molecules were aligned perpendicularly to the wafer surface, and a monolayer of the C30 molecules formed a precursor film over the substrate. At the same time, the excess molecules stacked on top of the precursor film and also formed ordered layers. On the other scenario, C30 molecules were inadequate to cover the wafer with their backbones perpendicularly to the surface. Based on the reflectivity results, Riegler believed that molecules were oriented in two directions, either perpendicular or parallel to the surface. The patches of the perpendicular molecules had lower surface energy and the patches of the parallel molecules had higher surface coverage. The precursor film made up of a mosaic of these patches covered the solid surface and have the minimal surface tension. Such mosaic structures of precursor films were also observed by Yamamoto.[50]

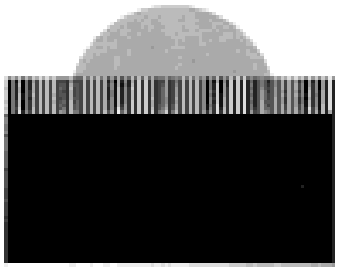

Figure 2.10. Illustration of monolayer model.[48] At the temperature around the surface freezing point, alkane molecules stand perpendicularly to the surface and form a monolayer. The molecules in hemispherical drop stay in liquid phase and sit on the top of the monolayer.

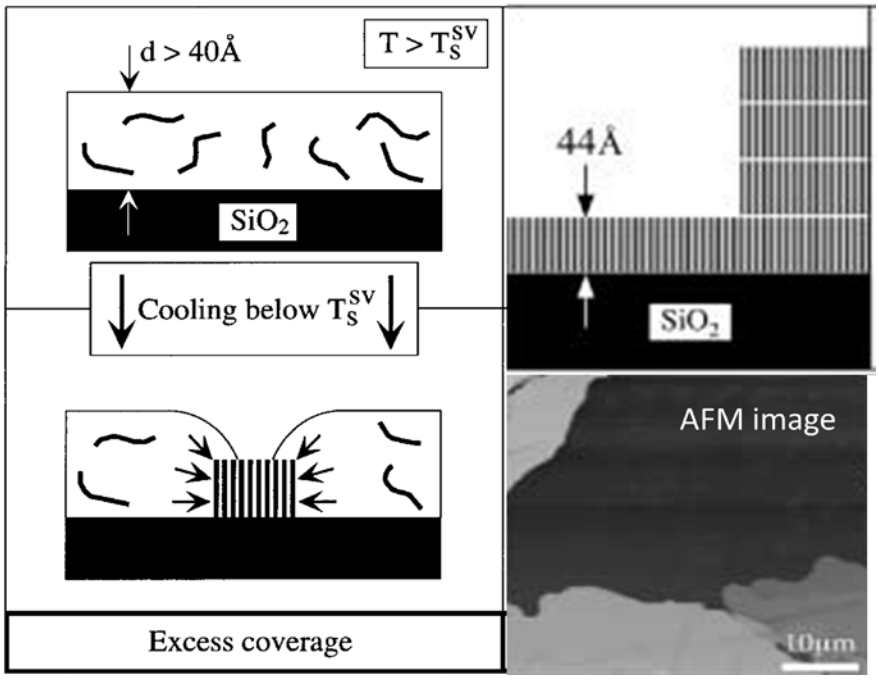

(a)

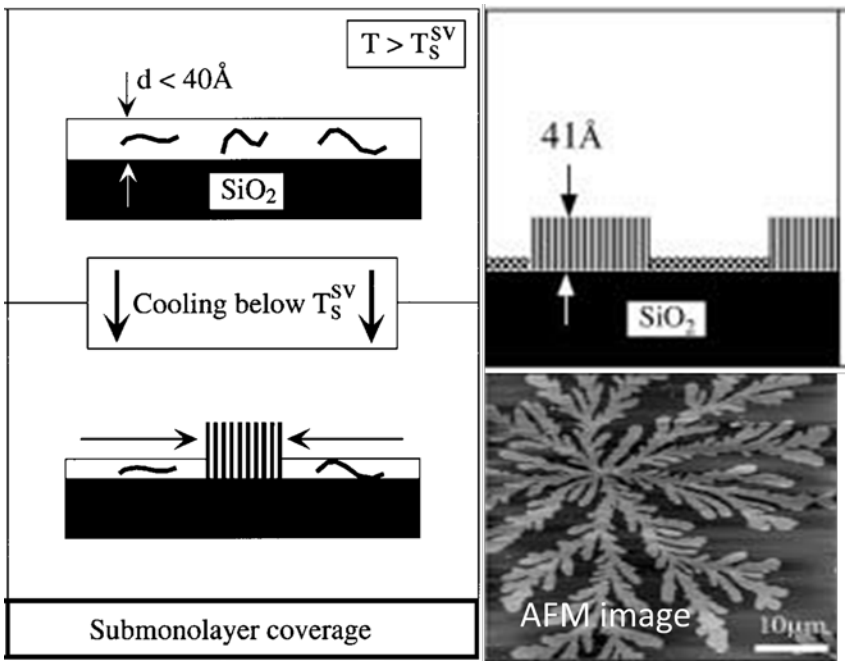

(b)

Figure 2.11. Scheme of triacontane spreading over SiO_2 with excess coverage and submonolayer coverage.[49] (a) Excess coverage: The precursor film consists of several layers of C30 molecules that are densely packed with all their carbon backbones perpendicular to the surface. The topography image shows the continuity and the terraced structure of the film. (b) Submonolayer coverage: The layer of the perpendicular molecules could not cover the surface and left the vacancy covered by the molecules laying parallel to the surface. The dentritic fractal detected by AFM indicates the inefficient number of the molecules to cover the whole area.

The structures of the precursor films of long-chain alkanes were also investigated by Taub. However, he did not agree with the monolayer model. He implemented very high resolution ellipsometry (VHRE) and found that in addition to the layers to which molecules stood perpendicularly, a thin film of alkane molecules laying parallel to the

surface existed between the SiO_2 substrate and perpendicular film (Figure 2.12).[51] Such structure was called bilayer model. Furthermore, in the so-called "perpendicular" film, dotriacontane (C32) molecules were found tilting 26.5° to the surface norm.[52] This bi-layer structured precursor film and the tilting angles were also observed by Cai, when hexatriacontane (C36) was spread over a carboxylic acid terminated surface.[53] Four tilting angles, 0°, 29.25°, 40.02° and 48.24°, were found with AFM measurements. These values matched the calculation results where C36 molecules aligned their neighboring molecules with 0, 2, 3 and 4 methylene groups shifts, as listed in table 2.1.

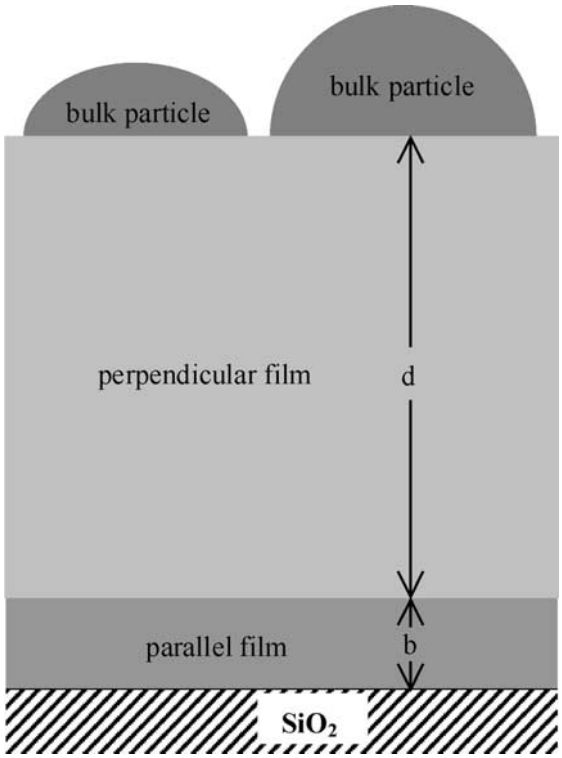

Figure 2.12. Illustration of "bilayer" model.[51] The precursor film of C36 is composed of two kinds of layers: the perpendicular layer sitting on top of the parallel layers. The molecules in the parallel layers lay their carbon backbones parallel to the SiO_2 surface, and the molecules in the perpendicular film stand perpendicularly to the surface.

Table 2.1. The tilting angles and the corresponding heights of n-hexatriacontane molecules in the precursor films

C36 molecules shifting distance (1 Unit=1.26Å)	**Calculated C36 tilting angle off the surface norm (°)**	**Calculated C36 layer thickness (Å)**	**Measured C36 layer thickness (Å)**
0	0	50.6	50.6±0.3
2	29.25	44.1	44.3±0.3
3	40.02	38.7	38.8±0.4
4	48.24	33.7	34.1±0.6

The spreading kinetic study of the precursor films formed by long-chain alkanes did not show any exceptions. By taking a series of optical microscopic images during the expansion of a precursor film, the precursor film was observed having two layers (Figure 2.13).[13] Each layer of the film expanded with its own diffusion coefficient.

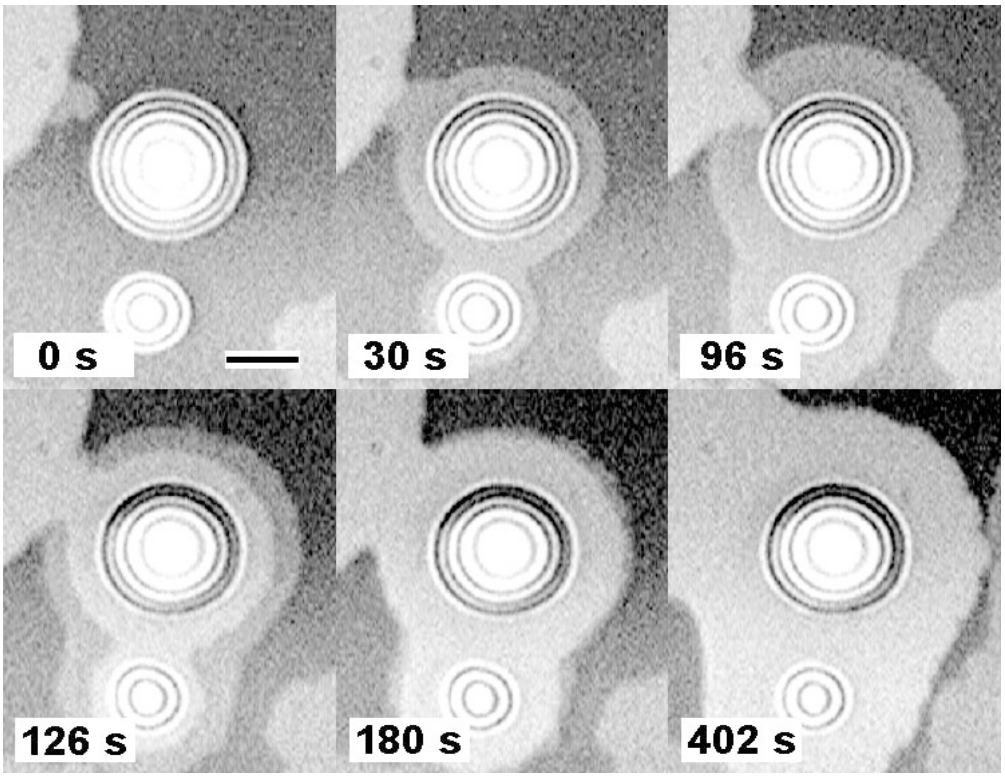

Figure 2.13. Growth of hexatriacontane monolayer and bilayer terraces (optical reflection microscopy, 1.5°C below its melting point).[13]

2.3.2.3 Ionic liquids and other materials

PDMS and long-chain alkanes are worm-like molecules. Both of them have the energy preferences to form terrace-structured precursor films over solid substrates. Organic molecules that have the similar shape, such as 4-octyl-4'-cyanobiphenyl (8CB) liquid crystals,[54] perfluoropolyalkylether,[55] polymers with poly(n-butyl acrylate) side chains[56] etc., were also found forming terrace-structured precursor films. Naturally, all of their spreading dynamics follow the $\sqrt{t}$ law.

Ionic liquids (ILs), unlike other nonpolar organic compounds, are influenced by electronic interactions and have negligible vapor pressures. Although Endres,[57]

Casparotto,[58] and Gnahm[59] took efforts to explore the structures of the IL films at IL/solid interfaces, the layering structures of the IL films were not confirmed until Mezger reported the X-ray reflectivity measurements of the IL films over a sapphire substrate.[60] Other studies of the IL spreading, such as 1-butyl-3-methylimidazolium bis-(trifluoromethanesulfonyl)imide (BMIM-TFSI) and 1-butyl-3-methylimidazolium tetrafluoroborate (BMIM-BF_4), were conducted over Highly Ordered Pyrolytic Graphite (HOPG) surface.[61] The results showed the precursor films also had a terraced structure as shown in Figure 2.14. Each layer of the BMIM-TFSI film was found to be 2.2 nm thick, and the thickness of a BMIM-BF_4 layer was 0.79 nm.

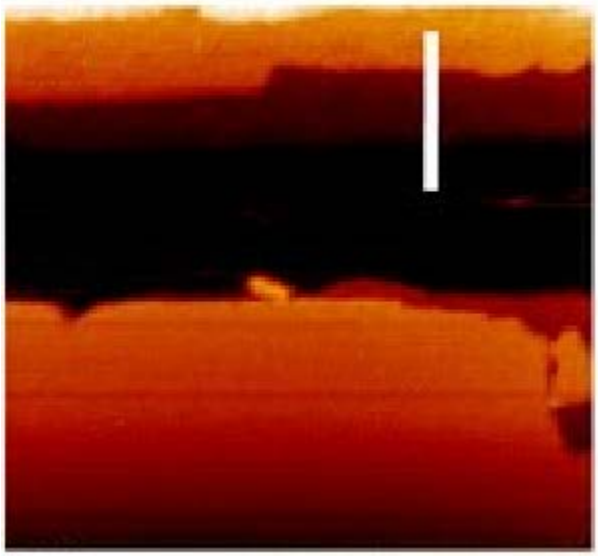

Figure 2.14. AFM topography image of a BMIM-BF_4 film over HOPG surface.[61] Two layers of IL molecules were observed along the white line. The average thickness of the layers was 0.79 nm.

Another approach for observing the terraced structure of the IL films was to measure the penetration force.[15] By immersing the solid substrates, such as gold, mica, and HOPG, into the pure IL liquids, layers formed near the solid surfaces. A typical processed indenting force and distance curve is presented in Figure 2.15. The periodic change of the forces suggested a layered structure of the film, while the distance between each peak implied the thickness of each layer was 0.8 nm. The number of the layers depends on both the solid substrates and the anions of the imidazolium ILs.[15, 62]

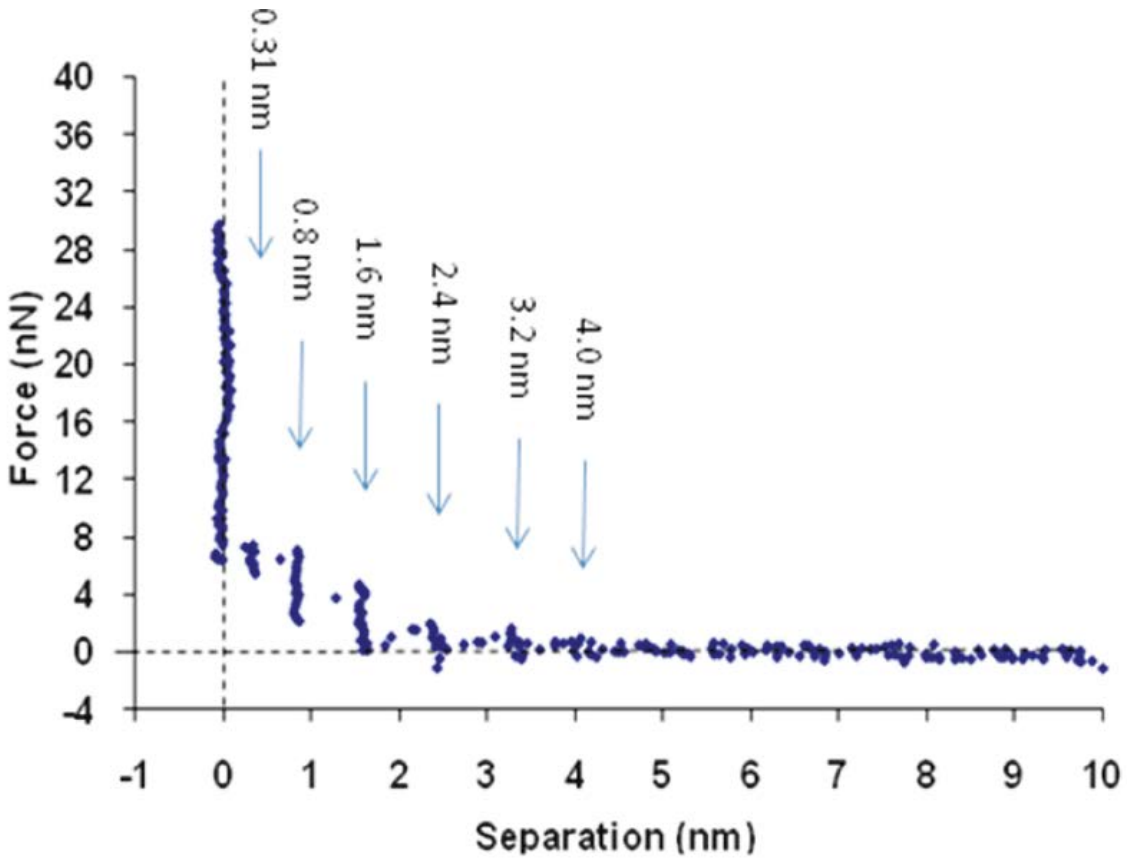

Figure 2.15. Typical force versus distance profile for an AFM tip approaching from a Au(111) surface in 1-ethyl-3-methylimidazolium fluoroalkylphosphate.[15]

Further study on the cation orientation of the 1-alkyl-3-methylimidazolium ILs at the interfaces showed dependence on the distance between the IL molecules and the surface substrates. Dou reported that when the number of the carbon of the alkyl side chain was between one to four, the imidazolium ring and the alkyl group in the first two layers of the precursor films nearest the graphene surface laid parallel to the surface plane.[63] This result was also agreed with the results of molecular dynamics simulations.[64] With the increase of the distance between the IL molecules and the surface, the alkyl groups started to tilt.[63]

Upon the IL/vapor interface, there are two main arrangements of the orientation of the imidazolium ring. By using surface-sensitive vibrational spectroscopy sum frequency generation (SFG), Rivera-Rubero found that at the IL/vapor interface, the imidazolium ring was parallel to the solid substrate, while the alkyl group tilted 20-54° to the surface norm, as illustrated in Figure 2.16(a).[65-67] The orientation of the alkyl group was also confirmed by the results of X-ray reflectivity and direct recoil spectroscopy.[68-71] However, Law et al. pointed that the imidazolium ring at the IL/vapor interface was rotated vertically to the surface plane. Particularly, for 1-butyl-3-methylimidazolium cation, the surface norm passed through two N atoms with an error of ±30°.[69] Furthermore, Seddon[72] and Deutsch[71] observed the alternating alignment of the 1-alkyl-3-methylimidazolium cations at the IL/vapor interface that the neighboring methyl groups pointed in opposite directions as illustrated in Figure 2.16(b). For the long-chain alkyl group substitutes, C_{12}-C_{18}, the van der Waals interaction between the alkyl group dominated the alignment of the IL molecules and leaded to a charged-alkyl-charged tri-layer structure.[72, 73] For short-chain alkyl group substituted IL, although Deutsch had confirmed the alternating

orientation of the molecules, no evidence showed the 1-butyl-3-methylimidazoloum cations were also coupled with their butyl groups.

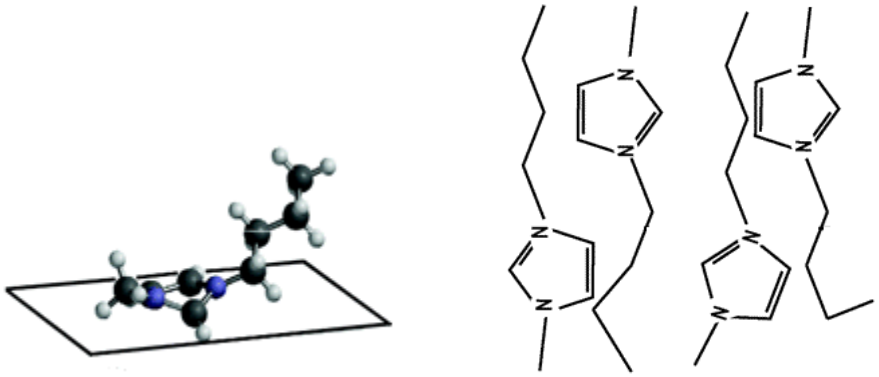

(a) (b)

Figure 2.16. Orientation of 1-butyl-3-methylimidazolium cation at IL/vapor interface. (a) SFG results showed the imidazolium ring was parallel to the surface, while the butyl group tilted 20-54° to the surface norm.[65] (b) Deutsch proposed the alternating alignment of the 1-butyl-3-methylimidazolium cation, according to X-ray reflectivity results.[72]

2.4 Summary

A precursor film is composed of thin layers of liquid molecules that are packed orderly over a solid substrate during the spreading. In this chapter, the studies of the precursor films are reviewed from the aspects of experimental methods and liquid compounds. The growth of a precursor film is mainly due to the flow of the liquid molecules and is also affected by the condensation of the vapor. Dynamically, the radius of a precursor film is proportional to the square root of time.

The structures of the precursor films were investigated with ellipsometry, optical microscopy, atomic force microscopy etc. In micro-scale, the precursor film was found in a terraced layering structure. Molecules in each layers were packed orderly. Particularly

for long-chain n-alkane, the molecules may lay the parallel to the surface or perpendicularly to the surface. For 1-alkyl-3-methylimidazolium, its imidazolium ring and its alkyl group may both lay parallel to the surface in the first two layers nearest the solid substrate. At the ionic liquid/vapor interface, the 1-alkyl-3-methylimidazolium cations may align alternately with neighboring methyl groups pointing in opposite directions.

Chapter Three

PATTERNING TECHNIQUE: OCTADECYLTRICHLOROSILANE PARTIALLY DEGRADED PATTERNS

3.1 Introduction

Patterning processes play an important role in nanotechnologies, such as integrated circuits, biosensors, tissue engineering, etc.[74] The conventional techniques for fabricating patterns are based on various lithographical methods, such as photolithography,[75] electron beam lithography,[76] and ion beam lithography.[77] However, these techniques are often limited by their high costs and poor accessibilities. Atom force microscopy nanolithography is a newly developed method. It is potentially low-cost and has nanometer precision in patterning and replication.

Since the invention of AFM in 1986, it has been widely used to directly image the surface morphology with atomic and molecular resolutions.[36] As previously mentioned, the principle of AFM is to regulate the force sensed by the tip from the surfaces. Typically, the curvature of an AFM tip is only 20-60 nm. When suitable forces, currents, or other external fields are applied, the tip could induce various physical modifications and chemical reactions to the interested substrate areas. Due to the unique positioning capability, AFM nanolithography is well-suited for creating site-specific and localized functional structures.

After almost two decades of development, most AFM nanolithography techniques can be classified into two categories: force-assisted AFM nanolithography and bias-

assisted AFM nanolithography. In a force-assisted process, a force larger than the force required for imaging is normally applied. The interaction between the tip and the surface is mainly mechanical. By the motion of scratching, pulling or pushing the surface, the patterns are fabricated. Techniques in this category include: mechanical indentation and plowing,[78] thermomechanical writing,[79] and nanomanipulation.[80]

Instead of manipulating the loading force, bias-assisted AFM nanolithography creates a strong electric field at its tip. Under a high localized electric field, 10^8 V/m to 10^{10} V/m, anodic oxidation,[81] electrochemical deposition,[82] and electrostatic attraction[83] were developed. Anodic oxidation, also known as local probe oxidation, in principle, brings the oxidative OH^- and O^- to the surfaces to form localized oxide nanostructures.[74] This technique was first performed on Si(111) surfaces. Day et al. found the growth of the SiO_2 dots is linearly dependent on the electric pulses applied on the Si surface.[84, 85] Further study of the local oxidation involved a large number of other metals, such as titanium,[86] tantalum,[87] niobium,[87] and molybdenum.[88, 89]

Another approach of local oxidation lithography is to create the nanostructures on the self-assembled membranes (SAM). Sugimura pioneered a nano-structured surface with two different SAMs.[90] First, Sugimura prepared an octadecyltrimethoxysilane SAM on a silicon wafer; the electric pulses were then applied on the interested spots to remove the organosilane film. Along with the elimination of the silane molecules, Si was turned into SiO_2. An increase of the height was observed as well. Finally, the other silane, fluoroalkylsilane (FAS), was then grown on the structured SiO_2 dots.

A significant progress for local oxidation of the SAM films was later made by Sagiv.[91, 92] He successfully created a protocol to quantitatively build the nano patterns

from a monolayer of SAM to a multilayer of SAMs, known as "constructive nanolithography".[93] Upon an OTS SAM, the electric pulse applied via the AFM tip only oxidized the top methyl groups to carboxylic acid groups under ambient conditions. The oxidation of Si under the SAM was negligible. In other words, it created zero-contrast topographical patterns. Silane molecules interacting with those carboxylic acid groups may form the second layer of the SAM.[91, 93, 94]

A similar method to partially oxidize the OTS SAM to OTSpd patterns was developed by Cai and Pei in our group.[53, 95, 96] As the fundamental experimental method in this dissertation, the preparation and characterization of the OTSpd patterns are thoroughly discussed in this chapter, even though most of the results have already been described in the literature.[53] In this local probe oxidation lithography technique, the OTS SAM is neither completely decomposed nor remains the same height. By conducting a pulse through the tip, an electrochemical reaction is induced on the OTS SAM surface under 100% relative humidity. OTS molecules are partially degraded, called OTSpd (Figure 3.1). It was confirmed that the OTSpd patterns were terminated with carboxylic acid groups that allow most organic compounds to form thin films. The average depth of the OTSpd patterns was also measured to be 10.2±0.7 Å. By controlling the voltage and the dwelling time, the sizes of the patterns were controlled from 20nm to sub-millimeter, which exceeds the scan range of AFM.

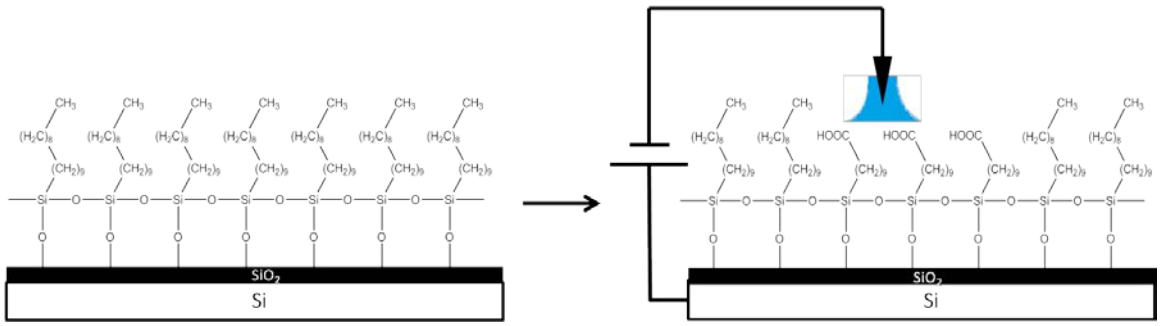

Figure 3.1. Scheme of fabricating OTSpd pattern on OTS SAM. A flat OTS SAM sample was used. Under 100% relative humidity, water meniscus formed between the tip and SAM surface. By anodic oxidation, OTS molecules were partially degraded. The fabricated pattern was 10.2 Å below the OTS surface and was terminated with carboxylic acid groups.

3.2 Octadecyltrichlorosilane partially degraded (OTSpd) patterns

3.2.1 Materials and instruments

Silicon (100) wafers, nitrogen doped with 13 ohm·cm resistivity, were purchased from James River Semiconductors. Octadecyltrichlorosilane (OTS, 97%) was from Gelest. 1-Pyrenylidiazomethan (PDAM, ≥97%) was purchased from Invitrogen. Chloroform (HPLC grade) was from Mallinckrodt Baker. Toluene (HPLC grade) was from EMD. All chemicals were used without further purification.

The OTSpd patterns were fabricated with an Agilent PicoPlus AFM, which was equipped with an environmental chamber. The tips, CSC-17, used to fabricate the patterns were purchased from MikroMasch. These tips were coated with Ti-Pt and generally had a force constant of 0.18±0.10 N/m. The AFM tip positioning was controlled by the software, PicoLith. After the pattern fabrication, the patterns were

characterized in tapping mode with MikroMasch NSC-14 tips. The fluorescence image was captured with Nikon Eclipse N55i Microscope.

3.2.2 Fabrication of the OTSpd patterns

As a fundamental step, the preparation of OTS SAM coated silicon wafer has been reported extensively.[97-99] First, a silicon (100) wafer cleaned by Piranha solution (1:2 volume ratio of conc. H_2SO_4 to 33% H_2O_2) is incubated in 5mM OTS/toluene solution for 10 hours. After thoroughly rinsed with chloroform, the wafer is kept in a 100% relative humidity environment for another 10 hours to stabilize the OTS film. Repeating the incubation-stabilization procedure three times, a pinhole free, fully expanded, and densely packed OTS SAM coated silicon wafer is ready for further use.

The fabrication of OTSpd patterns is conducted with an Agilent PicoPlus AFM in contact mode. A Ti-Pt coated conductive tip is hooked up with the electric circuit and is also kept in contact with OTS SAM coated wafer during the fabrication. As a DC bias, normally 10 V, is applied on the tip at 25 °C and 100% relative humidity conditions, the OTS molecules are partially decomposed, and the terminated functional groups are converted to carboxylic acid groups. The size of the pattern is mainly controlled by the electric dwelling time.

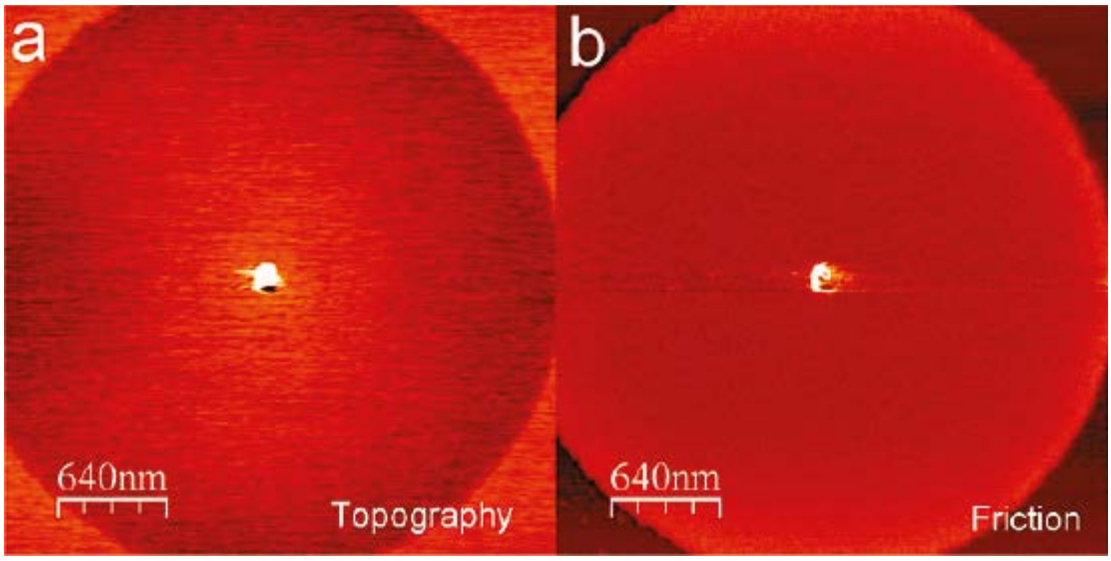

Figure 3.2. OTSpd pattern fabricated by a stationary tip.[53] (a) topography image of a OTSpd pattern fabricated at 100% humidity environment and 25° (b) the corresponding friction image of the OTSpd pattern.

Figure 3.2 shows an OTSpd pattern on the OTS surface. Figure 3.2(a) is the topography image, and Figure 3.2(b) shows the frictional change over the scanned area. In Figure 3.2(a), a round OTSpd pattern in brown is surrounded by dark-yellow OTS films. At the center, the bright dot is the place where the tip applied bias. Generally, in a topography image, the height of the surface is presented in brightness. Particularly in Figure 3.2(a), brighter the color, higher the surface feature. Therefore, the height of the OTSpd pattern in Figure 3.2(a) gradually decreases from the center to the edge. The area surrounding the pattern is higher than the area of the OTSpd pattern. Friction signals are mainly determined by the interaction between the tip and surface hydrophilicity. Since the Ti-Pt coated tip is hydrophilic, the surface area possessing more hydrophilicity will show stronger interaction with the tip. In other words, those areas showing brighter color in friction image are more hydrophilic. In Figure 3.2(b), the OTS surface is the darkest

and the OTSpd pattern is brighter. Those results match the structures of the patterned surfaces that the OTS SAM is terminated with hydrophobic methyl groups while OTSpd patterns are terminated with hydrophilic carboxylic acid groups, which will be proven later in this chapter.

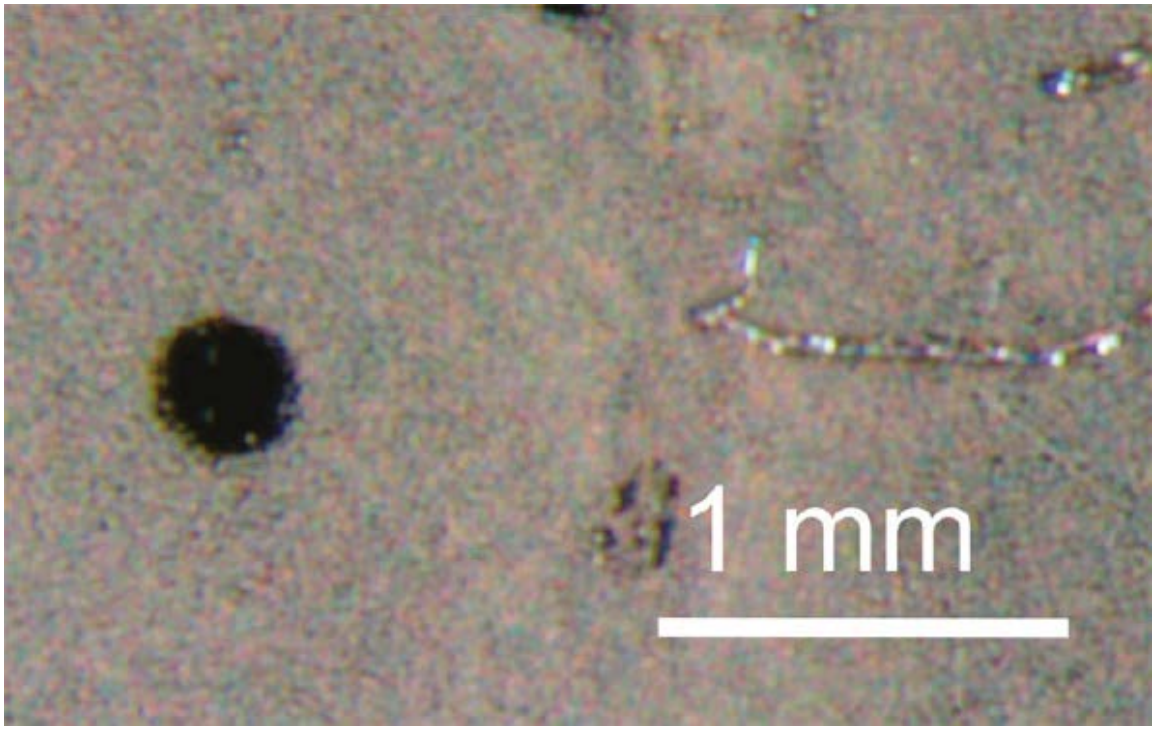

Figure 3.3. Optical microscopy image of an OTSpd pattern fabricated under the conditions of 100% humidity, 25°C, 10V and 60min dwelling time.[53]

The oxidation of an OTS SAM is normally controlled by the environmental humidity, bias applied, and the dwelling time. Low humidity will only allow the top methyl groups of OTS SAM to be oxidized,[94] while the bias and the dwelling time, together, control the sizes of the OTSpd patterns. Here, the bias are kept at 10 V to investigate the sizes of the OTSpd patterns impacted by dwelling time. Figure 3.2 has

already shown an OTSpd with its diameters in micrometers. Figure 3.3 shows an optical microscopy image of an OTSpd pattern in submillimiter scale. This pattern was fabricated at the same conditions, 100% humidity, 25 °C, 10 V, as the pattern shown in Figure 3.2, except for an extremely long dwelling time of 60 minutes. Since the movement of the tip is limited by the range of the piezo scanner that is only 50 μm by 50 μm, this pattern can be only formed through a long lasting electric pulse. During the fabrication of this pattern, water was condensed over its carboxylic acid hydrophilic surface and made this pattern observable under optical microscopy.

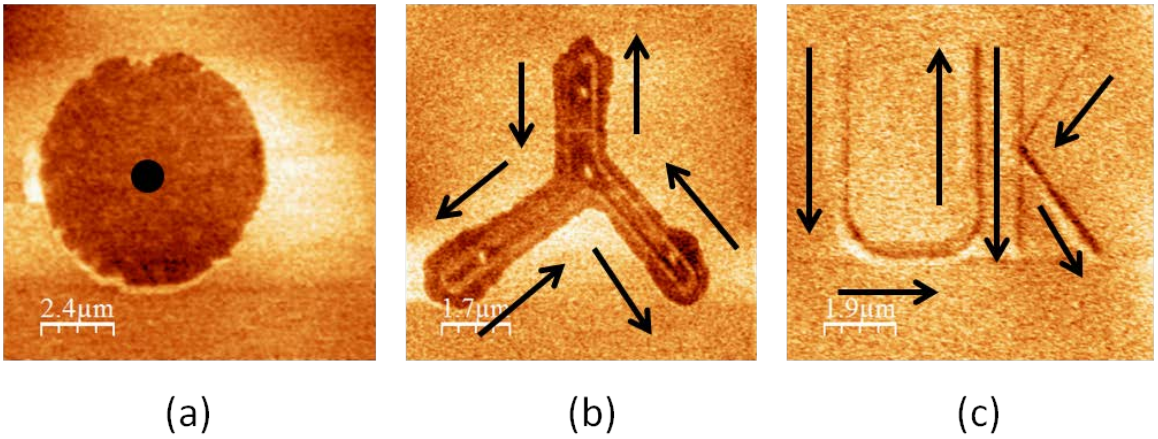

Figure 3.4. Fabrication of OTSpd patterns with different shapes. (a) A stationary tip created a round pattern. (b) Continuous movement of the tip fabricated a three-way mark. (c) OTSpd pattern of "UK". The AFM tip was lifted after fabricating the letter "U", and re-approached to fabricate letter "K".

The shapes of the OTSpd patterns are controlled by the motions of the AFM tip. By implementing the programmable software, PicoLith, one can make the tip stay, move, withdraw, and approach. Figure 3.4 shows a series of topography images of OTSpd

patterns made with PicoLith. The black dot and arrows indicate the motions of the tip along the surface. In Figure 3.4(a), the tip stayed at the black dot while a 10 V DC pulse was applied for 5 seconds. Thus, a disc-shaped pattern was fabricated. Figure 3.4(b) shows a three-way mark fabricated through a continuous movement of the tip. The light yellow lines inside the pattern are the path of the tip. Since the end of the path meets the head, it presents as a close-loop three-way mark. Figure 3.4(c) shows the lifting and approaching of the tip. When the letter "U" was fabricated, the tip was lifted up and was then moved right to write the letter "K".

3.2.3 Depth of the OTSpd patterns

The depth of the OTSpd patterns were measured through the AFM contact mode in the pH 7.0 phosphate buffered saline (PBS) solution to eliminate the charge effects. Figure 3.5(a) shows a topography image of a 5×6 array of OTSpd patterns on an OTS coated silicon wafer sample. Each round OTSpd pattern has a bright dot in the center at which the tip applied bias. During the fabrication, two oxidation steps generally occur: the decomposition of the OTS molecules and the oxidation of the silicon substrate. When OTS molecules are oxidized under an electric current, the alkyl chain is partially destructed, which lowers the horizontal plane. On the contrary, the oxidation of Si increases the height. The topographical change of the OTSpd patterns combines both effects. Due to the difference of the molecular packing density and electrical field, the measurement of a specific OTSpd pattern is insufficient to represent the morphology of OTSpd patterns in general. A histogram is, thus, used here. In principle, a histogram provides the information of the population of all specific values existing within an image.

If a certain value dominates in a measurement, a peak will show up. Figure 3.5(b) is the histogram of the correlated topography image, Figure 3.5(a). Two peaks show up. One is around 5 Å and the other is at 15 Å. Correlating these two values with the fact that the OTS surface is higher than the OTSpd pattern, the difference of the heights of the peaks, 10.7±1.4 Å, is the average depth of the OTSpd patterns. Combing the results of 30 other samples, the depth of the OTSpd patterns is 10.2±0.7 Å in average.

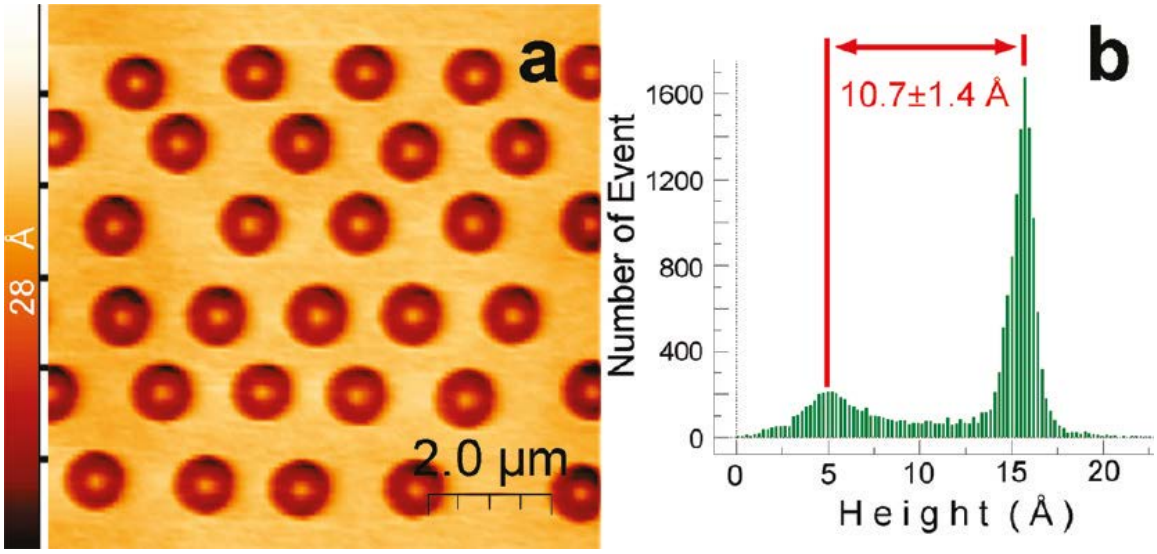

Figure 3.5. An array of the OTSpd patterns.[53] (a) The topography image of the array. (b) Histogram of the height distribution of the correlated topography image.

A parallel experiment for proving the depth of OTSpd patterns is done by preparing another layer of OTS SAM over the freshly created OTSpd patterns. Figure 3.6 shows an illustration of the height change after the layer of an OTS SAM is deposited over an OTSpd pattern. The fully extended length of OTS molecules is calculated to be about 26 Å by Gaussian 03W.[53] If the OTS molecules are filled in the OTSpd pattern with their backbones standing perpendicularly to the silicon wafer surface, the patterned

area (OTSpdOTS) will be 16 Å higher than the OTS SAM surface. The results of this experiment are shown in Figure 3.7. Figure 3.7(a) is the topography image that the second layer of OTS SAMs grew over the OTSpd patterns, and Figure 3.7(b) is the correlated phase image. The patterns in bright yellow in the topography image are higher than the OTS surface in brown. Both patterned areas and OTS surface showing the same color in the phase image suggests both areas are terminated with the same functional groups, $-CH_3$. The measurements of the height profile and the phase signals along the grey line are shown in Figure 3.7(c). The OTSpdOTS area is about 16 Å higher and the phase signals are almost constant except for two sharp peaks. Once an AFM tip moves to a pattern with different height, the side of the tip is first impacted. As a result, a negative peak shows up for the tip moving up to the surface of the OTSpdOTS pattern, while a positive peak shows up for the tip moving down. A more general measurement of the height difference is shown in Figure 3.7(d). The histogram, Figure 3.7(d), shows the OTSpdOTS patterns are generally 16.8 Å higher than the surface over the whole scanned area.

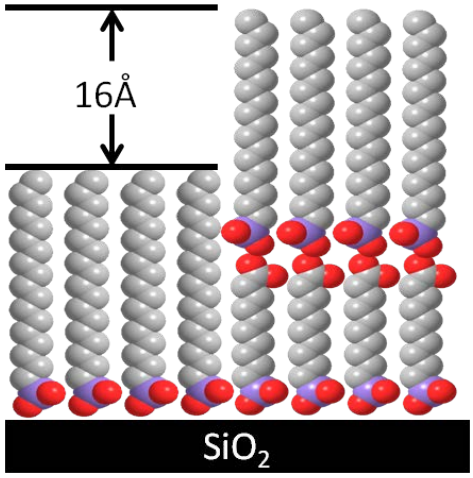

Figure 3.6. Illustration of OTS SAM deposited over an OTSpd pattern

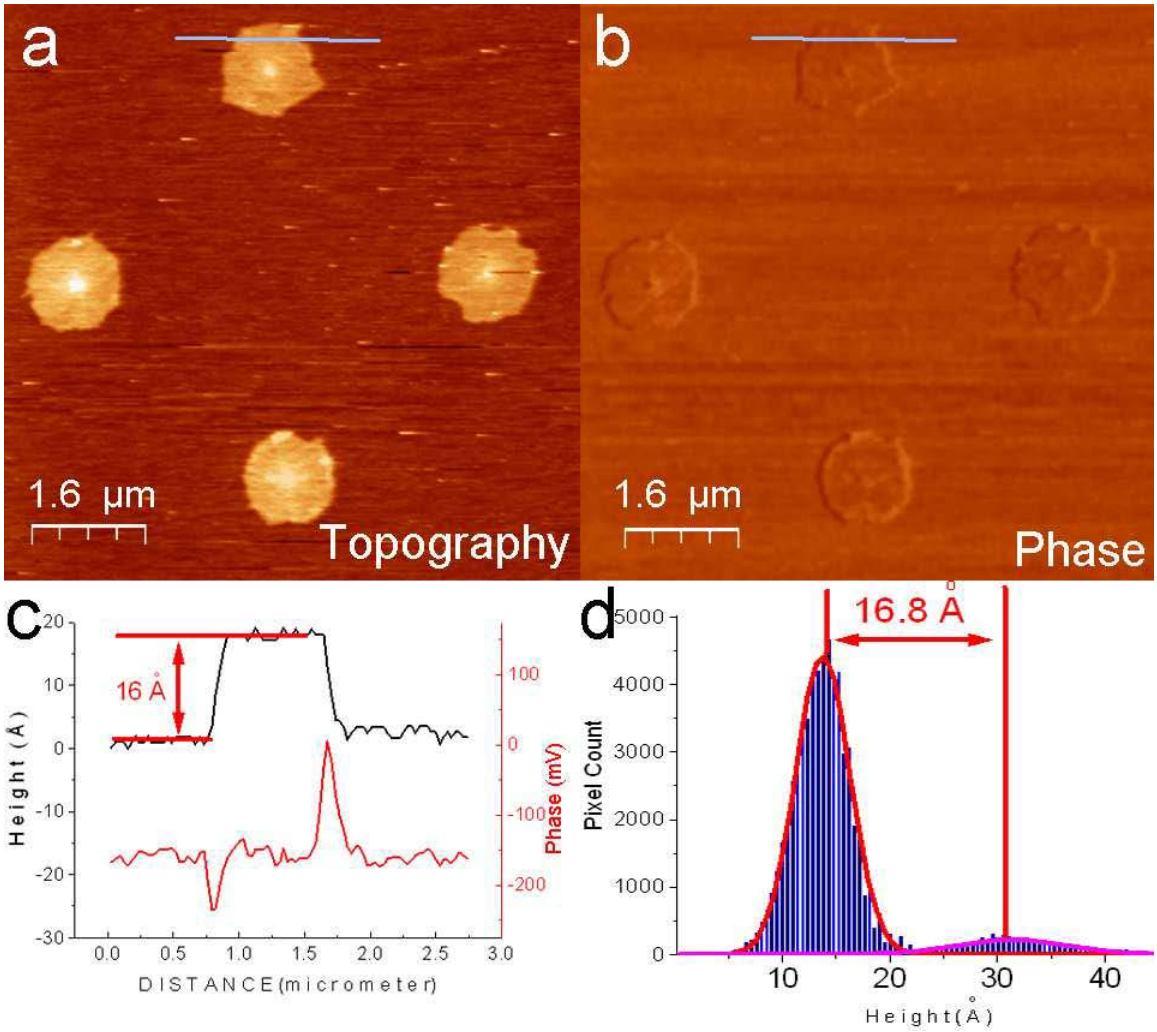

Figure 3.7. OTS SAM grew on OTSpd patterns (OTSpdOTS).[53] (a) The topography image of OTSpdOTS patterned surface. (b) The correlated phase image of (a). No phase contrast was observed. Therefore, the second layer of the OTS SAM exposed the same functional group as the first layer. (c) The measurement of both heights and phase signals along the grey line. (d) Histogram indicates a 16.8 Å height difference over the whole scanned surface.

3.2.4 Identification of the chemical properties of the OTSpd patterns

Previously two features were found in an OTSpd round pattern: a flat bottom and a center dot. According to Sagiv's reports, the oxidized alkyl groups were converted to carboxylic acid groups,[93] and the center dots or lines are believed to be silicon oxide.[90] In this part, 1-pyrenyldiazomethane (PDAM) and 1% hydrofluoric acid aqueous solution are used to identify the carboxylic acid groups and SiO_2 residues.

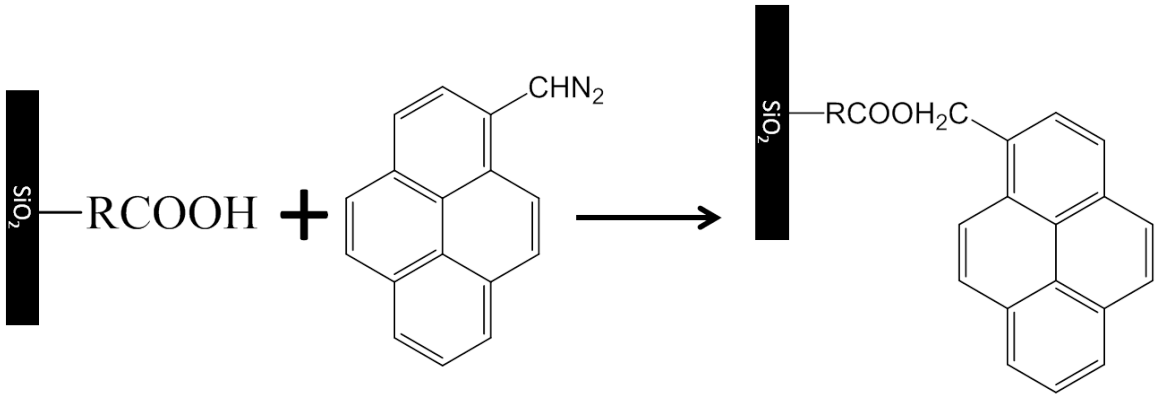

Figure 3.8. Scheme of PDAM reacting with a carboxylic acid group

PDAM is a novel carboxylic acid tagging agent. When PDAM is bound to a carboxylic acid group, the product is fluorescent at 395 nm due to the conjugation, while the free PDAM molecule is fluorescent at 319 nm. Figure 3.8 shows the scheme of PDAM reacting with carboxylic acid group on the OTSpd pattern. After the reaction, the pyrenyl group binds with the SAM through an ester group.

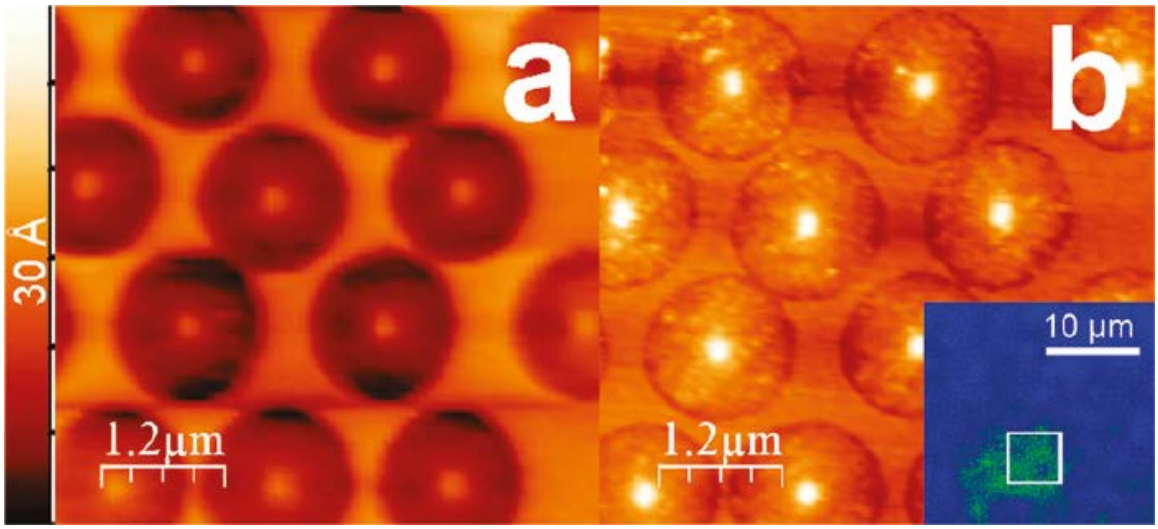

Figure 3.9. Topography images of identical OTSpd patterns before and after the reaction with PDAM.[53] (a) Topography image of OTSpd patterns before the reaction with PDAM; (b) Topography image of OTSpd patterns after the reaction with PDAM. Inlet: fluorescence image of PDAM bound OTSpd area. The bound area is shown in green and the rest area is in blue.

The surface morphologies before and after the identification reaction are shown in Figure 3.9(a) and Figure 3.9(b), respectively. The surface of OTSpd patterns in dark color are lower than the OTS surface initially in Figure 3.9(a). After the incubation in 3mM PDAM/methanol solution for 10h and thorough rinsing with tetrahydrofuran (THF), the OTSpd patterns are found filled with PDAM molecules. Further fluorescence observation was done under fluorescence microscopy equipped with GFP bandwidth filter (395nm). The light passing through the filter is shown in green in the inset (Figure 3.9(b)). Both morphology change and fluorescence response prove the binding of PDAM molecules with the OTSpd substrates. Therefore, the terminated functional groups of OTSpd patterns are confirmed to be carboxylic acid.

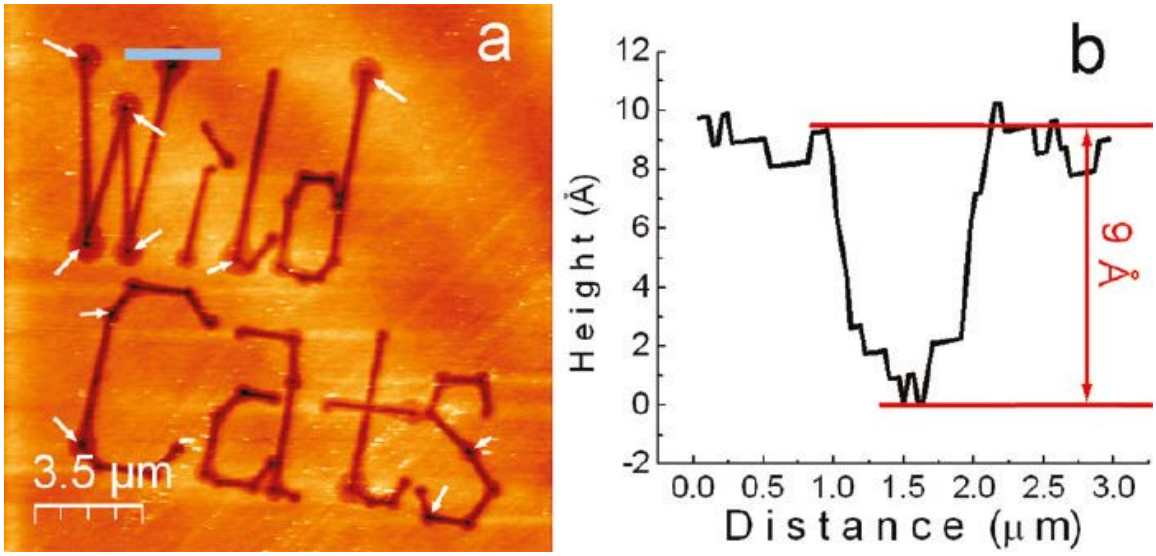

Figure 3.10. Result of a HF etching experiment.[53] (a) The topography image of an OTSpd pattern incubated in HF 1% solution for 5 min. (b) The height profile along the grey line suggests the depth of the pattern after the incubation is 9 Å.

The result of the HF etching experiment is shown in Figure 3.10. The oxidation path is normally in a bright white dot or a line as demonstrated in Figure 3.4. After the incubation in a 1% HF aqueous solution for 5 minutes, the center dots and lines turned dark in the topography image, Figure 3.10(a). This color change in topography images indicates SiO_2 is etched away and the heights of those areas are lower than the OTSpd patterns. Meanwhile, the height profile along the grey line shown in Figure 3.10(b) suggests the remaining area of the OTSpd patterns remains the same and is not composed of SiO_2.

3.3 Summary

In this chapter, a partially degraded OTS patterning technique developed previously by our group is discussed. By controlling the electric dwelling time, the size of the OTSpd pattern can be increased up to submillimeter scale. The depth of the OTSpd patterns is 10.2 Å below the OTS surface in average, and the patterns are terminated with carboxylic acid groups.

Chapter Four

STUDY OF THE SPREADING OF N-HEXATRIACONTANE OVER OCTADECYLTRICHLOROSILANE PARTIALLY DEGRADED PATTERNS

4.1 Introduction

Long-chain n-alkanes are fundamental organic compounds and are also a fundamental component in lubricants,[100-102] gasoline,[103, 104] and coating solutions.[105, 106] Understanding the spreading of the alkane over solid substrates may improve their applications.

When long-chain n-alkane spreads over a solid surface, a thin film known as the precursor film forms directly above the substrate. Although the interfacial structures of the films have already been intensively studied by X-ray diffraction,[107-109] neutron diffraction,[110-112] ellipsometry,[51] optical microscopy,[13] atomic force microscopy[113-115] etc., conflicts still exist in the results. There are two models describing the structures of the alkane films at the interfaces, the monolayer model[49] and the bilayer model[51, 109]. In the monolayer model, long-chain n-alkane molecules stand perpendicular to the surface.[47, 49] Meanwhile, the bilayer model consists of two kinds of layers, the standing-up layer and the parallel layer.[51, 52, 109] Upon the solid substrate are the parallel layers in which the long-chain n-alkane molecules lay their carbon backbones parallel to the surface. The standing-up layer forms on the top of parallel layers. Molecules in the standing-up layer pack side by side densely and either stand perpendicularly to the surface or tilt at some angles.[51, 52]

In addition to the structures, the mechanism of the formation of the films is also not clear. When spreading over a solid surface, alkane molecules transport simultaneously via two phases, liquid phase and vapor phase. However, due to technical difficulties, the contributions of liquid flowing and vapor condensation are hard to distinguish. Cazabat et al. attempted to use non-volatile materials, tetrakis(2-ethylexoxy)-silane and PDMS, to ignore the vapor of the liquid molecules,[12, 14, 38, 39, 41] and found the condensation of the molecules from their vapor was not *condicio sine qua non*.[4] On the contrary, Ajaev and Glasner found the spreading dynamics were influenced by the pre-adsorbed molecules from the vapor.[116, 117] Particularly, long-chain alkanes are volatile. The liquid phase transport and vapor phase condensation occur at the same time. Although, Basu and Nozaki found the interfacial films formed only by the vapor of the molecules had the similar structures as the films formed during the spreading,[50, 109] such results still cannot explain the relationship between the liquid phase transports and the vapor phase transport. Thus, a method that is able to present the results of both transport paths separately on a same surface is required.

Finally, the mechanical properties of the alkane interfacial films play an important role in micro-electro mechanical systems (MEMS). Although intensive studies of the mechanical properties of the methyl terminated SAMs have been reported, none of those results can be directly adopted on the alkane films.[118-120] Compared to the SAMs, such as alkanethiol and silane, alkane doesn't have the functional groups binding with the substrates. Therefore, alkane molecules in the film are easier to remove and pick up than alkanethiol and silane SAMs. A study of the mechanical properties of the alkane interfacial films is needed to reveal the difference.

In this chapter, I employ the OTSpd patterns to study the spreading of the long-chain n-alkane, n-hexatriacontane (C36). As introduced in the previous chapter, OTSpd patterns are surrounded by OTS SAM which is terminated with inert methyl groups. When spread over the OTSpd pattern, the C36 molecules in liquid phase are limited within an OTSpd pattern, while the molecules in vapor phase also condense into the isolated OTSpd patterns. Hence, the effects of vapor condensation are extracted out. I found the parallel layers are primarily formed by vapor condensation and were formed prior to liquid expansion.

Next, the methyl groups of the OTS surface provide a chemical reference to distinguish the model of the C36 films. The standing-up layer of C36 films is terminated with methyl groups which have the same phase signals as the OTS surface. If parallel layers exist in the C36 films over OTSpd surfaces, the phase signals of the parallel layers will be different. I found the C36 precursor film over the OTSpd pattern followed bilayer model and the standing-up monolayer may have different thickness due to the tilt of C36 molecules.

Furthermore, the shape of the OTSpd pattern is also used to serve as a reference for tracking the movement of the alkane molecules. Results showed the parallel layer did not move during the spreading.

Finally, the mechanical properties of the alkane film are characterized by atomic force microscopy to reveal the coefficient of friction and the penetration pressure.

4.2 Materials and instruments

Silicon (100) wafers, nitrogen doped with 13 ohm·cm resistivity, were purchased from James River Semiconductors. Octadecyltrichlorosilane (OTS, 97%) was from Gelest. n-Hexatriacontane (C36, >99%) and n-dotriacontane (C32, >97%) were both purchased from Sigma.

The OTSpd patterns were fabricated with an Agilent PicoPlus Atomic Force Microscopy (AFM) which was equipped with an environmental chamber. All the AFM tips were purchased from MikroMasch. The CSC-17/Ti-Pt tips used to fabricate the patterns were coated with Ti-Pt and generally had a force constant of 0.18±0.10 N/m. The CSC-17/No Al tips used for the frictional measurements were made from silicon and also had an average force constant of 0.18±0.10 N/m. The tips used to characterize the alkane films in tapping mode were NSC-14 whose typical spring constant was 5±2 N/m. All the AFM images were processed with WSxM.[121]

4.3 The structures of n-hexatriacontane precursor films over OTSpd patterned surfaces

4.3.1 Methods and experiments

4.3.1.1 Preparation of octadecyltrichlorosilane coated wafers

The one side polished silicon (100) wafers were first cut into one inch by one inch square pieces. After being boiled in Piranha solution (33 vol.% of H_2O_2 and 67 vol.% of conc. H_2SO_4) for 30 minutes at 130 °C, the wafers were thoroughly rinsed with deionized water and dried with compressed air. Therefore, the organic contaminants on

the wafers were completely removed, and the surface of the silicon wafers were terminated with hydroxyl groups.

Next, the cleaned wafers were incubated in 5 mM OTS/toluene solution for 10 hours at 40 °C. The OTS molecules close to the wafer surface were hydrolyzed, cross-linked, and finally reacted with the hydroxyl groups over the wafer surface. After the reaction, the wafers were withdrawn from the solution and rinsed with toluene. The physical adsorbates left over the wafer surfaces were removed by wiping the wafers with Kimwipes. Subsequently, the OTS coated wafers were kept under 100% relative humidity for another 10 hours at 40 °C for stabilizing the OTS film. Repeating the incubation and stabilization steps three times, the uniform and "pin-hole" free OTS-coated silicon wafers were ready for further use.

4.3.1.2 Spreading of n-hexatriacontane over OTSpd patterned surface

Figure 4.2 illustrates the procedure of the spreading experiment. Two steps of OTSpd fabrication were involved. All the patterns were made with the method of local probe oxidation lithography, which was described in Chapter 3. In addition, the C36 molecules were dip-coated over the OTSpd patterns by following Sagiv's "wetting driven assembly" approach.[122]

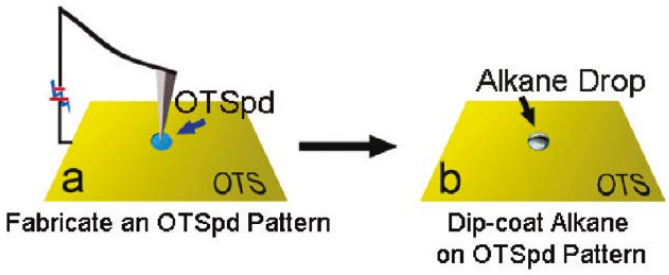

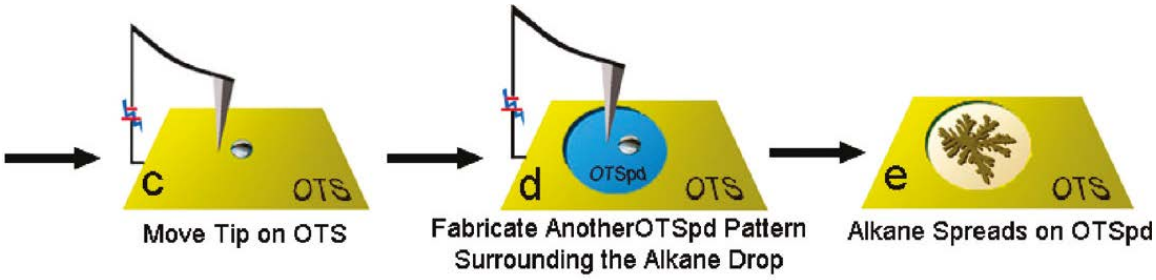

Figure 4.1. Scheme of C36 spreading over OTSpd patterned surfaces. (a) An OTSpd pattern was fabricated by local probe oxidation lithography. (b) After dip-coating, a drop of C36 molecules was immobilized on fabricated OTSpd pattern. (c) The AFM tip was moved to the place close to the frozen C36 drop. (d) A bigger OTSpd pattern enclosing the C36 drop was fabricated. (e) After heating, C36 spread over OTSpd patterned surface.

First, an OTS coated silicon wafer was connected to the AFM with a copper foil tape to form an electric circuit. A beaker of hot water was also kept in the environmental chamber of the AFM to maintain the relative humidity of the chamber at 100%. During the fabrication, a 10 V pulse was applied through the AFM tip (Figure 4.1(a)). The OTS molecules under the tip were oxidized and a round pattern was created. Typically for a 1 second pulse, the diameter of the OTSpd pattern would be 2-5μm.

Next, the C36 molecules were dip-coated over the OTSpd pattern(Figure 4.1(b)). The patterned sample wafer was vertically immersed into melted C36 liquid at 120 °C. After 3 minutes, the temperature of the sample wafer reached equilibrium with the temperature of melted C36. The wafer was then slowly withdrawn from the liquid at an estimated speed of 0.1 m/s. Since the surface tension of C36 is much lower than the OTSpd surface and is higher than the OTS surface, C36 molecule would fill in the hole of OTSpd patterns. No C36 molecules would be left over OTS surfaces during this step.

The subsequent step was to fabricate the second OTSpd pattern that enclosed the C36 molecules as illustrated in Figure 4.2(d). In this step, the AFM tip was moved toward the OTS surface nearest the C36 molecules and a 20 second 10 V pulse was applied. Consequently, a large OTSpd pattern was fabricated and enclosed the C36 source drop. This OTSpd surface would be used for C36 to spread.

Finally, the sample wafer was heated up to 90 °C for 25 seconds to let the C36 molecules spread over the OTSpd pattern. After the sample wafer was cooled to the room temperature, it was ready for characterization. Images were not taken until the final step to prevent the contamination to the C36 film during the AFM scan. The spread C36 film and the OTSpd patterns were characterized with AFM in tapping mode.

4.3.1.3 Domains in C36 precursor films

The experiment followed the same procedure as described in section 4.3.1.2. During the cooling stage, instead of letting the temperature of the wafer gradually decrease to the room temperature, the sample wafer was immediately removed from the hotplate and put on a cold steal sheet. The wafer was cooled to room temperature in less than 5 seconds. The C36 film and OTSpd patterns were also characterized with AFM in tapping mode.

4.3.1.4 Force induced change in titling angle

The C36 precursor film with domains was prepared according to the procedure described in section 4.3.1.3. The morphology of the original C36 film was first characterized with AFM in tapping mode. Then, the AFM tip was switched to CSC/17 no

Al, and the scan mode was turned to contact mode. With the engagement of the tip to the C36 film, 10 nN force was applied. After the C36 film was scanned under 10nN in contact mode, the scan mode was turned back to tapping mode to conduct a nondestructive characterization of the morphology of the C36 film. The topography images and phase images before and after the wipe in contact mode were finally compared with each other.

4.3.2 Results and discussion

4.3.2.1 Bilayer structure of the C36 precursor film

C36 molecules spread over OTSpd patterned surface and form a thin film. The shape of the C36 film over an OTSpd pattern is similar to that of the film over a SiO_2 surface. Figure 4.2 shows the morphology and phase signals of a typical C36 precursor film over an OTSpd pattern. The values of both height signals and phase signals are presented in brightness. In the topography image, Figure 4.2(a), the brightest spot is 10.4 nm higher than the darkest spot. While in the phase image, Figure 4.2(b), the maximal phase contrast is 5.2 V.

First of all, in the topography image, Figure 4.2(a), a round brown OTSpd pattern is observed. Since the original C36 source pattern has been merged into the bigger OTSpd pattern during the second fabrication (Figure4.1(d), no contours of the C36 source pattern are found here. However, two light yellow dots, labeled as oxidation spots, indicate two different positions where the pulses were applied. The "oxidation spot and C36 resource" is the place where the first electric pulse was applied and is also where C36 molecules were dip-coated. The "2nd oxidation spot" is where the second electric

pulse was applied. The dwelling time of the second pulse is much longer than the first one. Thus, the OTSpd pattern is bigger. Consequently, the second OTSpd pattern encloses the first OTSpd pattern and only one big round pattern is shown in Figure 4.2.

The depth of the pattern after spreading is measured by comparing the height signals of the patterned area to the height signals to the OTS surface. The statistical results of the heights of a typical OTSpd/OTS junction highlighted in a green square are plotted in the histogram (Figure 4.2(c)). In a histogram, the x-axis indicates the height change, while the y-axis presents the abundance of each height value in the green square. According to Cai's study, a fresh OTSpd pattern is 1.02±0.07 nm lower than the OTS surface originally.[53] In this image, the histogram indicates the height difference is only 0.46±0.09 nm. Considering the fact that the OTSpd patterned surface is darker than the OTS surface in the topography image, I speculate that OTSpd surface is 0.46±0.09 nm lower than the OTS surface. By taking the current depth of the pattern, 0.46±0.09 nm, from the average depth of fresh OTSpd patterns, 1.02±0.07 nm, 0.56±0.11 nm thick C36 molecules are filled in this OTSpd pattern. In addition, since the size of the C36 molecular cross section is about 0.45×0.45 nm^2, there could be a monolayer of C36 molecules laying parallel to the surface, denoted as parallel layer.

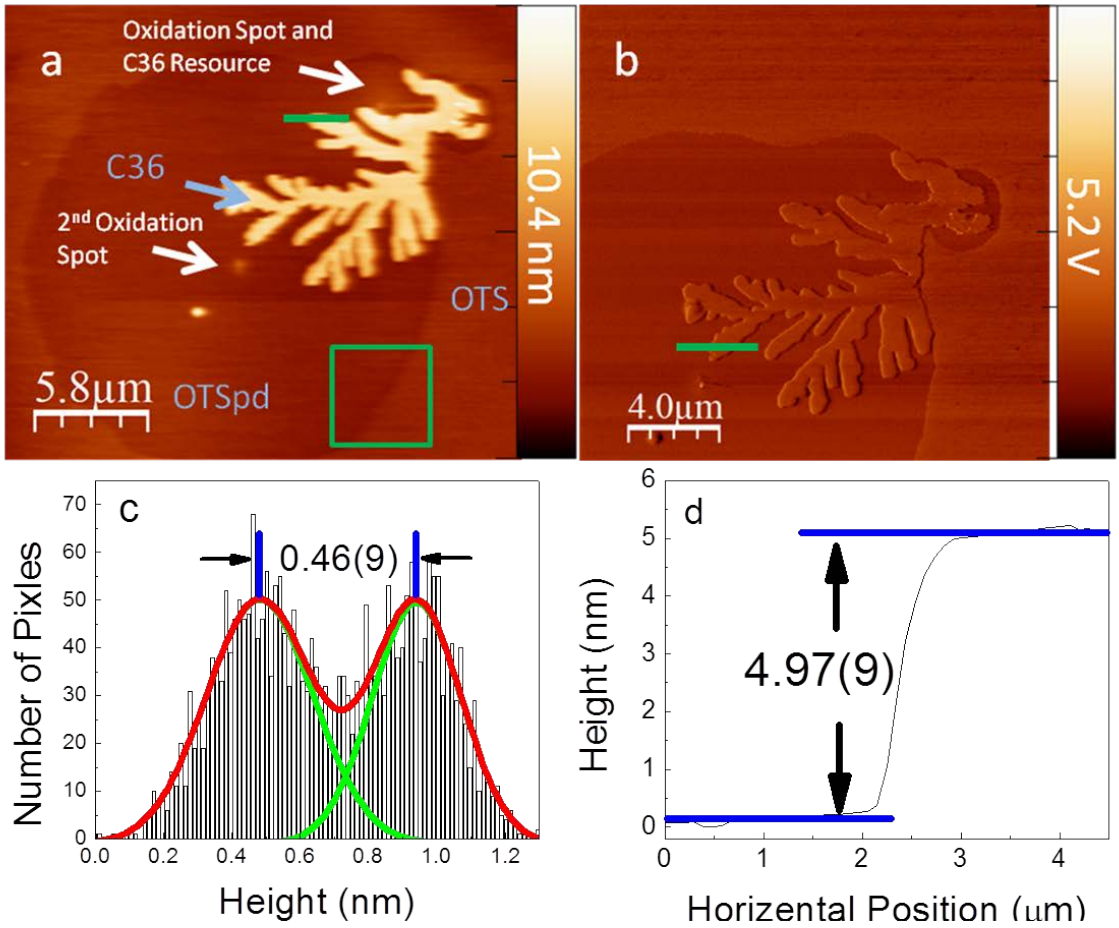

Figure 4.2. C36 precursor film over OTSpd patterned area. (a) The topography image of the precursor film; (b) The phase image of the film. The fractal and the OTS surface have the same phase signals, while the patterned area is different. (c) Histogram of the square area in the topography image, indicating the patterned area is 0.46±0.09 nm lower than the OTS surface. (d) The height profile of a branch of the fractal along the green line in the topography image, indicating the thickness of the fractal is 4.97±0.09 nm.

Another feature found in the topography image is a seaweed-shaped fractal on the top right corner of the OTSpd pattern. Since C36 was the only liquid involved in this experiment, the fractal is made of C36 molecules. Alkane molecules frozen on the

surface follow the diffusion limited aggregation (DLA) theory.[49] During the process of surface freezing, the liquid alkane molecules move along the surface until they meet the surface crystalline seeds. Once the liquid molecules come across the seeds, they stop moving and align themselves with the seed molecules in the same orientation. Consequently, a dentritic fractal forms and is enlarged. The thickness of a branch of the dentritic fractal film along the green line in Figure 4.2(a) is plotted in Figure 4.2(d). The height profile has two platforms that indicate the surface of parallel layer and the surface of the fractal. Furthermore, from the topography image the fractal surface shows brighter color than the parallel layer. Therefore, the value of the higher platform corresponds to the fractal surface, the lower platform corresponds to the surface of parallel layer, and the difference between these two values is the thickness of the fractal. From the height profile, the thickness of the C36 dentritic film is 4.97±0.09 nm. As reported by Cai, the thickness of a C36 monolayer could only be several specific values due to the interlock of the carbon backbones. If the C36 molecules stand perpendicularly to the surface, the thickness of the monolayer would be 5.02±0.03 nm.[53] Therefore, the C36 molecules found in this seaweed-shaped fractal stand perpendicularly to the surface. In this dissertation, such seaweed-shaped layer of alkane molecules is called "standing-up layer".

In addition to the topography image, the phase image (Figure 4.2(b)) of the same region also confirms the existence of both parallel layer and standing-up layer. Two colored components are found in the phase image (Figure 4.2(b)). The seaweed-shaped fractal and the OTS surface are slightly brighter, while the rest of the OTSpd patterned area is darker. Since the phase signals reflect the interactions between the surface species and the AFM tip in tapping mode, these signals generally imply the similarities of the

chemical identities detected by a tip. In this phase image, because the color of the standing-up layer is the same as the color of the OTS surface, the surface of the standing-up layer possesses the same functional groups as the OTS surface, while the OTSpd surface possesses the other kind of functional groups. For a C36 molecule, there are only two kinds of functional groups, methyl group ($-CH_3$) and methylene group ($-CH_2-$). The standing-up layer of C36 molecules must be terminated with the methyl groups that are also the exposed functional groups of OTS, whereas the C36 molecules in the parallel layer expose mostly methylene groups.

In summary, the film of C36 molecules spreading over the OTSpd patterned surface shown in Figure 4.2 is composed of two kinds of layers, the standing-up layer and the parallel layer. In the parallel layer, C36 molecules lay parallel to the surface, while C36 molecules stand perpendicularly to the surface in the standing-up layer. By observing 30 more samples, I found all C36 films contain both parallel layers and standing-up layers. The thickness of the parallel layers vary from 1-5 molecules. The molecules in the standing-up layer do not always stand perpendicularly to the surface; they may tilt at certain angles. When long-chain n-alkane molecules are packed side by side, they are straightened in all-trans form in which all the carbons are in the same plane and in zigzag shape. Therefore, in order to reach the minimal distance between the neighboring molecules, the alkane molecules are interlocked by their carbon teeth. Consequently, the neighboring alkane molecules, such as C36, would have 36, 35, 34 or fewer carbons coupled with each other. Particularly for a C36 molecule, when 36 carbons are coupled with its neighboring molecules, it stands perpendicularly to the surface. If a C36 molecule only has 34 carbons coupled with its neighboring molecule, in order to

have all the molecules stand on the surface straightly, the molecules have to tilt at certain angles. Therefore, due to the different number of coupling carbons, the thickness of the standing-up layers is found to be 5.02±0.03 nm, 4.43±0.03 nm, 3.88±0.04 nm and 3.41±0.06 nm which correspond to 36, 34, 33, and 32 coupling carbons.

4.3.2.2 Verification of the bilayer model

There are two models describing the structures of the long-chain alkane precursor films over the silicon oxide surface, the monolayer model[49] illustrated in Figure 4.3(a), and the bilayer model[51] illustrated in Figure 4.3(b). Riegler proposed the monolayer model in which alkane molecules standing perpendicularly over the SiO_2 surface formed a monolayer. If the monolayer was not big enough to cover the whole SiO_2 surface, some alkane molecules would lay parallel to increase of the coverage of the SiO_2 surface.[49] However, Taub observed the precursor film through very high resolution ellipsometry and concluded that the perpendicular layer was not directly on the SiO_2 surface. Instead, it was sitting on the parallel layers of alkane molecules.[51] He called the structure as a bilayer model. Here, the structure of the C36 precursor film over an OTSpd surface is distinguished by height analysis.

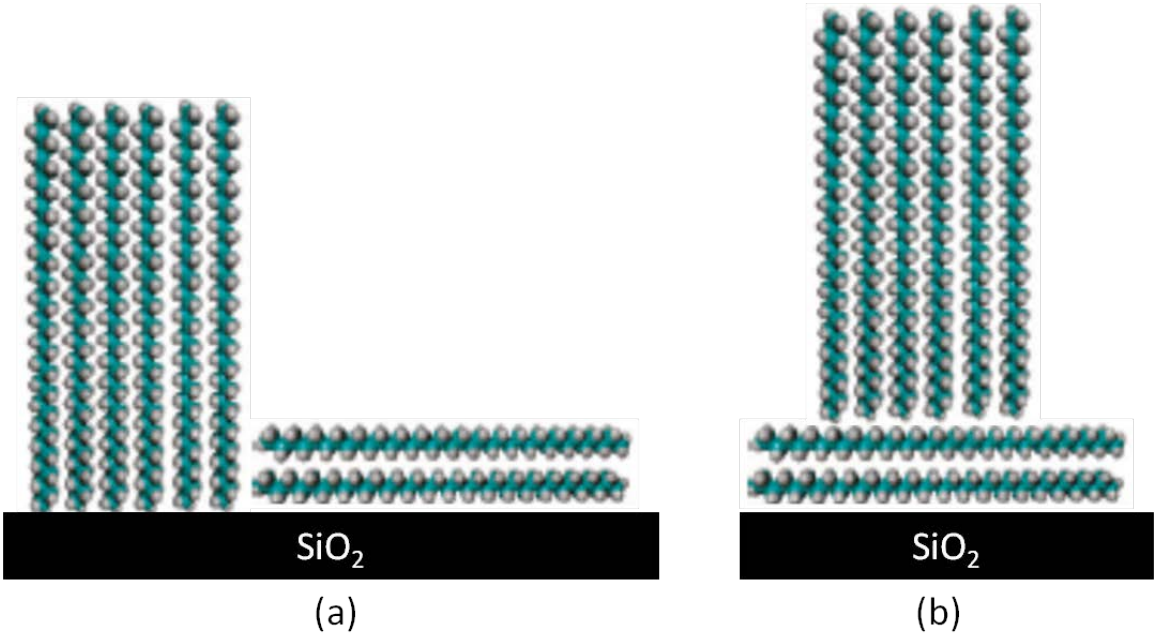

Figure 4.3. The illustrations of monolayer model and bilayer model. (a) The illustration of the monolayer model. Long chain alkane molecules stand perpendicularly and on the silica surface and form dentritic film. The remaining silica surfaces are covered with alkane molecules that lie with their long-axis carbon backbone parallel to the surface. (b) The illustration of the bilayer model. The silica surface is directly covered with layers of alkane molecules lying parallel. Layers of alkane molecules standing perpendicularly to the surface are on the top of these parallel layers.

In the previous section 4.3.2, C36 molecules are found standing perpendicularly on the parallel layer. The sum of the thickness of both layers is 5.53±0.14 nm, which is larger than the length of a C36 molecule, 5.02 nm. Undoubtedly, the precursor film follows the bilayer model. In other circumstances, the total thickness of the parallel layers and the standing-up layer may not exceed the length of the C36 molecules. Figure 4.4 shows a sample in which the total thickness is below 5.02 nm . In the topography image

Figure 4.4(a), the parallel layer of C36 has the same height as the OTS surface; and the boundary line is barely distinguishable. Since the average depth of the OTSpd pattern is 1.02±0.07 nm, the thickness of the parallel layer is estimated to be 1.02±0.07 nm as well. The histogram, Figure 4.3(c), of the whole topography image shows the standing-up layer is only 3.4±0.2 nm higher than the parallel layer. If the precursor film follows the monolayer model, the thickness of the film must be around 5.02 nm. However, in Figure 4.3, the sum of the thicknesses of the parallel layers and standing-up layer is only 4.4±0.02 nm, which contradicts Riegler's hypothesis that alkane molecules must stand perpendicularly to the surface.[48, 49] Thus, the precursor film of this sample also follows the bilayer model.

For both samples, Figure 4.2 and Figure 4.4, the thickness of the precursor film is either larger or smaller than the full length of a C36 molecule. It is rational to exclude the possibility of Riegler's monolayer model in the structures of C36 precursor films over OTSpd surfaces. Therefore, I conclude that the C36 precursor films over OTSpd surfaces follow the bilayer model in which a standing-up layer stacks on the top of the parallel layers. Moreover, further kinetic study in the following sections shows the parallel layer forms prior to the standing-up layer and reconfirms the bilayer structure of the C36 precursor film over OTSpd surface.

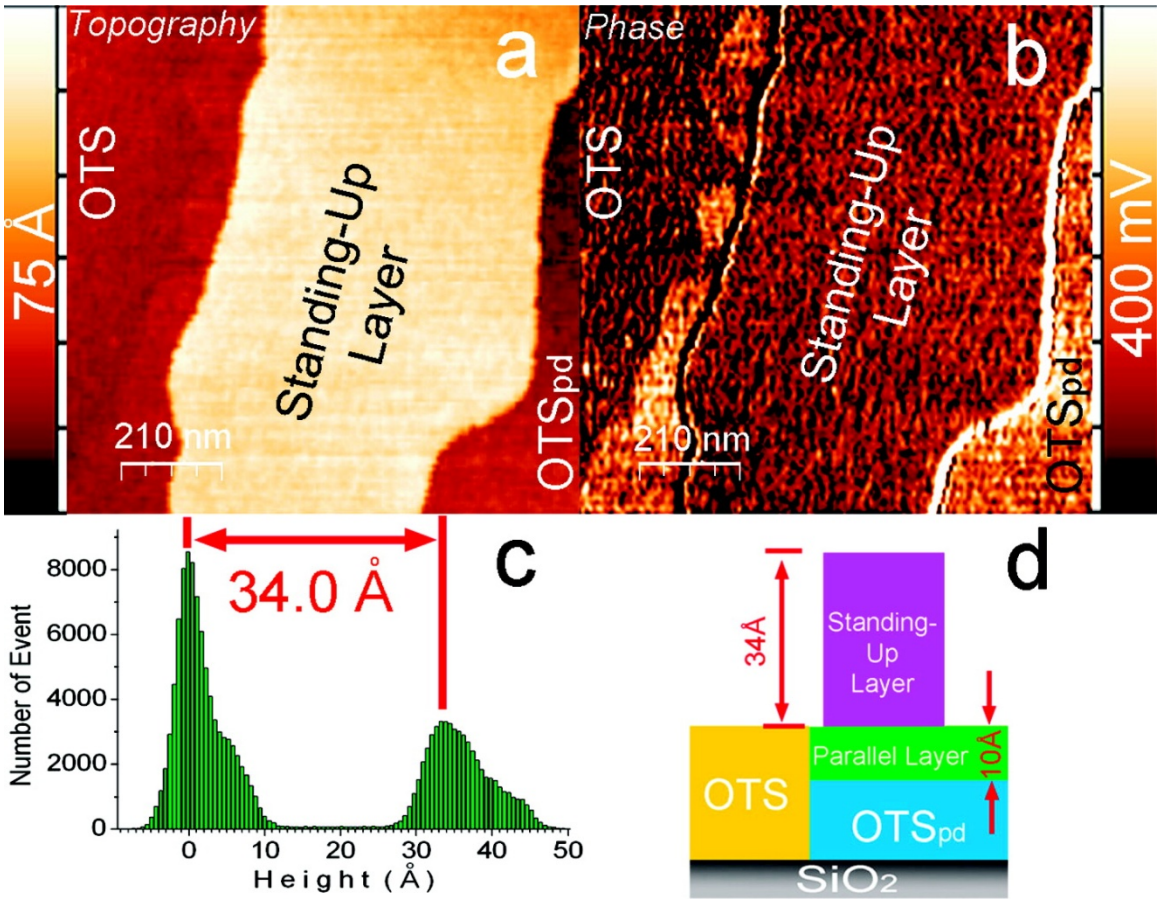

Figure 4.4. A representative patch of a C36 precursor film (a) The topography image. (b) The corresponding phase image. (c) The histogram of the topography image. The standing-up layer is about 3.4 nm thick. (d) The model to illustrate the structure of the precursor film.

4.3.2.3 Standing-up layer is composed of different domains

The thickness of the standing-up layer was observed to have some specific values, 5.02±0.03 nm, 4.43±0.03 nm, 3.88±0.04 nm and 3.41±0.06 nm with respect to 0, 2, 3, and 4 methylene group shifts along the alkane long-axis carbon backbones.[53] Those shifts were not only observed in different spreading samples, but were also found within the branches of a single fractal.

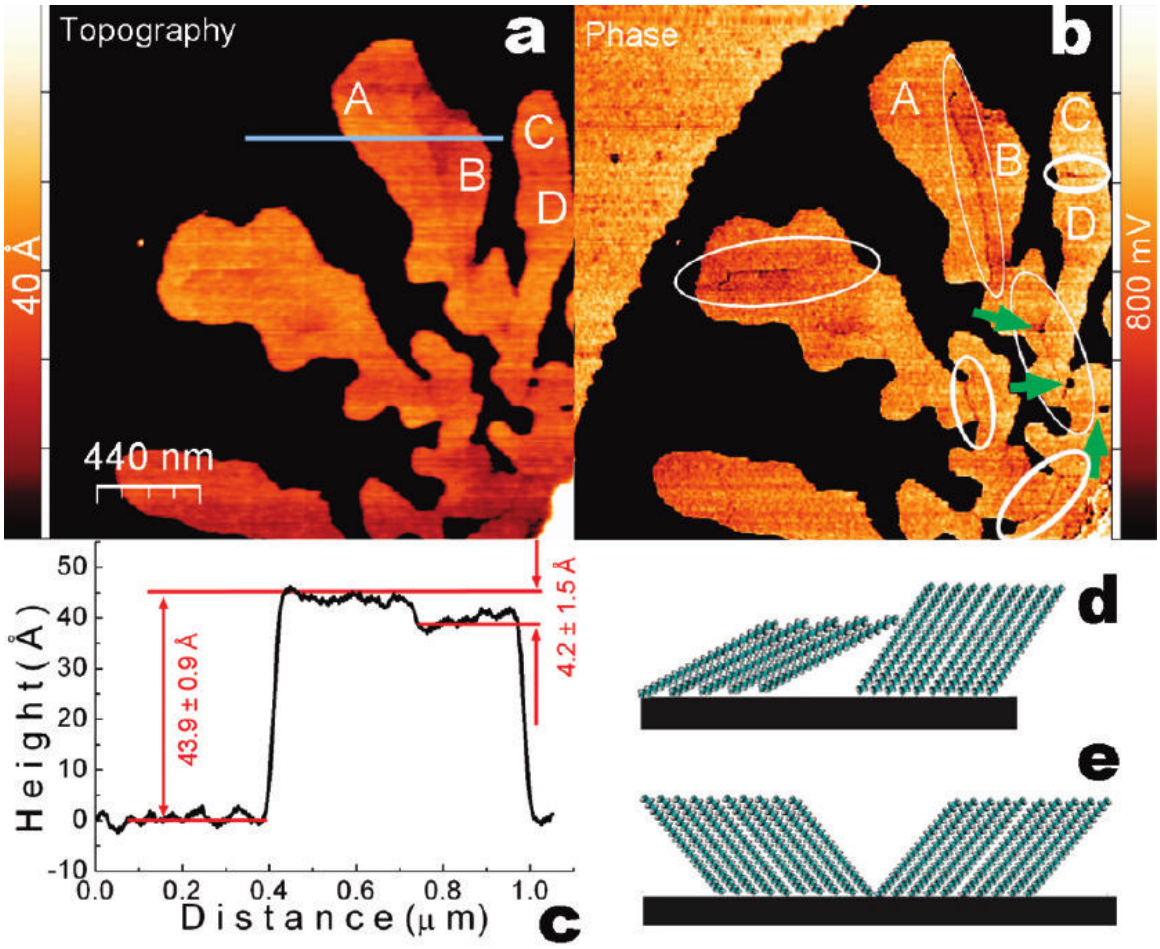

Figure 4.5. Multi-domain structure within the standing-up layer. (a) Topography image of a C36 standing-up layer. (b) The corresponding phase image. The white circles indicate the domain boundaries. The green arrows point to holes within the standing-up layer. Those holes are always on the boundary lines, indicating the coalescent process of domains. (c) The height profile corresponds to the grey line in the topography image. (d) Structural model of domains possessing different heights due to different molecular tilting angles. (e) Structural model of domains with same height but molecules are tilting in different direction.

Figure 4.5 shows the branches of a representative C36 standing-up layer. In a branch, Figure 4.5(a), two domains are labeled as A and B. The color change between domain A and domain B along the grey line indicates a change of the thickness of the standing-up layer. Based on the height profile, Figure 4.5(c), the bright part of the branch is 4.39±0.09 nm, which corresponds to a two-methylene-group shift of two neighboring C36 molecules, while the dark part of the branch is 0.42±0.15 nm lower, which corresponds to a three-methylene-group shift of two neighboring C36 molecules. The phase signals of both domain A and domain B shown in Figure 4.5(b) are similar, indicating molecules of both domains are terminated with methyl groups. Furthermore, a dark line separating the domain A and domain B implies the independence of the domains. During the freezing process, domain A and B were growing from the two different seeds and merging toward each other.

Despite domains having different thickness, they may also have different tilting directions. Domains labeled as C and D in the Figure 4.5(a) and (b) have the same thickness. In the topography image, both domains have the same color indicating they have the same height. However, a dark boundary line is found separating the domains in the phase image (Figure 4.5(b)). If the domains expand with their molecules tilting in the same direction during the surface freezing process, they should fuse together. No boundary line is expected, according to the DLA theory. Here, the boundary line indicates the molecules in the domains do not share the same orientation. As a result, domain C and domains D failed to fuse into each other. Since both domains have the same height, I speculate that the molecules in both domain C and domain D are tilting at the same angle but in different directions. Once both domains expanded and met each

other, the molecules on the edge could not be aligned and formed the boundary line. Similar phenomenon is also observed and highlighted in white circles in Figure 4.5(b).

The illustrations of Figure 4.5(d) and (e) summarize both scenarios of the domains. In one circumstance, molecules in different domains tilt at different angles. In the other circumstance, although molecules are tilting at the same angle, they are tilted in different directions. Similar phenomena were also observed in C32 precursor films. The boundary lines and holes in Figure 4.6 confirm the existence of domains in C32 precursor films.

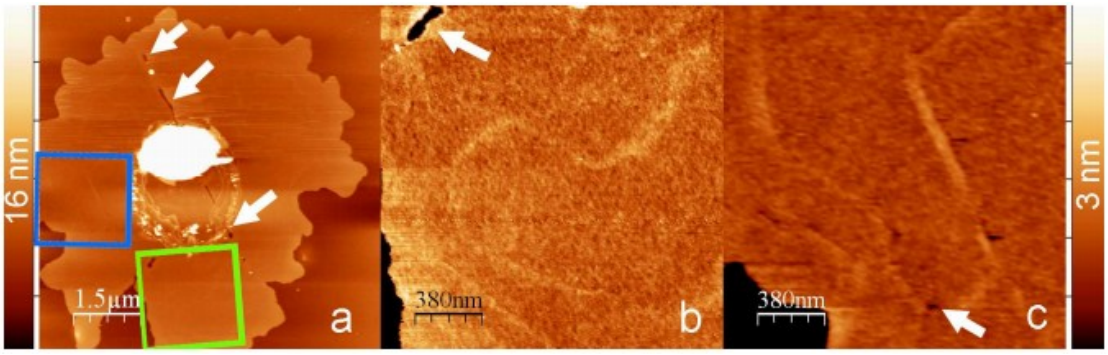

Figure 4.6. The multi-domain structure in a C32 film. (a) The topography image of a C32 precursor film over OTSpd patterned surface. (b) The topography image of the area in green square in part (a). (c) The topography image of the area in blue square in part (a).

4.3.2.4 Force induced change of the tilting angle

The formation of a seaweed-shaped fractal is normally due to the energy favorite during the undercooling process.[49] According to theoretical calculations, the free energy change for each methylene-methylene pair between aligned alkane molecules is -0.93kcal/mol.[123] However, such ordered alignment also reduces the entropy of the alkane films. As a result, the alkane precursor films flow out of the source drop and flow back

into the source drop at the same time.[47] In other words, the energy barrier for detaching 36 methyl or methylene pairs between the neighboring molecules is not too high. The force induced change of the tilting angles takes advantage of this property. The process is generally composed of two steps, breaking the interaction between two neighboring molecules and then re-aligning the neighboring molecules. The energy required for breaking the interaction between the molecules is similar to the energy of ditaching the molecules, which is also not too high. Moreover, under external pressures, the molecules will be pushed down and lose their original orientations. When molecules restore their alignments, the process is in favor of enthalpy and hence happens spontaneously. Thus, the molecules in the restored film may have different orientations.

Figure 4.7 shows the comparison of a branch of the fractals wiped by an AFM tip in contact mode under 10nN loading force. Figure 4.7(a1), (a2), and (a3) are the topography image, phase image, and height profile before wiping, while Figure 4.7(b1), (b2), and (b3) are the corresponding results after wiping, respectively. All the images were captured in tapping mode to prevent further damage to the C36 film.

Initially, the branch contains different domains as shown in the topography image, Figure 4.7(a1). Measuring the height along the white line, I find two different heights of the domains, 3.4 nm and 3.9 nm, which indicate the molecules tilt 48° and 40° to the surface norm, respectively. The phase image, Figure 4.7(a2), also confirms the existence of those domains that are separated by the boundary lines.

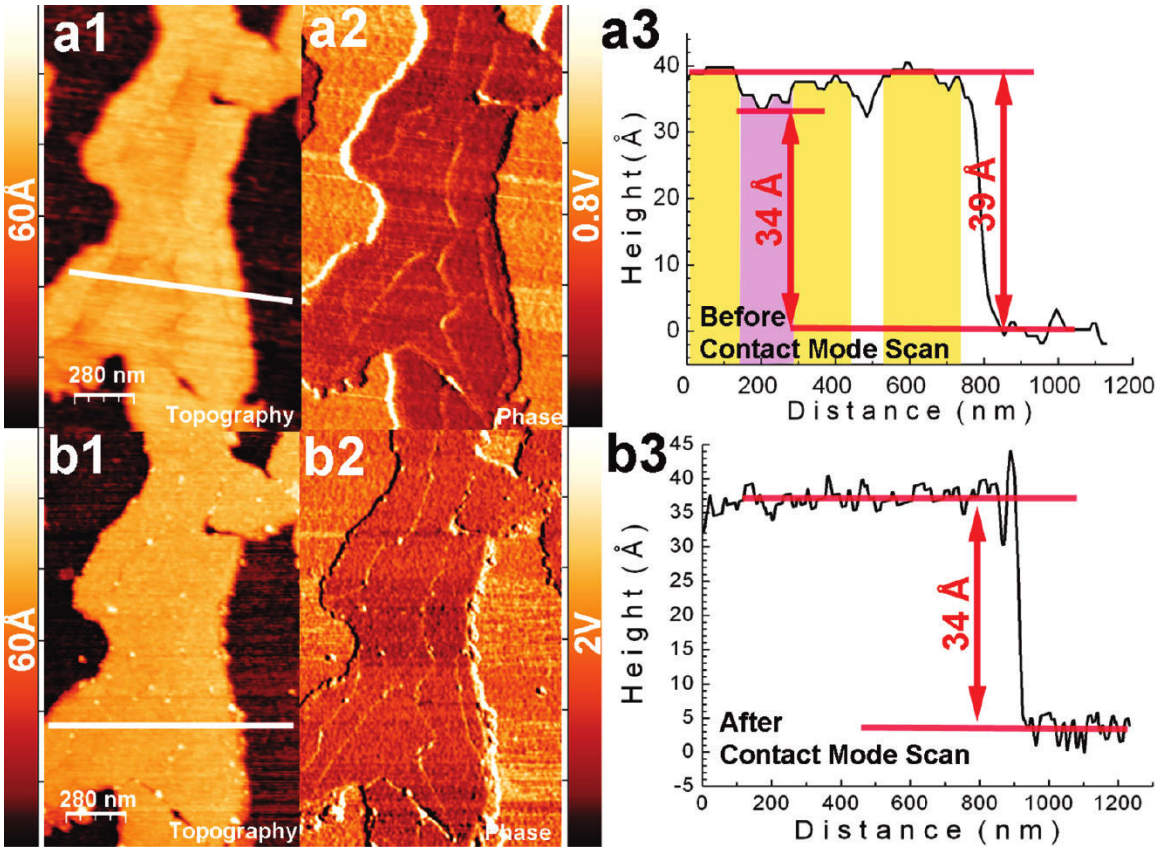

Figure 4.7. Force induced change of the molecular tilting angles during the contact mode scan. (a1), (a2) and (a3) are the topography image, phase image and the height cross-section along the white line in a1 before the wiping, respectively. (b1), (b2) and (b3) are the corresponding topography image, phase image and the height cross-section along the white line in b1 after the wiping, respectively. All the AFM images were captured in tapping mode. The domain height decreases from 3.9 nm to 3.4 nm.

After the tip wiped over the C36 film in contact mode, the height difference disappeared. All the domains reveal the same color in the topography image (Figure 4.7(b1)), and the thickness of the film is measured to be 3.4±0.2 nm, which is the same height as the lower domain before the contact mode scan. Since the solidified precursor film could preserve its shape and thickness for more than 5 days,[53] the external force

induced by the tip is the only driving force that changes the molecular tilting angles. Contrary to the change of tilting angles, the shapes of the domains still persisted after the contact mode scan. Comparing both phase images Figure 4.7(a2) and (b2), I find the boundary lines remain in their original positions, while a series of white spots are observed on the domain boundaries. The phase signals of those dots are neither the same as the parallel layer nor the same as the standing-up layer. They are speculated to be the glassy phase of the alkane molecules. During the contact mode wiping, the domains were pushed down from 3.9±0.2 nm to 3.4±0.2 nm. As a result, the density of the C36 molecules in the film decreases 13%. Although the AFM tip may carry the molecules off the film, some molecules may also drop from the tip and formed the glassy phase drops on the domain boundaries.

In summary, the tilting angles of C36 molecules in standing-up layer could be changed by external forces. An originally 3.9±0.2 nm thick layer of C36 molecules turns to 3.4±0.2 nm thick after wiping by AFM tip under 10nN loading force. This observation generally agrees with Taub's ellipsometry results that alkane molecules in standing-up layer may tilt at several different angles. In addition, this observation also excludes the monolayer model that the thickness of the alkane precursor film is constantly equivalent to the length of the molecules. Thus, the bilayer model of the precursor film of C36 over OTSpd surface is reconfirmed.

4.3.3 Conclusions

C36 molecules spread over OTSpd patterned surfaces form precursor films. The size and the structure of the films were carefully characterized with AFM. According to

the height analysis and the contrasts of phase signals, the films are found to consist of two kinds of layers: the parallel layers and the standing-up layers. As illustrated in Figure 4.8, the standing-up layers sit on top of the parallel layers. One to five layers of C36 molecules are found in the parallel layers where C36 molecules lie with their carbon backbones parallel to the surface. Meanwhile in a standing-up layer, C36 molecules straighten their carbon backbones and align with their neighboring molecules. Due to the zigzag-shaped carbon backbones, the straightened C36 molecules are interlocked with the carbon teeth. Consequently, only 0°, 29°, 40° and 48° tilting angles of the molecules are found in the standing-up layers.

On a silica surface, the argument of the structure of a long-chain n-alkane precursor films focuses on two models, the monolayer model and the bilayer model, which were proposed by Riegler and Taub, respectively. In the bilayer model, the standing-up layer sits on top of the parallel layers. While in the monolayer model, the parallel layers fill the gaps between the patches of standing-up layers, and the molecules in standing-up layer always stand perpendicularly to the surface. In this section, the thickness of a precursor film varies sample by sample. It does not always equal to the length of a C36 molecule. Therefore, the monolayer model of C36 precursor film over OTSpd surface is excluded. The C36 precursor films over OTSpd surface follow the bilayer model.

Furthermore, different domains are found in the standing-up layer. Within a domain, molecules tilt at the same angle. Molecules may tilt at different angles between the domains. By applying external forces on the domain-structured fractals, the molecules in the thicker domain are pushed down to comply with the orientation of the molecules in the thinner domain. Such change in the orientation of the standing-up molecules further

confirms that long-chain n-alkane molecules in the standing-up layer may not always stand perpendicularly to the surface.

In sum, the structure of a C36 precursor film over an OTSpd pattern is explored and discussed in this section. The full understanding of the structure may serve as the basis for the further study on the spreading mechanism and the stability of the C36 precursor films over OTSpd patterned surfaces.

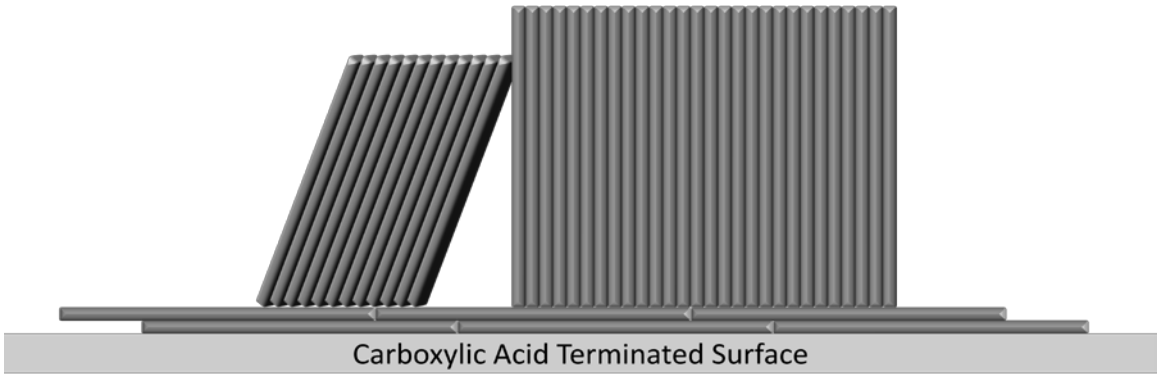

Figure 4.8. Illustration of the bilayer structure of the C36 precursor film over OTSpd surface.

4.4 Role of vapor-phase mass transport during the spreading

During the spreading process, the transport of the liquid molecules were mainly considered through the liquid flow.[4, 11] Although vapor condensation was one of the formation mechanisms of a precursor film, it was hard to be extracted from the liquid flow and was not studied separately. Generally, in the reported experiments, liquids were spread over Si, SiO_2, HOPG or silane surfaces. In spite of different surface tensions, all those surfaces were featureless. The interfacial film was formed both by the molecules

from the vapor phase and also from the liquid phase. Since both vapor phase transport and liquid phase transport took place at the same time and form the films along with each other, it was hard to distinguish the contribution from each phase.

An OTSpd patterned surface consists of two chemical features, carboxylic acid surface where both transport mechanisms are allowed and methyl group surface where the liquid flow is inhibited. In this part, I take advantage of the different surface properties of the OTSpd patterned sample to limit the flow of liquids. A series of separated carboxylic acid terminated OTSpd patterns were fabricated on the same surface. When an alkane drop spread within one of the patterns, the vapor of the alkane molecules adsorbed onto all OTSpd patterns and formed thin films. By comparing the OTSpd patterns where the alkane drop spread and the OTSpd patterns where only alkane molecules from the vapor were adsorbed, I separated the effects of vapor phase transport. The results showed that the vapor condensation played an important role during the spreading. When alkane spreads over a high energy surface, the molecules formed parallel layers through vapor phase transport. Instead of flowing directly on the solid substrate, the liquid flowed on the parallel layers.

4.4.1 Methods and experiments

4.4.1.1 Preparation of OTS coated silicon wafer and fabrication of OTSpd patterns

One side polished silicon (100) wafers were cleaned with Piranha solution (33 vol.% of H_2O_2 and 67 vol.% of conc. H_2SO_4) for 30 minutes at 130 °C before being incubated in 5 mM OTS/toluene solution. After 10 hours' incubation, the wafers were rinsed with chloroform to remove the physical adsorbed OTS molecules. Subsequently, the wafers

were kept under 100% relative humidity for another 10 hours at 40 °C to stabilize the OTS film. The incubation and the stabilization steps were repeated three times and the uniform and pin-hole free OTS coated silicon wafers were ready for further use.

The fabrication of OTSpd patterns followed Cai's local probe oxidation lithography method. The experiment was conducted in the AFM environmental chamber with 100% relative humidity. A 10 V pulse was applied through a Pt-Ti coated AFM tip on the OTS film. Along with the water vapor, the electric current oxidized the OTS molecules and partially degraded the OTS films. The patterns obtained were 1.02 nm deeper than the OTS surface and were terminated with carboxylic acid groups.

4.4.1.2 Study of C36 molecules transporting via their vapor phase

Figure 4.9 illustrates the scheme of the vapor phase mass transport experiment. A small OTSpd pattern was fabricated and dip-coated with C36 molecules using the same procedure described in the previous section. The rest of the OTS surface terminated with methyl groups has low surface energy and naturally prevents C36 molecules overflowing from the high energy OTSpd patterns. The subsequent step is to fabricate satellite OTSpd patterns that are isolated from the dip-coated C36 molecules. A fast scan is conducted first to position the dip-coated C36 molecules. Then, 1 s 10 V pulses are applied 5-25 μm away from the C36 molecules to create satellite OTSpd patterns. Normally, the diameters of those patterns are around 2 μm. Therefore, all the satellite patterns are surrounded by OTS films. Finally, a 20 s, 10 V pulse is applied next to the C36 molecules. A big main OTSpd pattern is fabricated enclosing C36 molecules. It will serve as the pattern where C36 molecules spread. No scans are conducted during the fabrication of the satellite

patterns and the main pattern to prevent the contamination of the newly created OTSpd patterns by C36 molecules.

Finally, the sample wafer is heated up and then cooled to room temperature. All the images are captured with AFM in tapping mode.

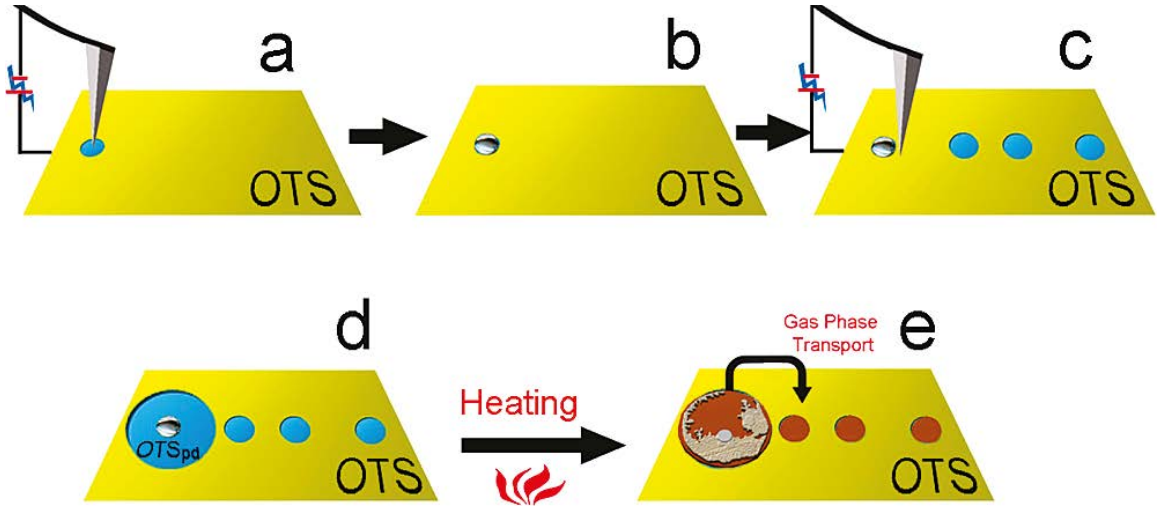

Figure 4.9. Scheme of study of vapor-phase mass transport during the spreading. (a) A 3μm diameter pattern was fabricated through local probe oxidation lithography method. (b) C36 was dip-coated onto the OTSpd pattern. (c) A series of 2-4 μm diameter OTSpd patterns were fabricated 2-20 μm away from the C36 drop. (d) The alkane drop was enclosed by a main OTSpd pattern that did not connect to other OTSpd patterns. The fresh patterns are illustrated in blue. (e) Illustration of the spreading results that molecules transport to the unconnected patterns through vapor phase transport. The experimental conditions for the spreading are 90 °C and 25 s, while the conditions for the control experiment are 70 °C and 25 s.

4.4.2 Results and discussion

4.4.2.1 C36 molecules adsorbed over OTSpd satellite patterns after spreading

A representative result of the C36 spreading with satellite OTSpd patterns is shown in Figure 4.10(a). The bilayer structure of the alkane film that a seaweed-shaped standing-up layer sitting on a parallel layer of C36 molecules is observed over the main pattern. The phase signal of standing-up layer is -2.0±0.2 V, which is the same as the OTS background. The phase signal of parallel layer is 0.12±0.05 V, which is significantly higher than the standing-up layer.

Two satellite patterns are also found in Figure 4.10(a). One is next to the main pattern, and the other is highlighted in a green square located in the up left corner of the topography image. Both satellite patterns show positive height contrasts to the OTS background, indicating the deposition of C36 molecules over the patterns. Other satellite patterns beyond the scan range, shown in Figure 4.10(b)-(e), have the similar features that alkane molecules are filled in the patterns. Since the flowing of liquid alkane was limited within the main pattern, the C36 molecules in the satellite patterns must be condensed via vapor phase transport.

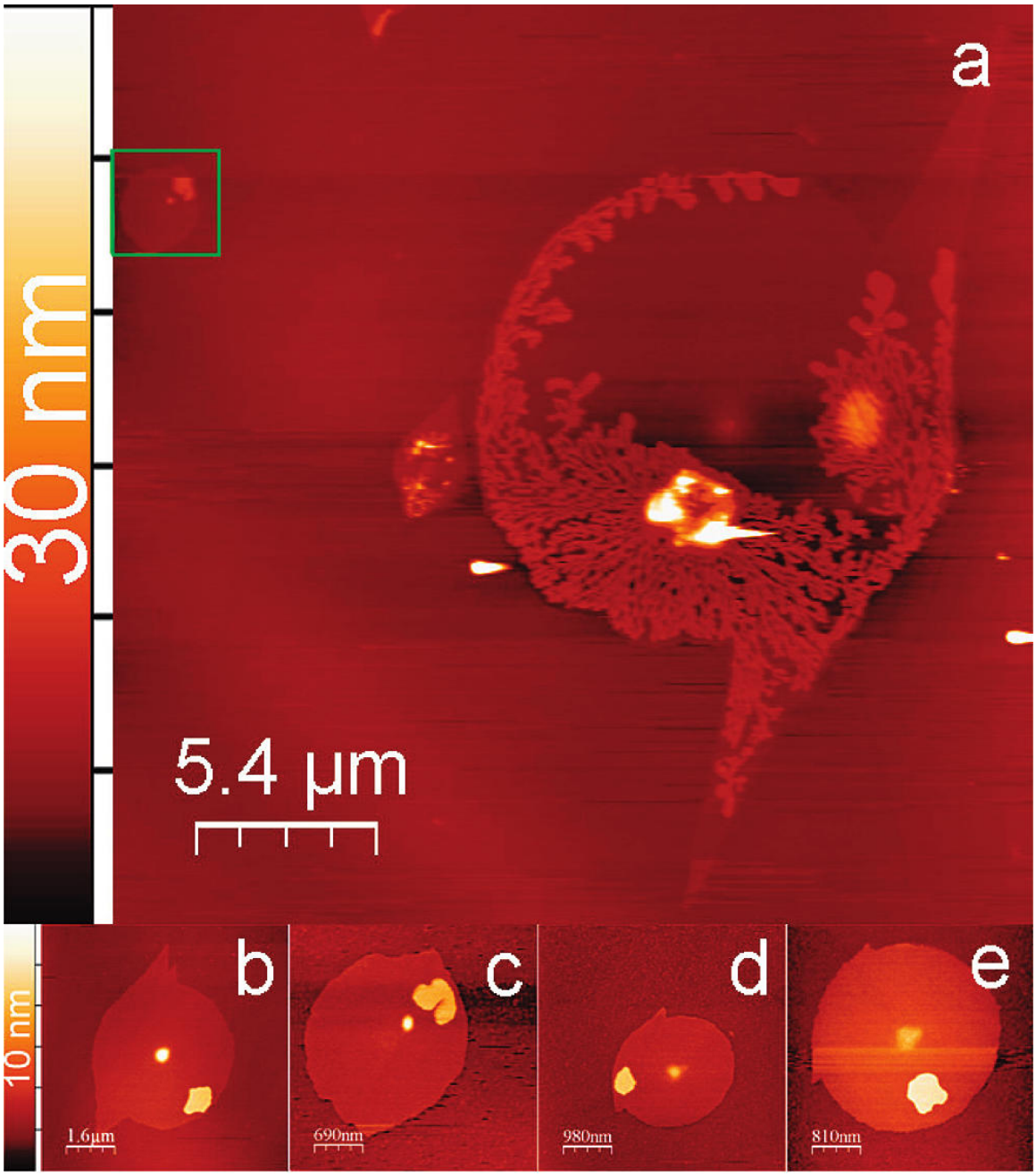

Figure 4.10. Topography images of the main pattern and the satellite patterns. (a) the main OTSpd pattern where alkane spread over. Two satellite patterns are covered with alkane molecules, (b)-(e)

The structural analysis of the C36 film over an OTSpd satellite pattern is shown in Figure 4.11. The topography image, Figure 4.11(a), and its correlated histogram, Figure 4.11(c), confirm the bilayer-structured C36 precursor film that C36 molecules cover the whole patterns with a small patch sitting on the top. Because of the depth of the OTSpd pattern, the thickness of the parallel layer is 1.89±0.4 nm which is about 4 layers of C36 molecules laying parallel to the surface. The thickness of the patch, 3.95±0.27 nm above the parallel layer, suggests the molecules are tilting 40° to the surface norm. In addition, the phase image Figure 4.11(b) also confirms the bilayer structure that the parallel layer has different phase signals from the methyl groups.

Generally, the absolute values of phase signals are not used for the comparison between different samples due to their sensitivities to the imaging conditions. However, in this study, the C36 precursor films in both main pattern and satellite patterns were captured at the same time, which makes the comparison of the phase signals valid. As mentioned before, the phase signal of the parallel layer over main pattern is 0.12±0.05 V. The phase signal of the parallel layer over the satellite pattern is characterized to be 0.19±0.08 V, which is insignificantly different from the value of the parallel layer over main pattern. Thus, I can conclude precursor films formed over the satellite patterns are composed of the same material, C36 molecules, as that over the main OTSpd pattern.

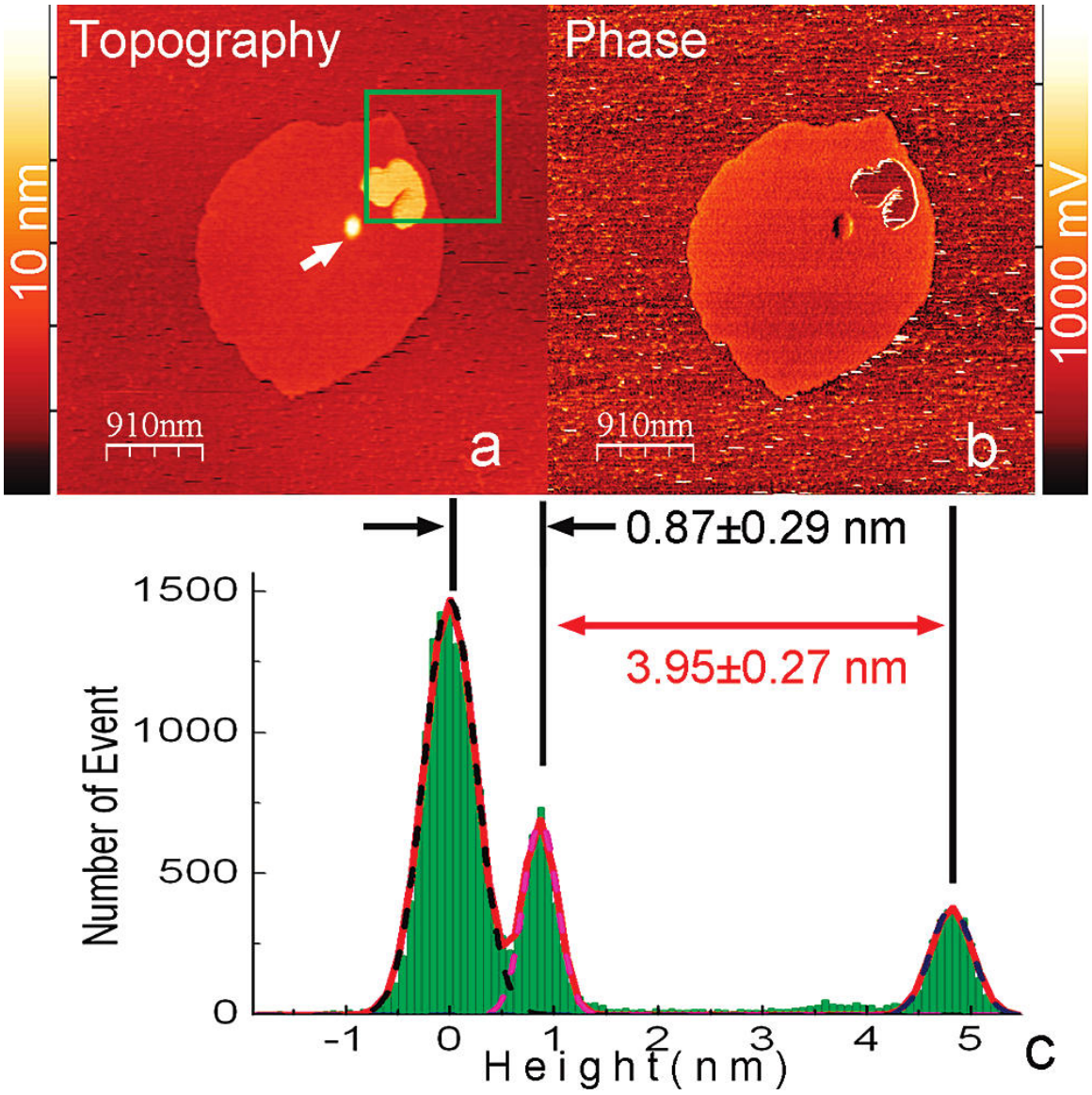

Figure 4.11. The C36 film over a satellite OTSpd pattern. (a), (b) are the topography image and phase image captured in tapping mode, respectively. (c) is the histogram of the green square in (a). The parallel layer is 0.87nm above the OTS surface and the patch is 3.95nm above the parallel layer.

4.4.2.2 The parallel layer forms prior to the standing-up layer

The alkane molecules migrate from the main OTS pattern to the satellite patterns via vapor phase mass transport and form the parallel layers. Such process also takes place within the main pattern. Here I discover the sequence of the formation of the parallel layers and the standing-up layer by controlling the spreading temperature under the melting point of C36.

In this experiment, the C36 molecules spread over the surface containing both main OTSpd pattern and satellite OTSpd patterns at 70 °C, which is 5 ° below the melting point of C36. The result was captured with AFM in tapping mode and presented in Figure 4.12. In the topography image, the alkane drop remains intact and no liquid flowing occurs. However, both main pattern and the satellite pattern are covered with the parallel layers of C36 molecules, which appear to be higher than the OTS surface. Therefore, I conclude that the parallel layers form without the presence of the liquid alkane molecules. The parallel layers on the main OTSpd pattern forms prior to the formation of the standing-up layer.

A series of samples shows that the deposition of the C36 molecules via vapor phase transport occurred beyond 10μm which is the characterization range of the AFM and no difference of the thicknesses of the parallel layers are observed within the same sample. I believe that within the radius of 10μm, the vapor pressure of C36 at 70 °C is high enough so that the adsorption of the alkane molecules always occurs. Since the vapor pressure only depends on the intrinsic properties of the molecules under the ambient conditions, I speculate that such vapor phase transport happens on the SiO_2 surface as well. Therefore, during the spreading of alkane over the SiO_2 surface reported by Riegler[49] and Taub[51],

the long-chain alkane molecules formed the parallel layer first, and then their liquids spread afterwards.

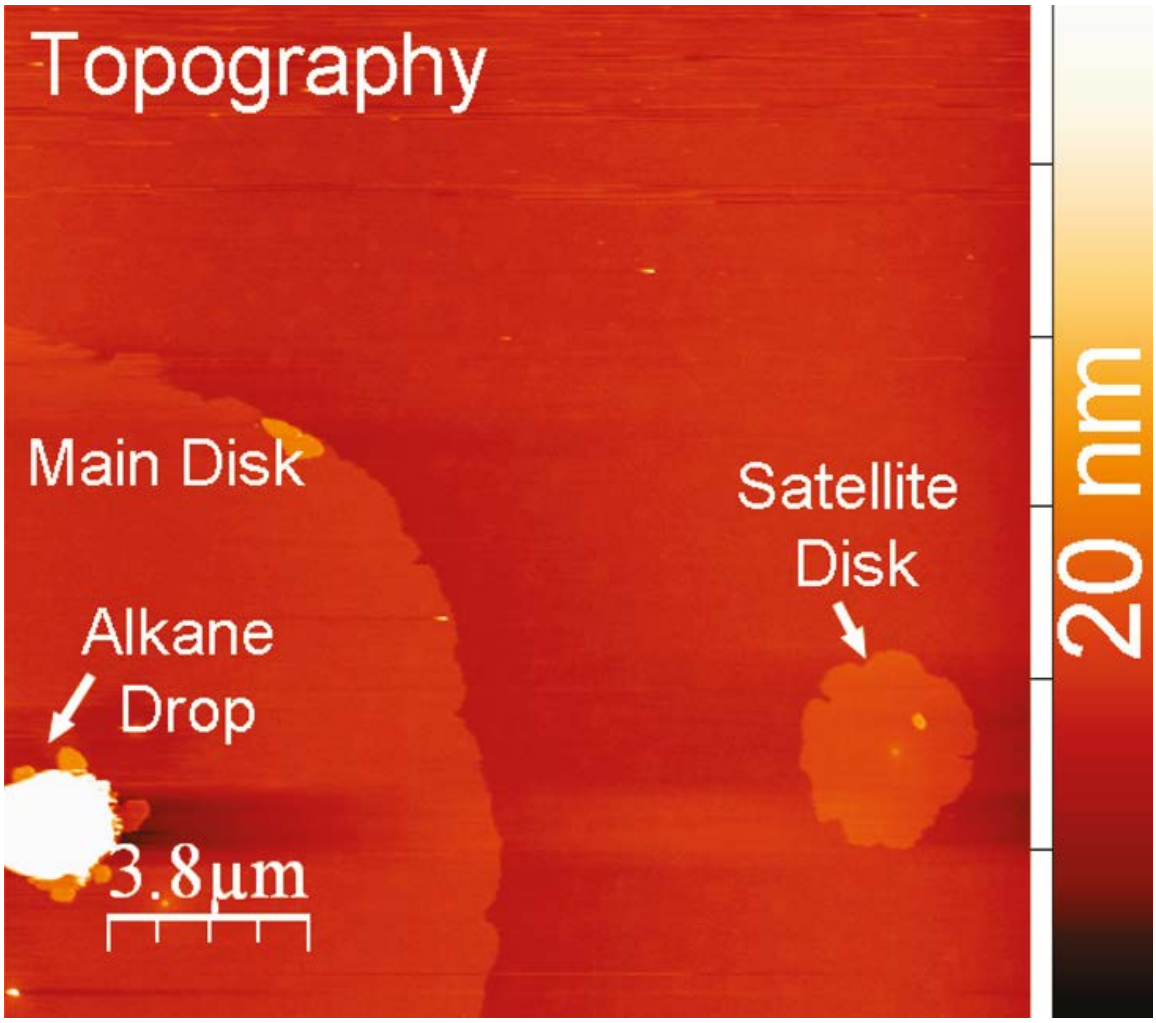

Figure 4.12. C36 molecules cover both main OTSpd pattern and the satellite pattern at the temperature of 5° below the melting point of C36.

4.4.3 Conclusions

C36 molecules spread over OTSpd surfaces through both liquid phase expansion and vapor phase transport. In this section, a big main OTSpd pattern is fabricated to serve

as the surface where both liquid expansion and vapor phase transport occur simultaneously. Satellite OTSpd patterns are also fabricated on the same surface while they are isolated from the main pattern by OTS surface. C36 can only transport to the satellite patterns through vapor phase transport. After spreading, both main pattern and satellite patterns are filled with C36 molecules. Since C36 molecules are not able to overflow the main pattern, the C36 molecules in satellite patterns must come through vapor phase transport. The effects of vapor phase transport are, therefore, extracted.

Compared with the C36 film in the main pattern, the C36 films in satellite patters are mainly composed of parallel layers. Furthermore, by controlling the spreading temperature below the melting point of C36, C36 molecules are still condensed into the satellite patterns and form parallel layers. Therefore, the effects of liquid phase expansion and vapor phase transport are distinguished for the first time. The parallel layers of C36 molecules on the high energy surface are formed by vapor phase adsorption, which proceeds the spreading of the liquid alkane.

4.5 The stability of the parallel layer

The precursor films of alkane molecules expand over the surfaces at their melting points.[13] Previously, I found the parallel layer formed at the temperature below the melting point, which brought up a question whether the alkane flowed over the parallel layer or the parallel layer moved with the liquid alkane. If the parallel layers were pinned on the solid substrate, they changed the substrate of the wetting process from the OTSpd surface to the parallel layers. In order to address this question, the stability of the parallel layer needs to be investigated. However, it is always difficult to track the motions of

molecules, especially on some featureless surface, such as SiO_2, HOPG and so forth. Here, I use the fabricated OTSpd patterns to tackle this problem. By connecting a fresh pattern with the old pattern where the alkane parallel layer has already formed, the parallel layers of alkane are allowed for further expansion. Therefore, any change of the parallel layers could be used to study the stability of the parallel layer.

4.5.1 Methods and experiments

The stability of the parallel layer was studied via a two-stage spreading method. Figure 4.13 illustrates the experimental scheme. Figure 4.13(a)-(e) are the same steps as the spreading alkane over OTSpd patterns. The alkane molecules were dip-coated on a small OTSpd pattern followed by the spreading over an enlarged OTSpd pattern. After the structures of the C36 film were characterized with AFM in tapping mode, the sample wafer was again heated to 90 °C to make the standing-up layer flow away from its original position. The features left over the parallel layer were, therefore, used as the indicator for monitoring the motion of the parallel layers. The subsequent step involved the further fabrication of a fresh OTSpd pattern enclosing to the original pattern. Making the alkane film expand again above the melting point provided the opportunity for the molecules to migrate to the newly created patterned area via both vapor condensation and liquid flow. The final structure of the precursor film was also characterized with AFM in tapping mode. The geometric properties of the OTSpd patterns and the precursor films were compared in the same scale.

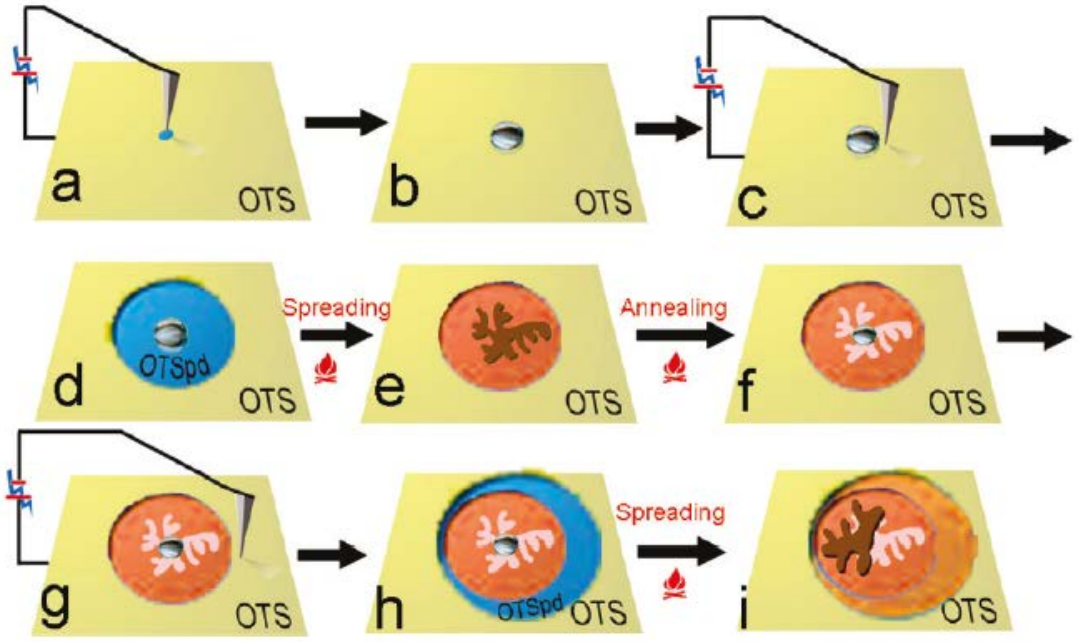

Figure 4.13. Scheme of using alkane residues as the landmark to track the movement of the parallel layer during the spreading. (a) - (e) Steps of spreading alkane over an OTSpd pattern. (f) The sample is heated again. The standing-up layer of alkane molecules flows away and leaves residues at its original position. (g) The AFM tip is moved to the position close to the OTSpd pattern. A 10V pulse is applied to fabricate a fresh OTSpd surface surrounding the original pattern. (h) The fresh OTSpd surface, in blue, surrounds the old pattern. (i) The sample is heated again at 90 °C for 25 seconds. Alkane molecules cover the newly fabricated OTSpd surface (in tangerine). The residues are used as the landmark to track the movement of the parallel layer.

4.5.2 Results and discussion

4.5.2.1 Residue layer forms after the perpendicular layer flows away

A representative precursor film of C36 over OTSpd pattern is shown in Figure 4.14. Similar to other C36 precursor films, this film also follows the bilayer model in that a 44.2Å thick standing-up layer sits on the parallel layers. After annealing, the topography image and the phase image of the same region are shown in Figure 4.15(a) and (b), respectively.

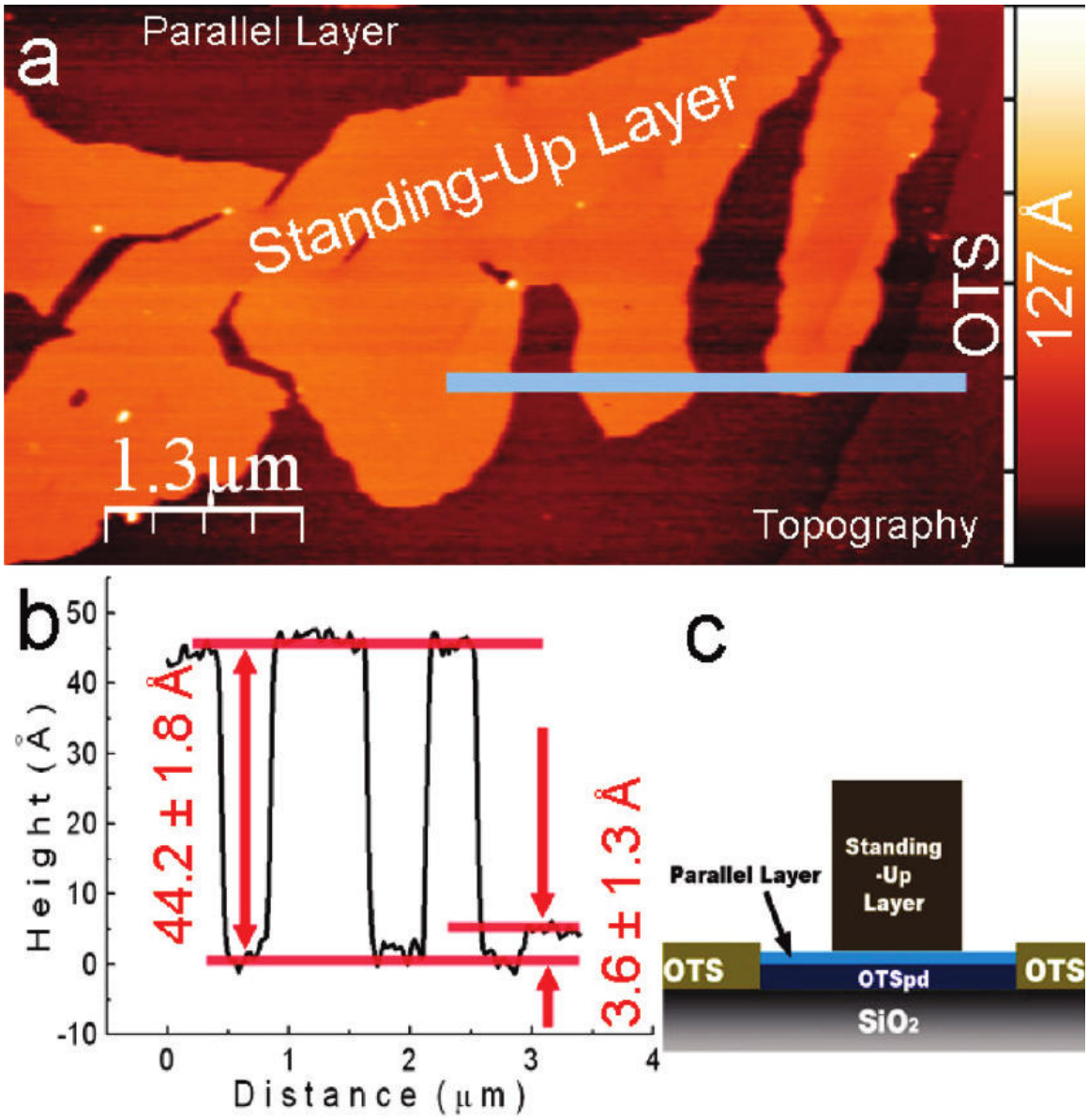

Figure 4.14. A C36 standing-up layer on an OTSpd pattern. (a) The topography image of the C36 film captured in tapping mode. (b) Height profile along the blue line in the topography image. The standing-up layer is 4.42±0.18 nm thick, and the parallel layer is 0.36±0.13 nm below the OTS surface. (c) Structural model of the C36 film over OTSpd pattern.

The C36 molecules in the standing-up layer flowed away during the annealing process and left residues on the parallel layers as the green species indicated in Figure 4.15(a). Compared with Figure 4.14(a), I find that the shape of the residue layer in Figure 4.15(a) is similar to that of the standing-up layer before annealing. However, the thickness of the residue layer is not even. In the height profile (Figure 4.15(c)) of the residues, the largest height contrast is 0.42 nm, which is about the thickness of a C36 lying down monolayer. In principle, AFM converts the interactions between its probe and the detected surface to the height information. However, if the surface material is not dense enough, the AFM tip may also penetrate the surface. Consequently, the apparent height given by the AFM is smaller than the actual value. Here, because the residual molecules fail to support the tip, some of the measured heights appear to be smaller than the thickness of the C36 monolayer, 0.42 nm. The corresponding phase image in Figure 4.15(b) also confirms the same information. The phase image is made of two colored components, the yellow region is the patterned area and the black region is the OTS surface. A slightly lighter yellow area over the OTSpd pattern matches the shape of the residue layer in the topography image, while its phase signal is just 22±9 mV higher than that of the rest of the OTSpd pattern. I speculate such small difference of the phase signals is caused by the roughness of the loosely packed molecules.

In sum, the residues are characterized. They will be used as marks on the previously featureless surface to track the motion the parallel layers.

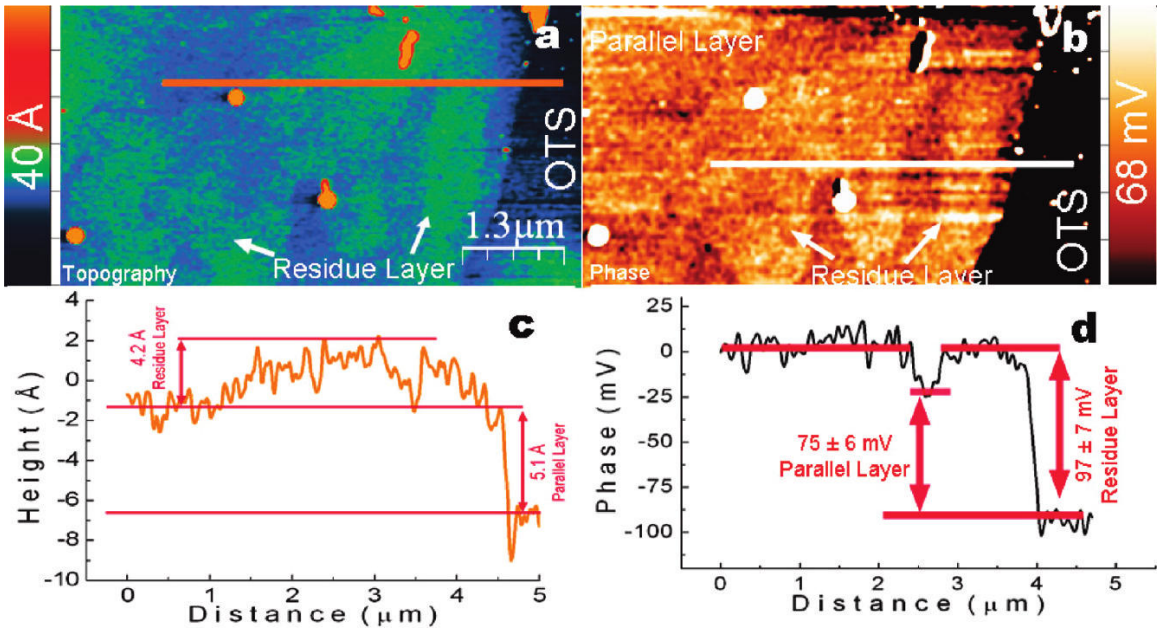

Figure 4.15. Residues of the standing-up layer. (a) Topography image; (b) Phase image. Similar phase signals of residues and parallel layer indicate the residues are the alkane molecules laying parallel to the surface. (c) Height profile of the orange line in the topography image. (d) Phase signals along the white line in the phase image.

4.5.2.2 Use the residue layer to track the movement of the parallel layers

Previously, I found the alkane liquid flowed over its parallel layers during the spreading. Although Taub observed the existence of the parallel layer at the temperature above the melting point of C32,[51, 52] no evidence showed whether the molecules were pinned on the SiO_2 surface or still had certain mobility in X-Y plane. In order to track the movement of the parallel layers, a landmark is required to indicate the original position and the current position after the expansion of the parallel layers. The residues of the standing-up layer possess an integrated shape and the same molecular orientation as the parallel layers. If the parallel layers move during the spreading, either the shape or the position of the residue layer will change. Here, I use the residue layer and the

OTSpd/OTS boundary as reference to investigate the movement of the parallel layers during the spreading.

Figure 4.16(a1), (b1) and (c1) are the C36 layers before annealing, after annealing and after re-spreading, respectively. All the images are rendered in the same scale. As described previously, the shape of the residue layer is the same as the shape of the standing-up layer before annealing. By stacking the image Figure 4.16(b1) on top of Figure 4.16(a1), I find both boundaries of OTSpd/OTS and the outlines of the alkane layers overlaid, indicating the parallel layers did not move during the annealing.

By following the scheme in Figure 4.13(g)-(i), a fresh fabricated OTSpd pattern surrounded the old OTSpd pattern, and the C36 molecules were re-spread over the pattern. The result, Figure 4.16(c1), shows a new rim of OTSpd pattern covered with C36 molecules. In addition, the shape and the position of the residue layer still keep the same.

Since the residue layer did not move during the annealing and re-spreading, I conclude the parallel layer is stable thermodynamically and the alkane liquids spread over their parallel layers instead of spreading with their parallel layers.

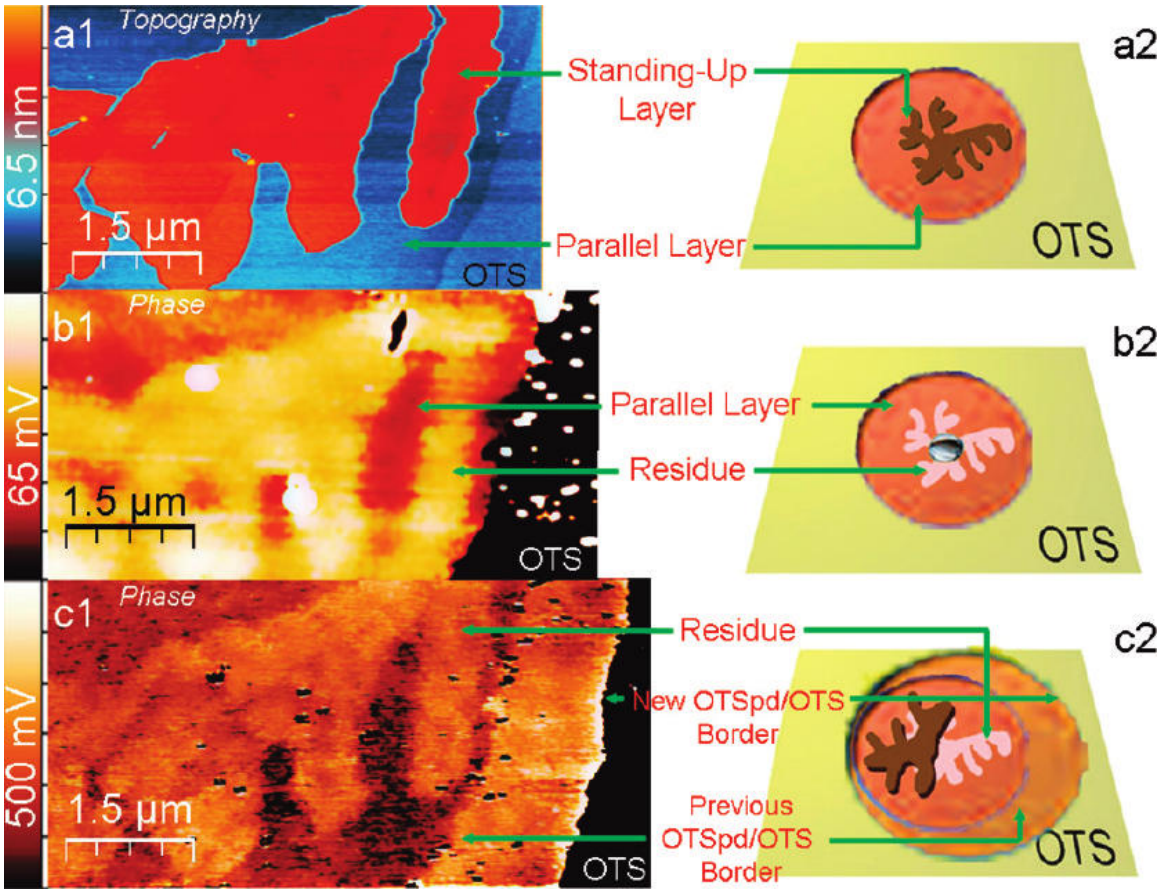

Figure 4.16. Comparison of the alkane layers. (a1) Topography image of the standing-up layer. (b1) Phase image of the residue layer. (c1) Phase image after re-spreading. (a2), (b2) and (c2) are the experiment steps illustrated in Figure 4.13

4.5.2.3 The source of the residue layer

The average thickness of a residue layer of C36 is less than 0.42 nm and the layer is the same shape as the standing-up layer. Generally speaking, there are two possible sources of the residual molecules, the standing-up layer and the parallel layer. On one hand, the residual molecules are probably from the standing-up layer and fall down during the annealing (Figure 4.17(2b)). On the other hand, it is also possible that a monolayer of parallel molecules flows away with the standing-up layer as illustrated in

Figure 4.17(1b). As a result, the thickness of the parallel layer should decrease. In this experiment, first of all, the parallel layer has been confirmed to be stable. Also, by comparing the topography images before and after annealing, I find the thickness of the parallel layer increases by 0.87±0.15 nm. Therefore, the second scenario does not hold. The formation of the residue layer must be caused by the molecules from the standing-up layer.

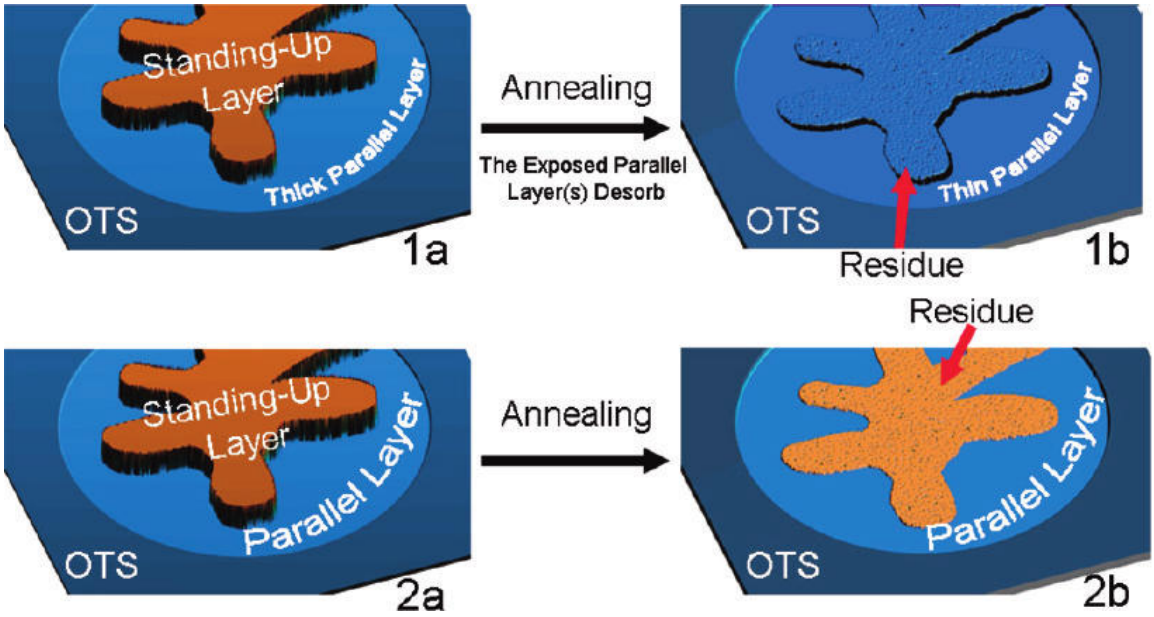

Figure 4.17. Scheme of the formation mechanism of the residue layer. (1a) and (2a) are the illustration of the standing-up layer. (1b) The residue layer forms because the molecules in the parallel layers flow away. (2b) The residue layer comes from the molecules of the standing-up layer.

Previously, Taub found the evidence of the domain structures within the parallel layer.[51] The alkane molecules shared the same azimuthal orientation within the same domain while the orientations varied from domains. During the cooling process, the

standing-up molecules were pinned to the domains that determine the shape of the standing-up layer. In this section, it could also be the reason that the residual molecules had higher affinity to the domains of the parallel layers, and the shape of the residue layer was determined by the domains as well.

4.5.3 Conclusions

The parallel layers of C36 molecules form prior to the standing-up layers during the spreading. Their stabilities directly impact the spreading process. If the parallel layers don't move with the standing-up layers, they change the solid/vapor interface to the parallel layer/vapor interface. In this section, a residue layer of C36 molecules laying parallel to the surface is found after the molecules of the standing-up layer flow away. By using the residue layer as a reference, the parallel layer is found remaining stationary during the spreading. These results indicate that during the spreading, the liquid molecules do not directly interact with the OTSpd surface, instead, they are directly influenced by the same C36 molecules in the parallel layers. Consequently, the surface properties of the parallel layers control the liquid behavior during the spreading.

4.6 Frictional properties of the n-Hexatriacontane self-assembly membrane

The frictional properties of a SAM are important for its applications in MEMS and lubrication. Systematic studies of alkanethiol SAM surface[124] and silane SAM surface[125] showed the dependence of the tribological properties on the structures of the SAMs.[118, 126] Unlike the uniformly and densely packed alkanethiol SAMs and silane SAMs, the standing-up layer of a C36 precursor film contains domains that have different

thicknesses. Molecules in those domains have different tilting angles, and the densities of the exposed methyl groups are different. The frictional study of the alkane standing-up layers needs to correlate the frictional properties with the orientations of the molecules. In this section, the structures of the C36 standing-up layers are carefully characterized, and the frictional properties of the C36 standing-up layer that molecules tilt 40° to the surface norm are studied with AFM.

4.6.1 Methods and experiments

The preparation and characterization of the C36 precursor film followed the procedure demonstrated in Figure 4.1 and will not be further described here.

The calibration of the force constants and torsional force constants of the AFM tips followed Sader's method.[127-129] First, the frequency response curve was measured to obtain the quality factor of the cantilever, Q and the resonant frequency of the cantilever, ω, in the air. The spring constant of the cantilever was calculated by substituting the quality factor and the geometric parameters of the cantilever to the equation 4.1:[129]

$$k_z = 0.1906\rho b^2 L Q \Gamma_i \omega^2 \qquad (4.1)$$

where L and b are the length and the width of the tip; the imagary part of the hydrodynamic function Γ_i depends on the resonant frequency of the tip in the experimental environment and could be found in Sader's literature;[129] the density of the air is 1.18 kg·m^{-3}. The torsional spring constant is a function of the normal force constant and could be found by following the equation 4.2:[127]

$$k_\phi = k_z \frac{2L^2}{3(1+\nu)} \qquad (4.2)$$

where k_z is the normal force constant obtained above and υ is the Poisson ratio of the material of the cantilever which is 0.28 for Si(100) in this dissertation.[120]

A typical CSC-17/no Al cantilever used in this dissertation has its length equal to 425±5μm, width equal to 50±3 μm, resonant frequency equal to 12±2 kHz, and quality factor equal to 50. By applying these parameters to the equations above, the spring constant of this cantilever is found to be 0.136±0.012 N/m, and the torsion constant is $2.26 \cdot 10^{-8} \pm 0.14$ N·m.

4.6.2 Results and discussion

4.6.2.1 Stability of the standing-up layer of C36 precursor film

As discussed previously, a C36 precursor film over an OTSpd surface is composed of several parallel layers and a standing-up layer where molecules tilt 0°, 29°, 40° or 48° to the surface norm. Figure 4.18(a) and (b) are the topography image and the phase image of a C36 precursor film. By correlating the height profile along the black line in the topography image and the phase signals along the blue line in the phase image, a 3.9±0.2 nm thick standing-up layer and two parallel layers of C36 molecules are found in the film. Since the full length of a C36 molecule is 5.02 nm, the molecules in standing-up layer tilt 40° to the surface norm.

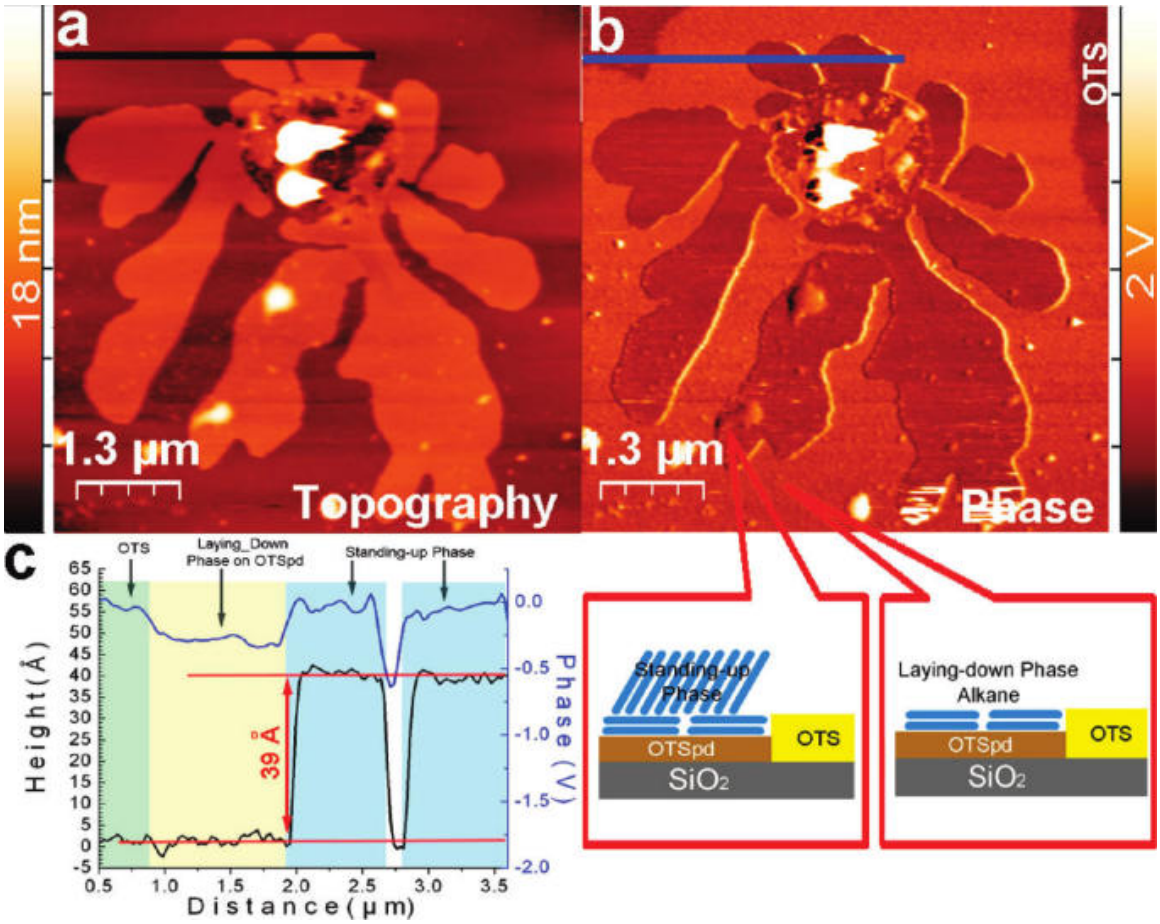

Figure 4.18. C36 precursor film over an OTSpd pattern. (a) Topography image of a C36 precursor film. (b) Phase image of the corresponding area. The call-out boxes are the models of the standing-up layer and the parallel layers, respectively. (c) The height profile along the black line in the topography image and the phase signals along the blue line in the phase image, respectively.

In order to characterize the frictional properties of the C36 film, the same region shown in Figure 4.18 was scanned by MikroMasch CSC-17 tip in contact mode under various loading forces, as shown in Figure 4.19. Figure 4.19(a) is the topography image captured in contact mode. Some parts of the film in yellow have integrated shapes. Others in brown are penetrated by the AFM tip under high pressure. The tapping mode

topography image, Figure 4.19(b), shows the shape of the C36 film after the contact mode scanning. The numbers between the topography images are the loading forces applied between the green lines. The friction of the C36 standing-up layer and the OTS surface are plotted in Figure 4.20. Although the standing-up layer and the OTS surface are both terminated with methyl groups, their coefficients of friction (COF) are different. The linear regression fitting of the friction vs. loading-force curves indicates that the COF of the OTS surface is 0.064±0.002, which agrees with the reported value.[120] The COF of the C36 standing-up layer with the loading force below 28 nN is 0.089±0.003, which is higher than that of the OTS surface. I speculate the increase of the COF is due to the lack of anchoring functional groups. During the contact mode scan, the tip picked up the alkane molecules which were not bound with the solid substrate. Those molecules increased the contact area between the tip and the surface, and also interacted with the C36 molecules in the film. As a result, the interaction between the tip and the C36 standing-up layer increases.

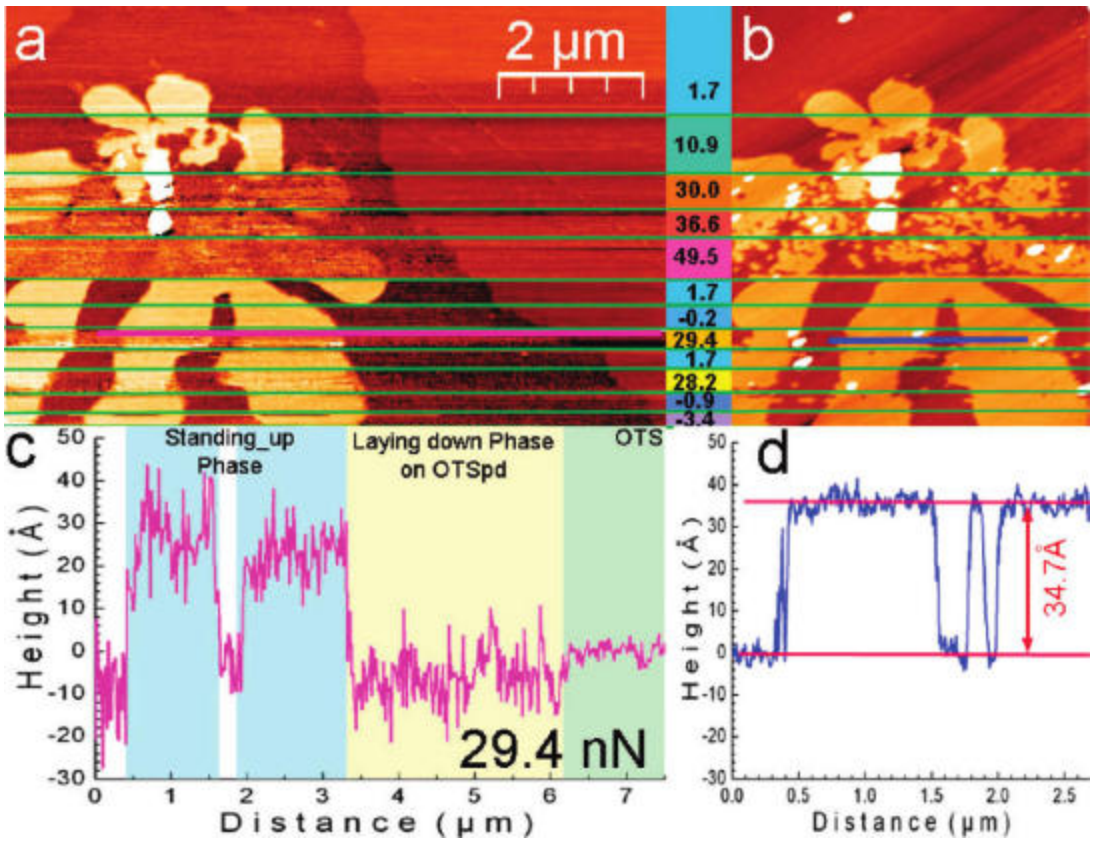

Figure 4.19. Responses of the C36 standing-up layer to various loading forces. (a) Topography image of the standing-up layer under different loading forces in contact mode. (b) Topography image of the standing-up layer after the wiping in tapping mode. (c) Height profile along the pink line in the topography image of contact mode. Under 29.4nN loading force, the apparent height in contact mode decreases to 2.7±0.5 nm, and the standard deviation of the height increases greatly. (d) Height profile along the blue line in the topography image of tapping mode. The layer recovered and the thickness is 3.47±0.11 nm.

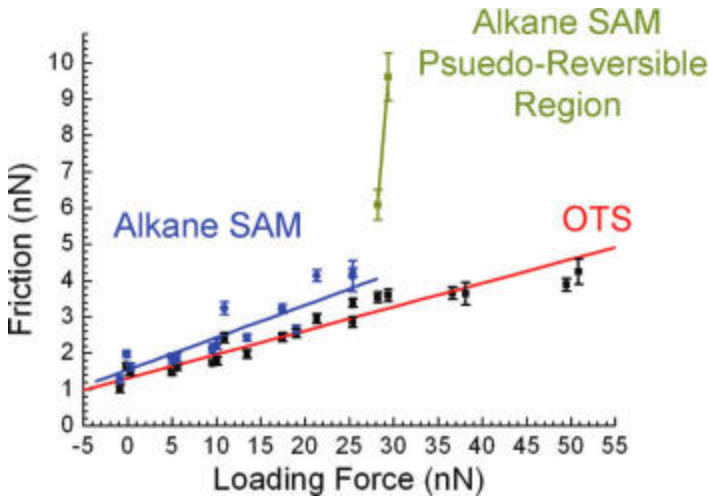

Figure 4.20. Plot of friction vs. loading force of the alkane standing-up layer and the OTS surface.

According to the COFs of the standing-up layer, the loading force could be divided into three regions, below 28 nN, 28 nN to 30 nN and beyond 30 nN. Under 28 nN loading force, the standing-up layer retains its own shape and thickness which is 3.9±0.2 nm. As the loading force is raised between 28 nN and 30 nN, the frictional behavior changes. The COF jumps from 0.089 to 3.0. In the contact mode topography image, Figure 4.19(a), although the shape of the layer persists, the roughness of the film increases. The height profile in Figure 4.19(c) shows the thickness varies from 1.3 nm to 3.9 nm, and the average value is about 2.7±0.5 nm. The standing-up layer of the same region was further characterized by tapping mode as shown in Figure 4.19(b). Since the tapping mode is a nondestructive imaging method, the topography image reveals the actual morphology of the C36 film after the wiping in contact mode. During 28 nN to 30 nN loading force, the shape of the fractal remains its original shape, while the thickness is reduced from 3.9±0.2 nm to 3.47±0.11 nm as indicated in Figure 4.19(d). The surface of the C36 layer

appears to be smooth, indicating the molecules recovered after the tip penetrated into the layer in contact mode. Therefore I define such loading force regions as pseudo-penetration region. Even though the alkane standing-up layer appears to be the same shape before the wiping, the orientation of the molecules changes.

When the loading force rises beyond 30 nN, the height of the alkane layer measured by the contact mode is further reduced. The color of the standing-up layer during this loading force region is just slightly higher than that of the parallel layer, indicating that the tip completely penetrated into the standing-up layer. Meanwhile, the alkane layer turned into small patches in the topography image of tapping mode after the film was shaved by the tip. The shaved-off molecules were dragged to the edge of the scanning zone which is not shown here.

The COF of the parallel layer is 0.159±0.012 which is higher than those of the OTS surface and the surface of the standing-up layer. By comparing the original topography image (Figure 4.18(a)) and the image captured under the pressures(Figure 4.19(a)), I find the AFM tip always penetrated the parallel layer. Due to the resistance of the alkane molecules in the parallel layers and higher affinity of the OTSpd surface to the tip, the COF of the parallel layer increases as a result of both influences.

Finally, the critical penetration pressure of the C36 standing-up layer is calculated with Hertzian contact model. The Hertzian contact model describes the relationship of deformation of the contacted solids and the contact area as shown the equation 4.3:[119]

$$A^{3/2} = \frac{3}{4}\left(\frac{1-\nu_1^2}{E_1} + \frac{1-\nu_2^2}{E_2}\right)\pi^{3/2}RL \qquad (4.3)$$

where R is the tip radius, L is the loading force, E_1 and E_2 are the Young's moduli of the tip and the alkane layer, and the υ_1 and υ_2 are the Poisson's ratios of the tip and the

alkane layer, respectively. As calibrated with double-stranded DNAs whose diameters are 2.2 nm, the radius of the tip was found to be 4.6 nm.[130] The Young's modulus and Poisson's ratio of the silicon tip is 61GPa and 0.27, respectively.[131] The values of the parameters for C36 layer, however, were unknown. Nevertheless, if I used the values of octadecanethiol monolayer (1GPa and 0.44, respectively),[132, 133] the contact area comes out to be 58nm^2 at 28nN loading force and 61nm^2 at 30nN loading force. Therefore, the critical pressure for the pseudo penetration is 0.48 GPa, and the critical pressure for the irreversibly destructive penetration is 0.49 GPa. Beyond 0.49 GPa, the alkane layer was shaved into small patches. In comparison, the critical penetration pressure of an octadecanethiol SAM is 2.3 GPa. I speculate that the thiol-silicon bond inhibits the movement of the octadecanethiol molecules in the X-Y plane. However, C36 molecules are pushed away when the tip penetrates the layer. Instead of breaking a thiol-silicon bond in the octadecanethiol SAM, the C36 molecules just need to overcome the van der Waals interaction between the neighboring molecules. Consequently, the critical penetration pressure of the alkane film is much smaller than that of an alkanethiol SAM.

4.6.2.2 Friction is affected by the molecular tilting angles

The friction over the standing-up layers that have different heights are found different under the same loading force. Figure 4.21 was captured under a minimal loading force, 5nN, under which the shapes and the heights of the C36 standing-up layer will not change. There are two domains found in Figure 4.21(a). One is 3.9±0.2 nm thick and the other is 3.4±0.2 nm thick. The corresponding frictional measurement shows the friction is 1.82±0.06 and 1.37±0.04nN, respectively. Since the friction was measured using the

same tip, under the same loading force and in the same scanning line, the observed frictional difference reflects the real difference of the surface tribological properties.

In this sample, the friction follows the single-asperity contact model[134-136] and the loading force is small. Therefore, the tip's disturbance to the alkane lattice is insignificant. The difference of the friction is impacted by the number of the alkane molecules under the tip. Previously, I have calculated that the 3.4±0.2 nm thick domain is 13% less dense than the 3.9±0.2 nm thick domain. Therefore, the 3.4±0.2 nm thick domain has 13% less interaction with the tip than that of the 3.9±0.2 nm thick domain. In our measurement, the friction of the 3.9±0.2 nm thick domain is 33% higher than that of the 3.4±0.2 nm thick domain. Beside the uncertainty of the measurements, I believe other possible factors, such as adhesion, the lattice structure and the stiffness of the alkane film, may also lead to the lower friction of the lower domain. Those factors will be investigated in the future.

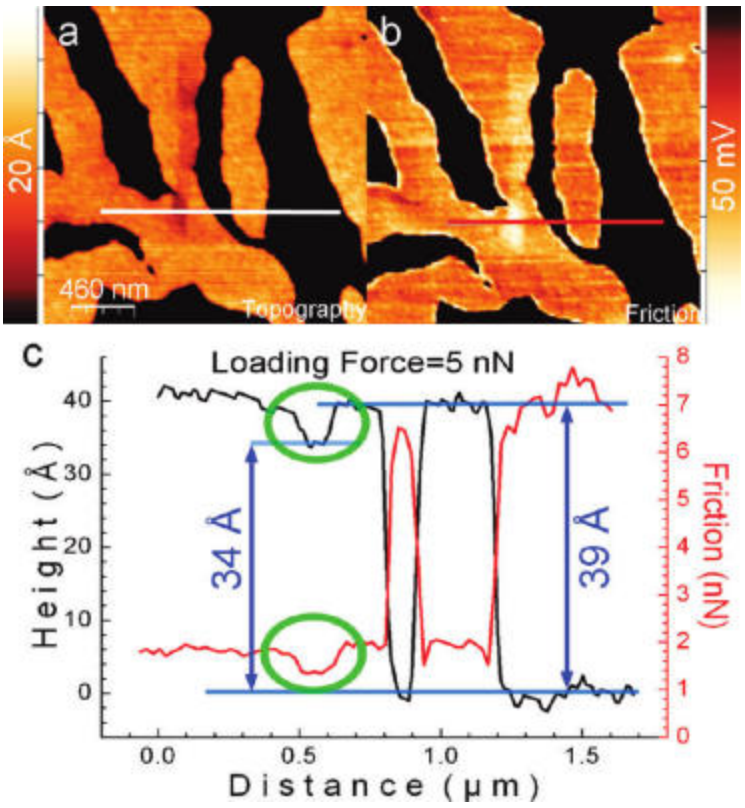

Figure 4.21. Friction is impacted by the molecular tilting angle. (a) Topography image of a standing-up layer which contains two domains under 5 nN loading force in contact mode. (b) the corresponding phase image. (c) height profile along the white line in the topography image and the corresponding phase signals of the same area. There are two domains. The 3.4±0.2 nm thick domain has 1.37±0.04nN friction response and the 3.9±0.2 nm thick domain has 1.82±0.06 friction response.

4.6.3 Conclusions

The mechanical properties of the C36 film are important for the applications in MEMS. In this section, the mechanical properties of a C36 standing-up layer of which the molecules tilt 40° to the surface norm are systematically studied. At the loading force 0-28 nN, the COF is 0.089 which is higher than the OTS surface. In the region of 28 nN to

30 nN, the standing-up layer is partially penetrated by the AFM tip and recovers after scanning. When the loading force is beyond 30 nN that is equivalent to 0.49 GPa in the experiment, the alkane film is destroyed. Furthermore, the standing-up layer with smaller tilting angle has higher COF due to its higher molecular density.

4.7 Summary of this chapter

The precursor film of n-hexatriacontane over OTSpd patterned surfaces follows the bilayer model in which a standing-up monolayer of the C36 molecules sits on several parallel layers. The number of the parallel layer(s) varies from one to five, while the molecules in the standing-up layer tilt 0°, 29°, 40° or 48° to the surface norm. Due to different tilting angles, domains are found in the standing-up layer. Within a domain, molecules tilt at the same angle, while molecules may be oriented differently between the domains. By applying an external force on the domain-structured fractal, the molecules in the higher domain are pushed down. Such changes in height also confirms the domain structure of the standing-up layer.

The formations of the parallel layers and the standing-up layer follow different mechanisms. The parallel layers form through vapor-phase mass transport, while the standing-up layer is formed by diffusion limited aggregation. During the spreading, the parallel layers form prior to the liquid flow and the seaweed-shaped standing-up layer may be impacted by the parallel layers.

On the aspect of stabilities, the parallel layer(s) is more stable thermodynamically than the standing-up layer, while the standing-up layer is able to withstand more loading force. A residue layer of C36 molecules is found after the molecules of the standing-up

layer flow away. By using the residue layer as a landmark, the parallel layer is found not spreading with the standing-up layer. A C36 standing-up layer whose molecules tilt 40° to the surface norm could bear 0.49 GPa pressure before being permanently damaged. Below 28 nN loading force, the COF of the standing-up layer is 0.089, which is higher than the OTS surface. During the region of 28 nN and 30 nN, the standing-up layer is partially penetrated by the AFM tip and recovered after scanning.

Chapter Five

STUDY OF THE SPREADING OF IONIC LIQUIDS OVER OCTADECYLTRICHLOROSILANE PARTIALLY DEGRADED PATTERNS

5.1 Introduction

Ionic liquids (ILs) are known as organic salts that have extremely low vapor pressures. They are widely used as lubricants,[137-139] extracting agents[140-142] and electrolytes in lithium ion batteries.[143-145] Studies revealed that ILs over a solid interface formed layered structures,[15, 60-62] which improved the interfacial properties.[61, 146-148] Earlier studies on the interfacial structures of the IL films by AFM showed the molecules adsorbed on gold surface and HOPG formed terraced layers whose thicknesses varied by several nanometers depending on the identity of the anion.[61, 62] X-ray diffraction and X-ray reflectivity results implied that at the interfacial layer, the long chain n-alkyl substituted imidazolium cations normally formed dimers where the alkyl side chains of two imidazolium aligned together.[72] Nevertheless, the formation mechanism and the molecular structure of the interfacial layers are still unclear. Further understanding the interfacial layer is the key to improving the application of the ILs.

1-butyl-3-methylimidazolium ([Bmim]) ILs are wildly used and are the most studied among all ILs. In bulk, the [Bmim] cation has a characteristic L shape where the butyl group does not share the same plane with the imidazolium ring.[149] However, at interfaces, [Bmim] cations show different conformations. Particularly, at the graphene/IL interface, the imidazolium ring and its butyl group both lie parallel to the surface plane.[63,

[64] When the interfacial film becomes thicker, the butyl groups at the IL/vapor interface no longer lie parallel to the surface; instead, the butyl group tilts 20°-54° to the surface norm.[65-67] Meanwhile, Seddon found that at the IL/vapor interface, the surface norm passes through the N-N axis on the imidazolium ring.[69] Therefore, the imidazolium ring also stands up on the surface. Further observation made by Deutsch et al. indicated the [Bmim] cations were aligned alternately at the surface.[71, 150, 151] No matter whether the imidazolium ring pointed to the air or to the solid substrate, the methyl groups were confirmed to be exposed to the air.[71]

In this chapter, I use OTSpd patterns to study the interfacial layers of 1-butyl-3-methylimidazolium chloride ([Bmim][Cl]). When the [Bmim][Cl] ion pairs spread over an OTSpd surface, the orientations of the cations are distinguished by the difference of the phase signals between the IL films and the OTS surface. Furthermore, the vapor phase transport of the [Bmim][Cl] ion pairs is also investigated. Although the vapor pressure of [Bmim][Cl] is normally considered negligible, molecules deposited over an OTS surface still change the friction of the surface. By comparing the COF of a fresh OTS surface and the vapor deposited OTS surface, the vapor phase transport of the [Bmim][Cl] ion pairs is confirmed. Finally, the orientation of the [Bmim][Cl] ion pairs impacted by the surface dipoles is explored. By coating the OTSpd surface with Zn^{2+} ions, the dipole of the solid surface is changed. IL molecules deposited on the OTSpd surface and the Zn^{2+} coated surface have different phase signals, indicating [Bmim][Cl] ion pairs have different orientations on different surfaces.

5.2 Materials and instruments

Silicon (100) wafers, nitrogen doped with 13 ohm·cm resistivity, were purchased from James River Semiconductors. Octadecyltrichlorosilane (OTS, 97%) was from Gelest. n-Hexatriacontane (C36, >99%) was purchased from Sigma. Zinc chloride (>98+%) was from Alfa Aesar. 1-Butyl-3-methylimidazolium chloride ([Bmim][Cl], >98%) was purchased from Aldrich. 1-Butyl-3-methylimidazolium bis(trifluoromethylsulfonyl)imide ([Bmim][Tf_2N]) was provided by Dr. De-en from Oak Ridge National Lab. All the chemicals were used without further purification.

The octadecyltrichlorosilane partially degraded (OTSpd) patterns were fabricated with an Agilent PicoPlus Atomic Force Microscopy (AFM) which was equipped with an environmental chamber. All the AFM tips were purchased from MikroMasch. The CSC-17/Ti-Pt tips used to fabricate the patterns were coated with Ti-Pt and generally had a force constant of 0.18±0.10 N/m. The CSC-17/No Al tips used for the frictional measurements were made of silicon and also had average force constant of 0.18±0.10 N/m. The tips used to characterize the IL films in tapping mode were NSC-14 whose typical spring constant was 5±2 N/m. All the AFM images were processed with WSxM.[121]

5.3 The structure of the [Bmim][Cl] film over OTSpd patterned surface

5.3.1 Methods and experiments

The spreading method follows the same procedure of the spreading of C36 described in the last chapter, as shown in Figure 5.1. First, the [Bmim][Cl] was dip-coated on an OTSpd pattern. A bigger OTSpd pattern was then fabricated enclosing the

IL drop. Subsequently, the sample wafer was heated on a hotplate at 100 °C for 5 min. Finally, IL film over OTSpd surface was characterized with AFM in tapping mode.

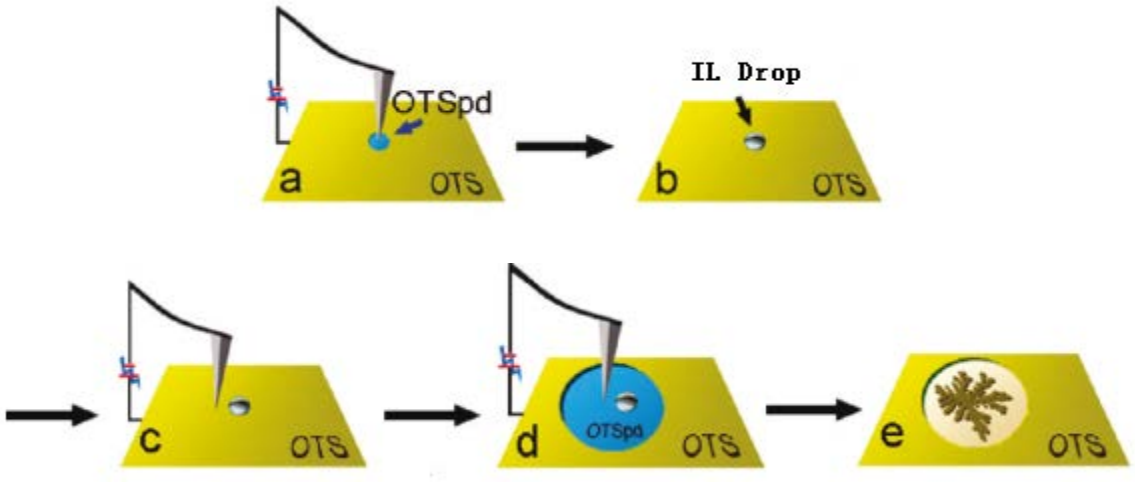

Figure 5.1. Scheme of [Bmim][Cl] spreading over an OTSpd patterned surface. (a) An OTSpd pattern whose diameter was 1-2 μm was fabricated on an OTS coated silicon wafer through local probe oxidation lithography. (b) The ionic liquid molecules, [Bmim][Cl], were dip-coated on the OTSpd pattern. (c) The AFM tip was moved to the place close to the IL drop and conducted a 10 V pulse for 20 seconds. (d) The newly fabricated OTSpd pattern enclosed the IL source drop. (e) The sample was heated on a hotplate at 100 °C for 5 minutes to let the ionic liquid molecules spread out. The surface was characterized with AFM in tapping mode.

5.3.2 Results and discussion

5.3.2.1. The structure of the [Bmim][Cl] film

Figure 5.2 shows a typical [Bmim][Cl] film over OTSpd surface. The [Bmim][Cl] ion pairs fill the OTSpd pattern and reveal a positive height contrast to the OTS surface. The blue square in the topography image, Figure 5.2(a), indicates the intersection of the

OTSpd pattern and the OTS surface. The patterned area is 1.02±0.06 nm higher, according to the histogram shown in Figure 5.2(d). Since the average depth of an OTSpd pattern is 1.02±0.07 nm, the thickness of this IL film is 2.04±0.10 nm. The phase signals of the patterned area in Figure 5.2(b) show darker color than those of the OTS surface, indicating the IL film isn't terminated with methyl groups. There are three interfacial orientations of [Bmim] cations reported previously. One of the orientations requires the cation standing up and pointing the methyl group to the air.[68, 71] Such orientation does not match the observation of the [Bmim][Cl] layers over the OTSpd pattern. The imidazolium ring of the other two orientations lies parallel to the surface, as shown in Figure 5.3. Although the butyl group lies parallel to the surface in one orientation and tilts at a certain angle in the other orientation, neither of the orientation will result in a surface whose phase signals in AFM images are the same as the OTS surface. Therefore, I can only speculate, on the OTSpd pattern, the imidazolium ring of the [Bmim] cation lies parallel to the surface, denoted as parallel layers.

Upon the [Bmim][Cl] parallel layers, a small round patch and a big L-shaped patch are observed in Figure 5.2(a). Both patches have the similar structure that hemispherical drops of IL molecules in a bright color sit on a flat thin film in a light brown color. The histogram of the area in the green square in Figure 5.2(a) shows the thickness of the film is 3.9±0.8 nm. The corresponding phase image shows that the phase signals of the thin film are the same as the signals of OTS surface, indicating the methyl groups are exposed uppermost for the IL film. According to the molecular formula of [Bmim] cation, there are two methyl groups that one is from the 3-methyl group and the other is from the 1-butyl group. Based on X-ray scattering[73] and X-ray reflectivity results,[72] 1-alkyl-3-

methylimidazolium cations were found aligned alternately in the film at the interfaces (Figure 5.4). Law et al. also confirmed the dimer model of the methylimidazolium film at surfaces by using direct recoil spectrometry.[68] He specifically stated that at the interface of the dimer layer, the imidazolium rings were rotated and the methyl groups were exposed uppermost.[68] Therefore, I speculate that the IL molecules in the patches in Figure 5.2 also aligned alternately and expose their methyl group to the top, denoted as standing-up layer.

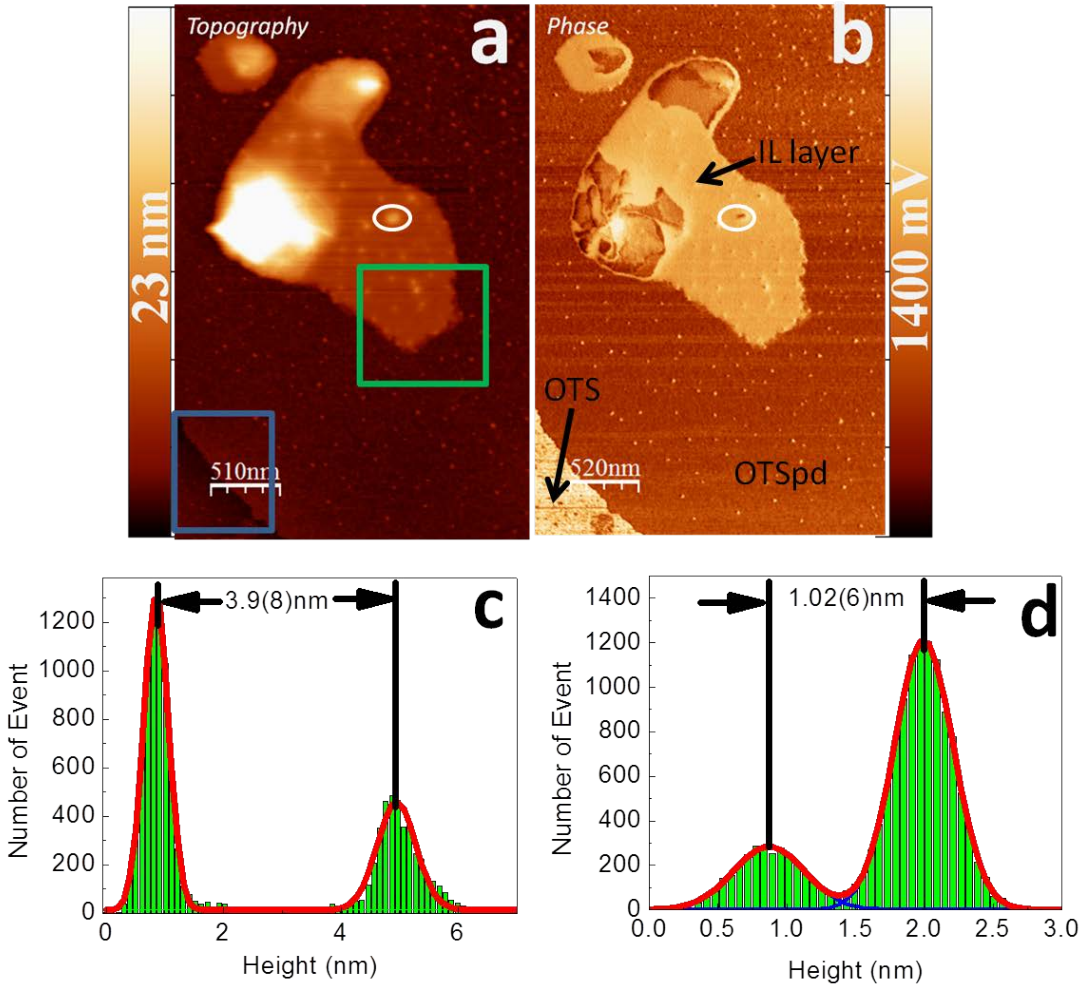

Figure 5.2. [Bmim][Cl] film over OTSpd surface. (a) Topography image of typical [Bmim][Cl] film over OTSpd surface. (b) The corresponding phase image. The IL thin

film shows the same phase signal as the OTS surface. (c) Histogram of the area highlighted in green square in the topography image. The IL thin film is 3.9±0.8 nm higher than the parallel layers. (d) Histogram of the blue square in the topography image where the OTSpd patterned area is 1.02±0.06 nm above the OTS surface. Since the depth of the OTSpd pattern is 1.02±0.07 nm, the thickness of the parallel layers is 2.04±0.10 nm.

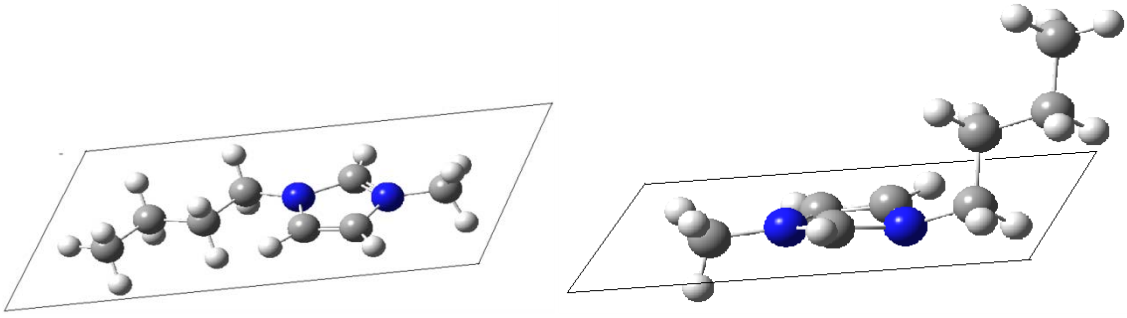

(a) (b)

Figure 5.3. Illustration of the [Bmim] cation laying parallel to the surface. (a) Both butyl group and imidazolium group are parallel to the surface. (b) The imidazolium ring lays parallel to the surface, while the butyl group tilt 20°-54° to the surface norm.

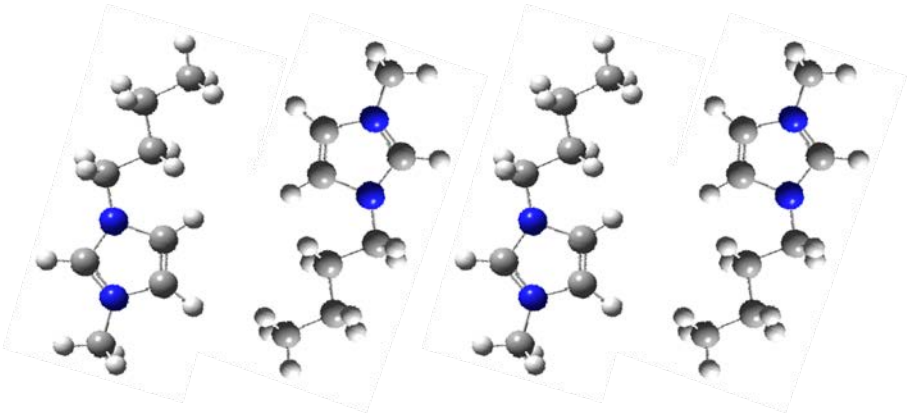

Figure 5.4. Illustration of the structure of the thin film of [Bmim] cation dimers on a solid substrate. Methyl groups on the top of the film point to the air.

In addition to the parallel layer and the standing-up layer, small dots are also observed over the OTSpd pattern. [Bmim] is composed of a charged imidazolium ring and a hydrophobic butyl tail. Such structure makes [Bmim] cations easy to aggregate and form small droplets to reach the hydrostatic equilibrium.[4] Particularly for the imidazolium ionic liquids, the aggregated molecules prefer associating their alkyl groups and expose imidazolium cations outside. Here, a small dot is highlighted in a white circle in the both topography image and phase image in Figure 5.2. The phase signals of the top of this dot are similar to that of the IL parallel layers, suggesting the exposure of the imidazolium groups. Other smaller dots revealing bright color in phase image may be caused by the surface roughness.

In summary, I find the precursor film of [Bmim][Cl] over a OTSpd pattern is composed of two kinds of layers. At the bottom of the OTSpd pattern, [Bmim][Cl] ion pairs lay their imidazolium groups parallel to the surface, denoted as parallel layers. On the top of the parallel layers, [Bmim][Cl] dimers are aligned with their alkyl chains and form a 4nm thick film where the dimers stand up and tilt to the surface norm, denoted as standing-up layer.

5.3.2.2. The residues of [Bmim][Cl] were left over after the thin film flowed away

When the sample was heated again, the IL film flowed away and left residues behind. Figure 5.5 shows the comparison of the IL film before and after the sample was re-heated. Figure 5.5(a) is the topography image of the original IL film which is the same as Figure 5.2(a). After the sample was placed on a hotplate at 100°C for 30 seconds, some of the [Bmim][Cl] ion pairs flowed away and left the residues behind (Figure 5.5(b)). The shape of the residual layer appears the same shape as the standing-up layer in

Figure 5.5(a). In addition, thickness of the parallel layer is 2.20±0.10 nm, which is similar to the thickness before the re-heating. Therefore, I speculate the parallel layers did not change during the re-heating.

In addition to the residues, small patches of the standing-up layers still remain in their original places. The height distribution of the same region measured in Figure 5.2 (lighted in green box in Figure 5.5(b)) is shown in Figure 5.5(d). In the previous section, the thickness of the standing-up layer is measured to be 3.9±0.8 nm. Here, the thickness of the residual layer is 0.9±0.4 nm and the patches of the standing-up layers are 3.2±0.9 nm above the parallel layers. Thus, 0.7 nm thick [Bmim][Cl] ion pairs flowed away during the re-heating.

Further investigation of the structures of the IL standing-up layers shows the thickness of the standing-up monolayer is about 1.0 nm. Figure 5.5(e) shows the terraced structure of the standing-up layers. The height profile indicates that the standing-up layers have three terraces. The bottom film is 3.4±0.2 nm thick, the middle one is 1.3±0.3 nm thick, and the top film is 2.9±0.2 nm thick. Since the length the [Bmim] cation is estimated to be 1.08nm,[152] I speculate the 1.3 nm thick film is composed of one layer of [Bmim][Cl] dimers, and both 2.9 nm and 3.4 nm films are composed of three layers of [Bmim][Cl] dimers where each layer is about 1.0 nm thick. By analyzing 10 other [Bmim][Cl] films, the average thickness of the standing-up monolayer of [Bmim][Cl] is 1.0±0.2 nm. Therefore, for the standing-up layers in Figure 5.5(a), there are four layers of IL dimers. After the [Bmim][Cl] ion pairs flowed away, the number of the layers was reduced to three.

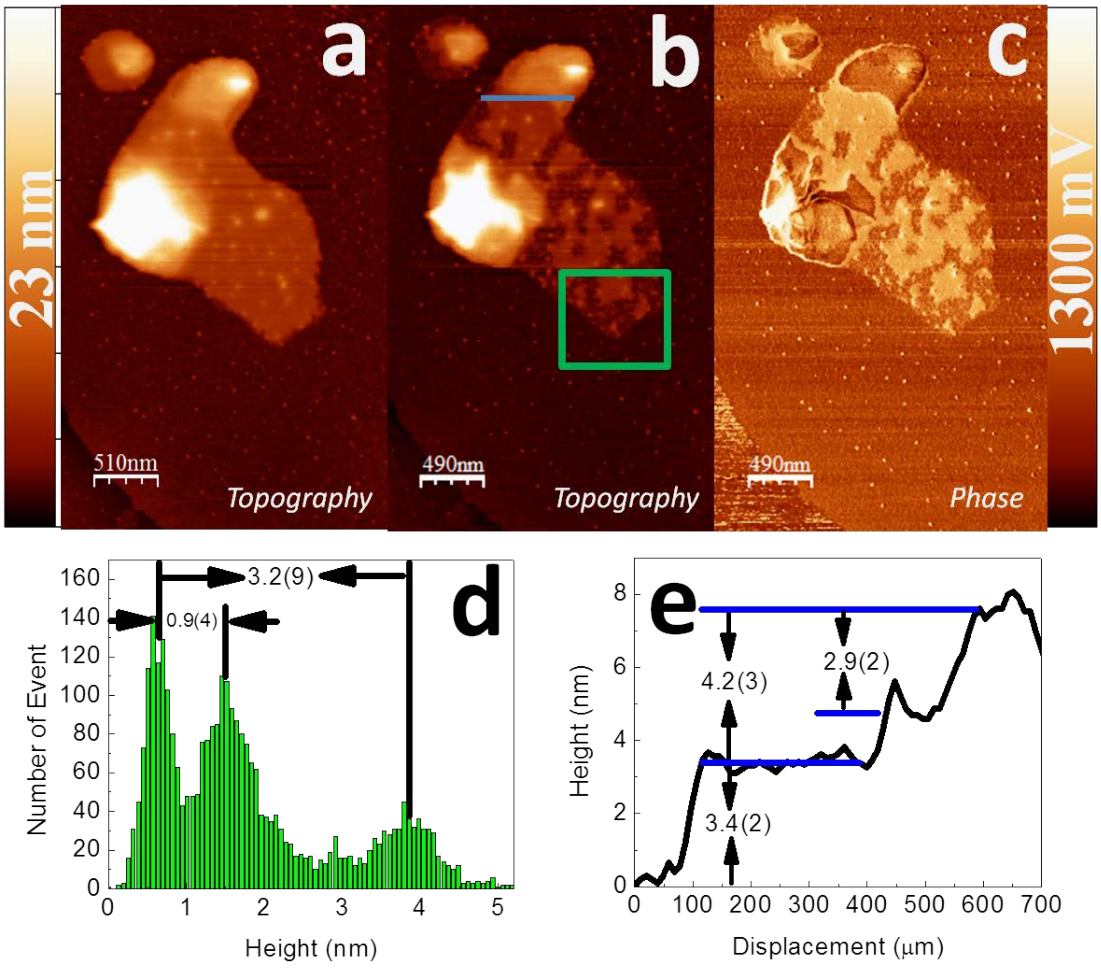

Figure 5.5. Residues are left after [Bmim][Cl] ion pairs flow away. (a) Topography images of the [Bmim][Cl] film over an OTSpd pattern before the re-heating. (b) Topography image of the [Bmim][Cl] film after re-heating. Residues stay on the position which is originally a standing-up layer. (c) Corresponding phase image of (b). (d) Histogram of the area highlighted in (b). The standing-up patches are 3.2±0.9 nm above the parallel layers, and the residual layer is 0.9±0.4 nm above the parallel layer. (e) Height profile along the blue line in (b).

The phase signals of the residues indicate the origin and the orientation of the molecules. The phase signals of the standing-up layers are 0.39±0.04 V, which is the same as the OTS surface, while the phase signals of the residues are only 0.15±0.09 V, which is 0.14 V lower than those of the OTS surface. Furthermore, the phase signals of the residues are not the same as the parallel layer, either. The phase signals of the parallel layers are -0.02±0.05 V, which is 0.17 V lower than those of the residues. If the residual molecules are lying down parallel to the surface, the phase signals should be the same as the parallel layer. In addition, the thickness of the residual layer is similar to the thickness of a standing-up monolayer. Therefore, I speculate the residual molecules are from the standing-up layers. The decrease of the phase signals may be caused by surface roughness and the exposure of the imidazolium functional groups.

5.3.3 Conclusions

[Bmim][Cl] films over the OTSpd surface follow the bilayer structure that standing-up layers sit on top of the parallel layers, as illustrated in Figure 5.6. In the parallel layers, the methylimidazolium ring lies parallel to the OTSpd surface. In the standing-up layer, [Bmim][Cl] ion pairs are aligned with their butyl groups alternately and expose their methyl groups uppermost. The thickness of each standing-up layer is 1.0±0.2nm.

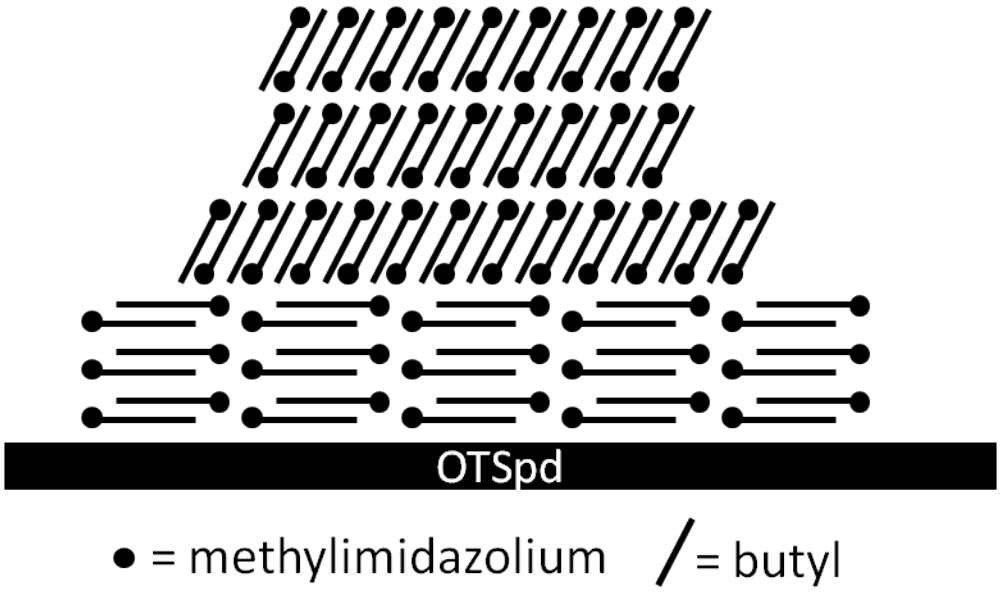

Figure 5.6. Illustration of [Bmim][Cl] bilayer structure over OTSpd surface

5.4 Vapor phase transport of [Bmim][Cl] ion pairs

5.4.1 Methods and experiments

The study of the vapor transport of [Bmim][Cl] ion pairs follows the same procedure as the vapor phase transport of C36 shown in Figure 5.6. First, the [Bmim][Cl] ion pairs were dip-coated in an OTSpd pattern. Satellite OTSpd patterns were fabricated at the place 8-20 μm away from the [Bmim][Cl] ion pairs. After the main OTSpd pattern was fabricated enclosing the [Bmim][Cl] drop, the sample was heated on a hotplate at 100 °C for 60 seconds. The spread [Bmim][Cl] films were characterized with AFM in tapping mode.

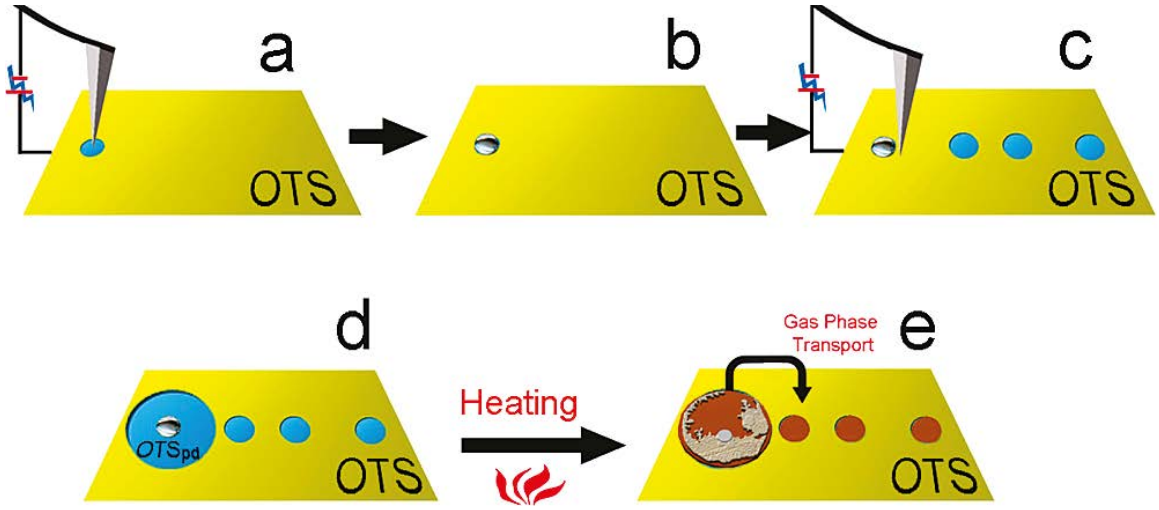

Figure 5.7. Scheme of the study of the vapor phase transport of the IL compounds. (a) Fabrication of a small OTSpd pattern. (b) Dip-coat [Bmim][Cl] ion pairs into the pattern. (c) Fabricate satellite patterns 8μm-20μm away from the [Bmim][Cl] source. (d) A longer pulse is applied to fabricate the main pattern enclosing the [Bmim][Cl] source. (e) The sample is heated at 100 °C for 60 seconds to let [Bmim][Cl] ion pairs spread out. The molecules transport through their vapor phase will condense on the satellite OTSpd patterns. The results are characterized with AFM in tapping mode.

5.4.2 Results and discussion

5.4.2.1. [Bmim][Cl] transport to satellite OTSpd patterns via its vapor phase

Figure 5.8 shows the topography of the sample surface that contains a main OTSpd pattern and two satellite patterns. All the patterns show positive height contrasts, indicating [Bmim][Cl] ion pairs are condensed over the patterns. Since the [Bmim][Cl] ion pairs only exist in the main pattern originally and the [Bmim][Cl] ion pairs cannot flow on the OTS surface, the molecules in the satellite patterns must come from the main pattern through vapor-phase transport.

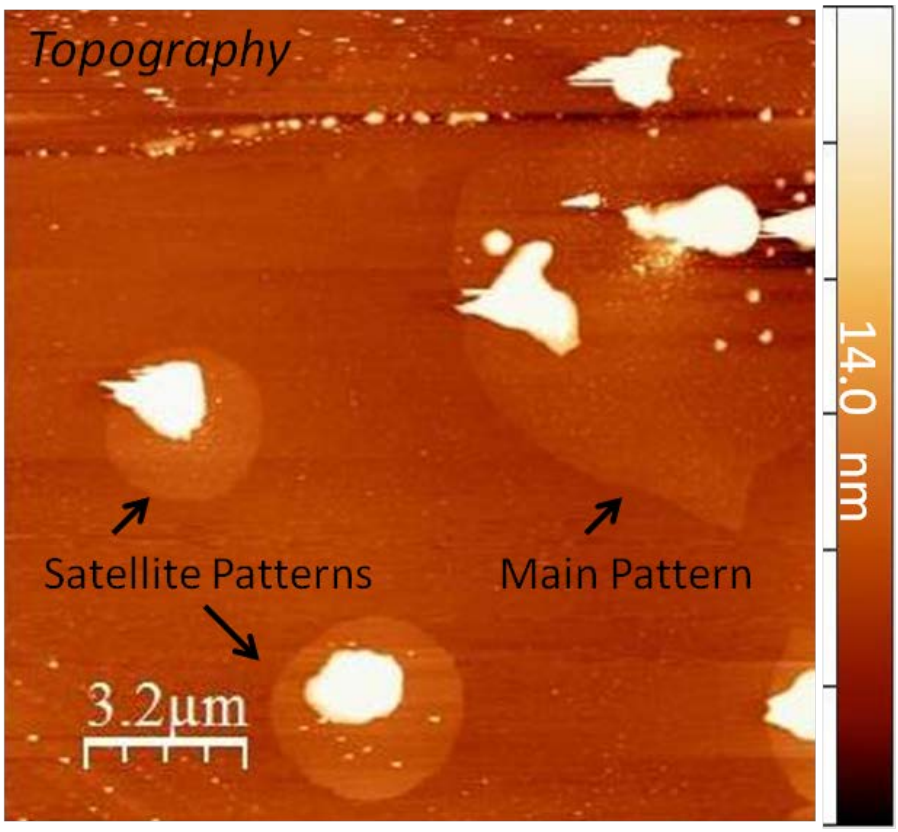

Figure 5.8. Topography image of vapor phase transport of [Bmim][Cl] over OTSpd patterns.

The satellite OTSpd at the bottom of Figure 5.8 is expanded in Figure 5.9. According to the histogram of the area highlighted in the blue square in Figure 5.8(a), the height of the parallel layer of the satellite pattern is 1.5nm above the OTS surface and the thickness of the standing-up layer is 5.3 nm. Therefore, the [Bmim][Cl] film in the satellite pattern contains 5 standing-up layers and a 2.7 nm thick parallel layer. Furthermore, after the sample was re-heated, the standing-up layers flowed back and left residues, as shown in Figure 5.9(b). The shape of the residual layer is the same as the

standing-up layer, indicating the existence of the standing-up layer before re-heating. In addition, terrace structured standing-up layers are also observed after re-heating. Therefore, I conclude the structure of the [Bmim][Cl] film over the satellite patterns is similar to the structure of the [Bmim][Cl] film over the main pattern. The molecules filling in the satellite patterns are [Bmim][Cl] which is the same as the molecules in the main pattern.

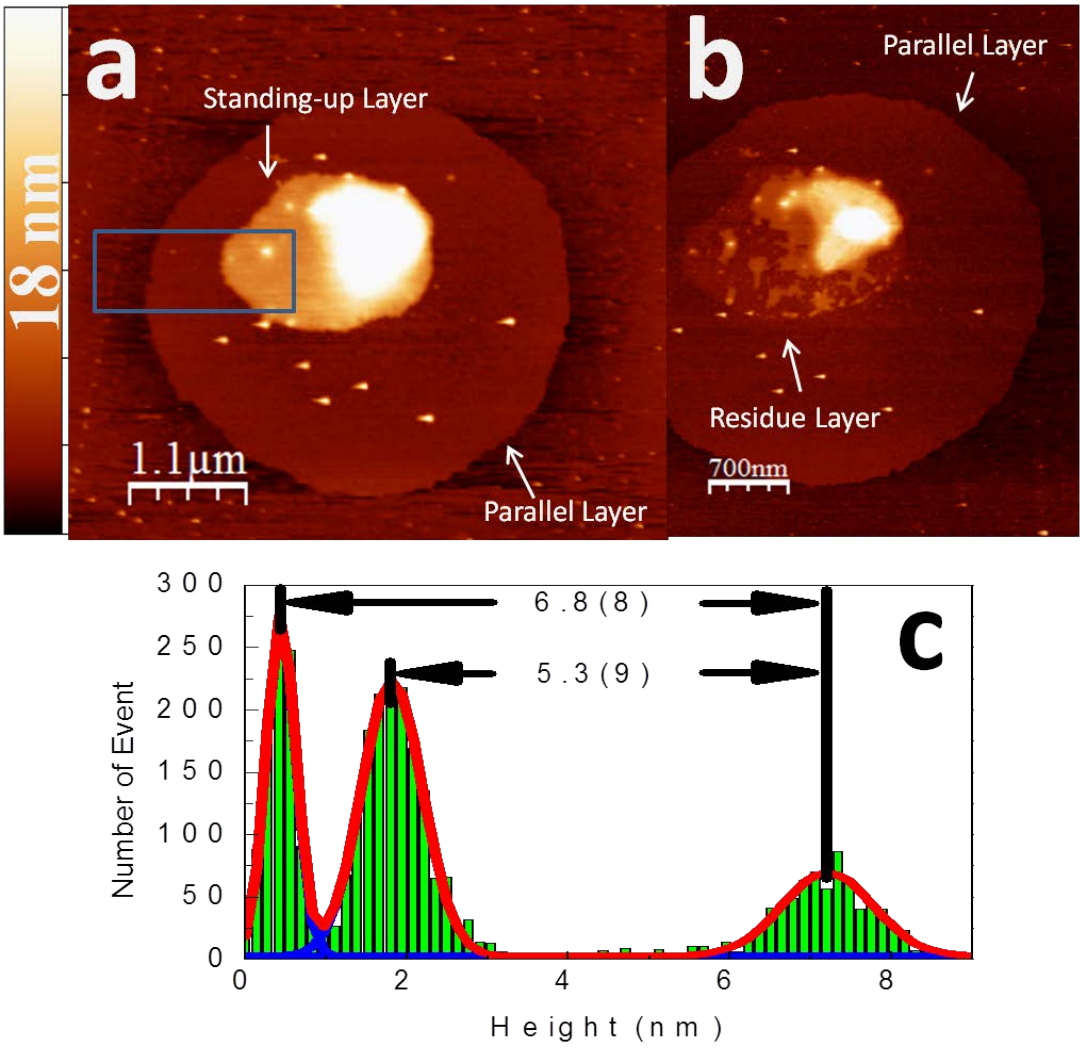

Figure 5.9. [Bmim][Cl] film over OTSpd satellite patterns. (a) Topography image of the [Bmim][Cl] film over OTSpd satellite pattern. (b) Topography image of the [Bmim][Cl]

film after re-heating. (c) Histogram of the lighted area in (a). The parallel layers are 1.5nm above the OTS surface and the standing-up layers are 5.3nm thick.

5.4.3 Conclusions

The vapor phase transport of [Bmim][Cl] ion pairs is studied on the OTSpd patterned surfaces. [Bmim][Cl] ion pairs in the main OTSpd pattern can only transport to the satellite patterns through their vapor. Since [Bmim][Cl] ion pairs are the only liquid compounds. The film found in the satellite patterns must be [Bmim][Cl] film. By comparing the structure of the film in the satellite pattern and the main pattern, the vapor phase transport is also confirmed.

5.5 The orientation of the [Bmim][Cl] ion pairs is influenced by the surface substrates

5.5.1 Methods and experiments

The preparation of the patterned surface that has both positively charged patterns and negatively charged patterns requires two steps: fabricating fresh OTSpd patterns and converting negatively charged OTSpd patterns to positively charged Zn^{2+} patterns. Figure 5.10 illustrates the scheme of the study of the [Bmim][Cl] ion pairs influenced by surface substrates. OTSpd patterns were first fabricated on an OTS SAM coated silicon(100) wafer by local probe oxidation lithography. Next, the sample was incubated in a 5 mM $ZnCl_2$ solution for 10 hours. $ZnCl_2$ salts adsorbed on the patterned surface converted the carboxylic acid surfaces to $ZnCl_2$ surfaces (denoted as OTSpd-Zn pattern). Since the Zn^{2+} cation was divalent, the surface charge changed as it was bound with carboxylic acid

groups. Similar methods were reported to convert a negatively charged mica surface to a positively charged surface, so that negatively charged DNA strands were immobilized.[153] The subsequent step was to fabricate fresh OTSpd patterns close to the OTSpd-Zn patterns. Therefore, the positively charged patterns and the negatively charged patterns were prepared on the same surface and were ready for further use.

The deposition of the molecules on the charged patterns was through vapor phase transport. 0.05mL melt chemicals, C36, [Bmim][Cl], or [Bmim][Tf_2N] was placed 0.5 cm away from the their patterned samples. After heated at 100 °C for 20 minutes, the samples were gradually cooled down to room temperature. Finally the frictional measurements were used to confirm the deposition of the molecules. The calibration of the spring constant and torsion spring constant of the cantilever followed Sader's method.[127-129] The [Bmim][Cl] films over patterned surfaces were characterized with AFM in tapping mode to identify the influence of the molecular polarity due to the surface charges.

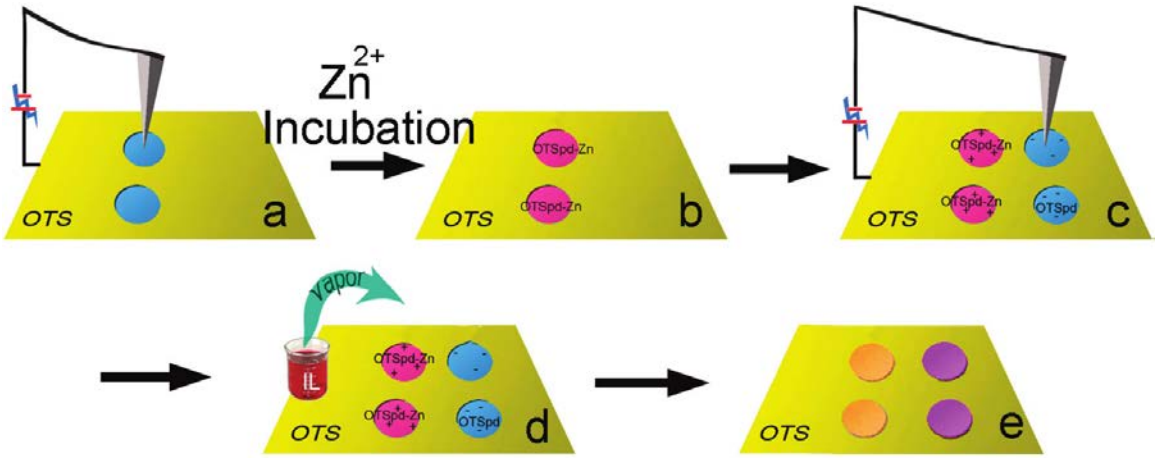

Figure 5.10. Scheme of vapor deposition of [Bmim][Cl] ion pairs over OTSpd patterns and OTSpd-Zn patterns. (a) Fabrication of OTSpd patterns on OTS SAM coated wafer.

(b) The sample wafers are incubated in 5 mM $ZnCl_2$ solution for 10 hours. After removing the sample from the solution and completely rinsing sample with deionized water, Zn^{2+} is bound on the OTSpd surface. (c) Further fabrication of OTSpd patterns by local probe oxidation lithography. The OTSpd-Zn patterns are illustrated in pink, and the OTSpd patterns are illustrated in blue. (d) [Bmim][Cl] ion pairs deposited over the patterns through their vapor phase. (e) [Bmim][Cl] adsorbates over different patterns. Organic patterns indicate [Bmim][Cl] ion pairs over OTSpd-Zn surfaces, denoted as OTSpd-Zn-IL, and purple patterns indicate [Bmim][Cl] ion pairs over OTSpd surfaces, denoted as OTSpd-IL.

5.5.2 Results and discussion

5.5.2.1. Frictional measurements confirm the vapor deposition of [Bmim][Cl] ion pairs

The OTS surface has low affinity to most adsorbates due to its low surface tension. None of the topography images and phase images show any changes before and after the vapor deposition of C36 and ILs. The difference of the adsorption of the molecules over OTSpd pattern and OTSpd-Zn pattern is still unknown. In order to confirm the adsorption of the molecules over the patterns, here, I employed frictional measurements. The AFM tip used for frictional measurement is made of silicon. During the contact mode scan, the molecules on the sample surfaces, either alkane with low surface tension or ILs with charges, may be adsorbed onto the tip. Therefore, when the tip scans through the OTS surface, the friction changes from silicon tip-OTS interaction to adsorbates-OTS interaction. Consequently, the COFs of the OTS surfaces change due to different

adsorbates. Since the AFM tip picked up molecules only from sample surfaces, by comparing the COFs of different molecules over OTS surface, the adsorption can be detected.

Table 5.1. Coefficients of friction of compounds over different surfaces

	COF of OTS Surface	**COF of OTSpd Surface**	**COF of OTSpd-Zn Surface**
Fresh Surface	0.077(6)	0.39(13)	0.38(3)
n-Hexatriacontane	0.060(5)	0.159(12)	0.136(11)
[Bmim][Cl]	0.045(4)	0.260(11)	0.289(13)
[Bmim][Tf_2N]	0.034(3)	0.118(13)	0.090(8)

Table 5.1 lists the COFs of C36, [Bmim][Cl] and [Bmim][Tf_2N] over OTS surface, OTSpd surface and OTSpd-Zn surface, along with the COFs of the all the clean surfaces measured with a CSC/17 uncoated silicon tip. As the reference, the COF of the fresh OTS surface is 0.077±0.006, which is similar to the value that I reported in the previous chapter. Therefore, the COFs of the clean OTSpd surface and OTSpd-Zn surface which are 0.39±0.13 and 0.38±0.03 respectively are used to serve as the references.

First of all, the COFs of C36 and both ILs, [Bmim][Cl] and [Bmim][Tf_2N] are all smaller than that of the clean OTS surface, indicating the adsorption of the molecules on the sample surface. Molecules adsorbed on the AFM tip convert the silicon/OTS interaction to organic molecules/OTS interaction, which results in different friction. Molecules either condensed on the OTS surface during the vapor phase transport or falling off the AFM tip during the scan may also change the friction. Therefore, the COFs of the molecules on the OTS surface are reduced.

The COFs of the adsorbates on both OTSpd surface and OTSpd-Zn surface do not show significant difference, indicating the surfaces of both charged patterns are covered with same materials. For the fresh patterned surfaces, different substrates should ideally have different COF. However, the similarity of the COFs of the fresh OTSpd surface and OTS-Zn surface implies the patterned surfaces are covered with the same material. Since during the fabrication of OTSpd patterns, the sample wafer was kept in the environment of 100% relative humidity, water molecules were condensed over the patterns. As a result, the capillary force from water meniscus dominates the frictional measurements. The COFs between the adsorbates follow the trend, fresh surface > [Bmim][Cl] > C36 > [Bmim][Tf_2N]. All the adsorbates show the effects of frictional reduction on the patterns. [Bmim][Cl] has the least effect, while [Bmim][Tf_2N] is most effective. Since the anchored molecules normally show higher friction,[154] the trend of COFs implies that [Bmim][Cl] has a strong interaction with the charged surfaces. The fluorine atoms on the [Tf_2N] anion, known as the anti-friction agent,[155] reduce the COF of [Bmim][Tf_2N], even though [Bmim][Tf_2N] may also have strong interactions with the pattern.

In summary, ionic liquid molecules deposit on both OTSpd patterns and OTSpd-Zn patterns through their vapor phase.

5.5.2.2. [Bmim][Cl] ion pairs over OTSpd patterns and OTSpd-Zn patterns have different orientation

The OTSpd patterns and the OTSpd-Zn patterns are terminated with carboxylic acid group and Zn^{2+}, respectively. By Kelvin Probe Force Microscopy, Zhang found the surfaces have different surface potentials in that OTSpd surface is 53±14 mV and

OTSpd-Zn surface is 62±8 mV with respect to OTS surface.[156] Such differences in surface potentials indicate the patterns also possess different surface dipoles.[157] Since ILs also possess distinct dipoles and charges, the adsorption of the IL molecules may also be impacted. In other words, the dipole-dipole and charge-dipole interaction between the IL molecules and the patterned surfaces may lead to the change of the orientation of the adsorbates.

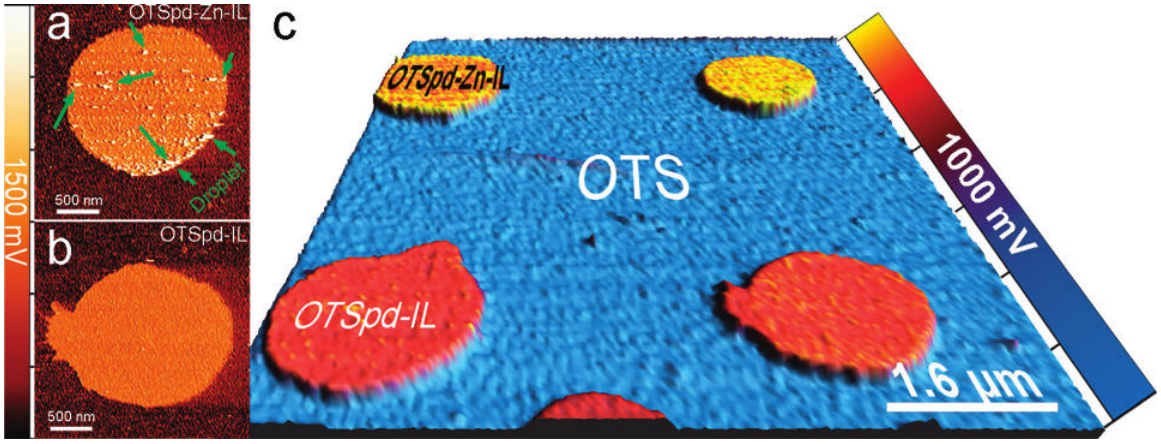

Figure 5.11. [Bmim][Cl] is adsorbed over OTSpd patterns and OTSpd-Zn patterns. (a) Phase image of [Bmim][Cl] ion pairs adsorbed over OTSpd-Zn surface which is the upper right pattern in (c). (b) Phase image of [Bmim][Cl] ion pairs adsorbed over OTSpd surface which is the bottom right pattern in (c). (c) 3D phase image of the [Bmim][Cl] ion pairs over both OTSpd-Zn patterns and OTSpd patterns where OTSpd-Zn-IL has higher phase signals than the OTSpd-IL surface.

Figure 5.11 shows the difference of the phase signals of [Bmim][Cl] adsorbed over OTSpd patterns and OTSpd-Zn patterns. Generally, phase signals of different samples are not used for comparison due to their extremely sensitivity to the change of environments.

However, here, I fabricate both OTSpd patterns and OTSpd-Zn patterns on the same surface and employ the same AFM tip so that the difference of the phase signals between the OTSpd-Zn-IL surface and the OTSpd-IL surface indicate the different orientations of the IL molecules over the patterns. I found the surfaces of adsorbed [Bmim][Cl] ion pairs were flat over OTSpd patterns, while small drops were aggregated on OTSpd-Zn surfaces. Since all the patterns experience the same exposure level of [Bmim][Cl] ion pairs, those drops imply that OTSpd-Zn surface has higher affinity to [Bmim][Cl] ion pairs. By extending the exposure time, more drops are found on the OTSpd-Zn surface, while the thickness of the IL layer remains the same.

5.5.3 Conclusions

The IL molecules transport to the OTSpd patterns through vapor phase not only within the same sample wafer, but also from the source out of the wafer. In this section, I employ the frictional measurements to confirm the vapor deposition of [Bmim][Cl] ion pairs. By changing the surface dipoles of the solid substrates, [Bmim][Cl] ion pairs are also found oriented in different directions.

5.6 Summary of this chapter

The interfacial interactions of ILs play an important role in their applications. In this chapter, a representative ionic liquid, [Bmim][Cl], is spread over OTSpd surface. The precursor film of [Bmim][Cl] follows bilayer structure that standing-up layers sit on top of the parallel layers. In the parallel layers, the methylimidazolium ring is rotated and shares the same plane with its butyl group. Therefore, the molecules lie parallel to the

OTSpd surface. In the standing-up layer, [Bmim][Cl] ion pairs are aligned with their butyl groups alternately and expose their methyl groups uppermost. The thickness of the standing-up layer is 1.0±0.2 nm.

Due to the nature of IL salts, the condensation through the vapor phase transport is normally ignored. However, by using satellite OTSpd patterns, [Bmim][Cl] ion pairs are found transported through their vapor phase. The molecules could deposit to the patterns from the source 0.5cm away.

Finally, different surfaces have different impacts to [Bmim][Cl] ion pairs. [Bmim][Cl] shows different orientation on the surfaces with different dipoles. The Zn^{2+} covered surface has more affinity to the [Bmim][Cl] ion pairs.

Chapter Six

CONCLUSIONS AND FUTURE WORKS

6.1 Conclusions

Spreading is a fundamental phenomenon involved in lubrication, painting and coating. The formation of a precursor film changes the spreading process, from a liquid wetting a solid substrate to a liquid wetting its own film. Understanding the mechanism and the structure of the precursor film helps improve the developments of wetting-related applications.

In this dissertation, organic molecules were spread over engineered octadecyltrichlorosilane partially degraded (OTSpd) patterns, including: n-hexatriacontane (C36) spreading over OTSpd surfaces (Chapter 4) and 1-butyle-3-methylimidazolium chloride ([Bmim][Cl]) spreading over OTSpd surfaces (Chapter 5). The spreading results of these molecules represent the behavior of volatile compounds and non-volatile compounds during the spreading.

The main achievements of this dissertation reveal the structures, contribution of vapor phase transport, and stabilities of the precursor films. They are summarized as the following:

- The precursor films of both C36 and [Bmim][Cl] over an OTSpd surface follow the bilayer model that the standing-up layers sit on top of the parallel layers. Particularly for C36, right on the OTSpd surface, C36 molecules lay their carbon backbones parallel to the surface and form 1-5 layers. Above the parallel layer,

C36 molecules are densely packed side by side. The molecules either stand perpendicularly to the surface or tilt at certain angles. For [Bmim][Cl], in the parallel layers, [Bmim][Cl] ion pairs lay their imidazolium rings parallel to the surface. Each standing-up layer is found to be 1nm thick and is terminated with methyl group.

- Not only does the volatile compound, C36, transport through the vapor phase during the spreading, but the non-volatile compound, [Bmim][Cl], also transports through the vapor phase. The precursor films condensed from the vapor have the same structures as the film formed by liquid. The parallel layers of C36 are primarily formed by vapor condensation and the expansion of its liquid proceeds afterward.
- The parallel layers do not flow with the standing-up layers. C36 residues form on the parallel layers after the standing-up layers flow away. The residual layer keeps the same shape and position as the standing-up layer. For C36, the residual layer does not move with the expansion of the parallel layers, indicating the parallel layers of C36 are thermally stable.
- [Bmim][Cl] ion pairs adsorbed on the surfaces which have different dipoles have different orientations.
- The C36 standing-up layer whose molecules tilt 40° to the surface norm can withstand up to 0.49 GPa pressure and the coefficient of fiction below 0.49GPa is 0.089, which is smaller than the coefficient of friction of alkanethiol and silane self-assembly membranes.

6.2 Future works

The purpose of this dissertation is to understand the interfacial structures and the mechanisms of the precursor films so that future developments involving wetting process may benefit from it. To thoroughly study the properties of the precursor films, more work needs to be done. Further study of the precursor films includes, but should not be limited to the following sections.

6.2.1 Frictional study of C36 standing-up layer

The frictional properties of C36 standing-up layers are important for its application in micro-electro mechanical system (MEMS). Previously, I have reported the coefficient of friction (COF) and critical penetration pressure of a C36 standing-up layer where the molecules tilt 40° to the surface norm. However, in a standing-up layers, C36 molecules could tilt at four different angles which are 0°, 29.25°, 40° or 48.24° to the surface norm. The frictional properties of the remaining three C36 standing-up layers where the molecules tilt 0°, 29.25° and 48.24° have not been studied yet. In further works, the C36 standing-up layers where molecules tilt 0°, 29.25° and 48.24° to the surface norm could be prepared by spreading C36 molecules over OTSpd surfaces. By conducting the same experiment in chapter 4.6, I will explore the mechanical properties of the C36 standing-up layers and find the relationship between the critical penetration pressure and the tilting angles. Therefore, a complete picture of the mechanical properties of the C36 standing-up layers would be discovered.

6.2.2 Kinetic study of vapor phase mass transport

Previously, I have found that both C36 molecules and [Bmim][Cl] ion pairs in the vapor were adsorbed over OTSpd patterns. The sizes of the standing-up layers were enlarged with respect to time. However, the kinetics of such adsorption have not been systematically studied yet.

In the future, the adsorption of both molecules will be thoroughly studied with respect to time, distance, and temperature. The corresponding adsorption constant, diffusion constant, and enthalpy of the adsorption will be found.

6.2.3 Study of competitive adsorption of n-hexatriacontane and 1-butyle-3-methylimidazolium chloride over OTSpd patterns

The wetting process is widely involved in a lot of applications, such as painting and lubrication. Generally, a lubricant is composed of a base oil and additives. During the lubrication, both the base oil and the additives are adsorbed over the solid surface. More importantly, the adsorbed additives react with the solid substrate to form a hard boundary film which reduces the wear.

According to my research, long-chain alkane, n-hexatriacontane (C36), could form parallel layers over the OTSpd surface at the temperature below its melting point. As a result, the parallel layers of C36 molecules cover the solid substrate and inhibit the direct contact of solid substrate with other molecules. Since the base oil of a lubricant is made of hydrocarbons that are similar to C36, the parallel layers of the base oil could also form over the solid substrate. Understanding how the additives penetrate the parallel layers of base oil and are adsorbed over the solid substrate may help improve the lubricants.

In the future research, I will use C36 and [Bmim][Cl] to simulate the base oil and the additives, respectively. Both molecules will be mixed and spread over the same OTSpd patterns. By comparing the films, the behaviors of the mixed molecules over the OTSpd surfaces are expected to be explored. Furthermore, I will use the residues over the parallel layers to investigate the behavior of [Bmim][Cl] ion pairs over the parallel layers of C36.

Reference

1. Degennes, P. G. *Rev Mod Phys* **1985,** 57, (3), 827-863.
2. Young, T. *Philos. Trans. R. Soc. London* **1805,** 95, 65-87.
3. Bonn, D.; Eggers, J.; Indekeu, J.; Meunier, J.; Rolley, E. *Rev Mod Phys* **2009,** 81, (2), 739-805.
4. Popescu, M. N.; Oshanin, G.; Dietrich, S.; Cazabat, A. M. *J Phys-Condens Mat* **2012,** 24, (24).
5. Hardy, W. B. *Philos Mag* **1919,** 38, (223), 49-55.
6. Deryagin, B. *Zh. Fiz. Khim.* **1940,** 14, 137.
7. Deryagin, B. *Kolloidn. Zn.* **1955,** 17, 191.
8. Dzyaloshinskii, I. E.; Lifshitz, E. M.; Pitaevskii, L. P. *Adv Phys* **1961,** 10, (38), 165-209.
9. Bascom, W. D.; Cottington, R. L.; Singleterry, C. R. *Contact Angle, Wettability, and Adhesion* **1964**, 355.
10. Ausserre, D.; Picard, A. M.; Leger, L. *Phys Rev Lett* **1986,** 57, (21), 2671-2674.
11. de Gennes, P. G. *C. R. Acad. Sci.* **1983,** 297 II, 9.
12. Heslot, F.; Fraysse, N.; Cazabat, A. M. *Nature* **1989,** 338, (6217), 640-642.
13. Lazar, P.; Schollmeyer, H.; Riegler, H. *Phys Rev Lett* **2005,** 94, (11), 116101.
14. Cazabat, A. M.; Fraysse, N.; Heslot, F. *Colloid Surface* **1991,** 52, (1-2), 1-8.
15. Hayes, R.; Borisenko, N.; Tam, M. K.; Howlett, P. C.; Endres, F.; Atkin, R. *J Phys Chem C* **2011,** 115, (14), 6855-6863.
16. Bangham, D. H.; Saweris, Z. *T Faraday Soc* **1938,** 34, (1), 0554-0569.
17. Bahadur, P.; Yadav, P. S.; Chaurasia, K.; Leh, A.; Tadmor, R. *J Colloid Interf Sci* **2009,** 332, (2), 455-460.
18. Novotny, V. J.; Marmur, A. *J Colloid Interf Sci* **1991,** 145, (2), 355-361.
19. Degennes, P. G. *Cr Acad Sci Ii* **1984,** 298, (4), 111-115.
20. Schmidt, J. W.; Moldover, M. R. *J Chem Phys* **1983,** 79, (1), 379-387.
21. Joanny, J. F.; Degennes, P. G. *J Phys-Paris* **1986,** 47, (1), 121-127.
22. Churaev, N. V.; Starov, V. M.; Derjaguin, B. V. *J Colloid Interf Sci* **1982,** 89, (1), 16-24.
23. Oron, A.; Davis, S. H.; Bankoff, S. G. *Rev Mod Phys* **1997,** 69, (3), 931-980.
24. AlaNissila, T.; Herminghaus, S.; Hjelt, T.; Leiderer, P. *Phys Rev Lett* **1996,** 76, (21), 4003-4006.
25. Lopez, J.; Miller, C. A.; Ruckenstein, E. *J Colloid Interf Sci* **1976,** 56, (3), 460-468.
26. Joanny, J. F. *J Mec Theor Appl* **1986**, 249-271.
27. Lukkarinen, A.; Kaski, K.; Abraham, D. B. *Phys Rev E* **1995,** 51, (3), 2199-2202.
28. Deconinck, J.; Hoorelbeke, S.; Valignat, M. P.; Cazabat, A. M. *Phys Rev E* **1993,** 48, (6), 4549-4555.
29. Deconinck, J.; Fraysse, N.; Valignat, M. P.; Cazabat, A. M. *Langmuir* **1993,** 9, (7), 1906-1909.
30. Yang, J. X.; Koplik, J.; Banavar, J. R. *Phys Rev Lett* **1991,** 67, (25), 3539-3542.
31. Yang, J. X.; Koplik, J.; Banavar, J. R. *Phys Rev A* **1992,** 46, (12), 7738-7749.
32. Deconinck, J.; Dortona, U.; Koplik, J.; Banavar, J. R. *Phys Rev Lett* **1995,** 74, (6), 928-931.

33. DOrtona, U.; DeConinck, J.; Koplik, J.; Banavar, J. R. *Phys Rev E* **1996,** 53, (1), 562-569.
34. Haataja, M.; Nieminen, J. A.; Alanissila, T. *Phys Rev E* **1995,** 52, (3), R2165-R2167.
35. Beaglehole, D. *J Phys Chem-Us* **1989,** 93, (2), 893-899.
36. Binnig, G.; Quate, C. F.; Gerber, C. *Phys Rev Lett* **1986,** 56, (9), 930-933.
37. Drevillon, B.; Perrin, J.; Marbot, R.; Violet, A.; Dalby, J. L. *Rev Sci Instrum* **1982,** 53, (7), 969-977.
38. Heslot, F.; Cazabat, A. M.; Levinson, P. *Phys Rev Lett* **1989,** 62, (11), 1286-1289.
39. Heslot, F.; Cazabat, A. M.; Fraysse, N. *J Phys-Condens Mat* **1989,** 1, (33), 5793-5798.
40. Heslot, F.; Cazabat, A. M.; Levinson, P.; Fraysse, N. *Phys Rev Lett* **1990,** 65, (5), 599-602.
41. Cazabat, A. M.; Fraysse, N.; Heslot, F.; Levinson, P.; Marsh, J.; Tiberg, F.; Valignat, M. P. *Adv Colloid Interfac* **1994,** 48, 1-17.
42. Bardon, S.; Cachile, M.; Cazabat, A. M.; Fanton, X.; Valignat, M. P.; Villette, S. *Faraday Discuss* **1996,** 104, 307-316.
43. Dorset, D. L.; Snyder, R. G. *J Phys Chem* **1996,** 100, (23), 9848-9853.
44. Wu, X. Z.; Ocko, B. M.; Sirota, E. B.; Sinha, S. K.; Deutsch, M.; Cao, B. H.; Kim, M. W. *Science* **1993,** 261, (5124), 1018-1021.
45. Wu, X. Z.; Sirota, E. B.; Sinha, S. K.; Ocko, B. M.; Deutsch, M. *Phys Rev Lett* **1993,** 70, (7), 958-961.
46. Pfohl, T.; Beaglehole, D.; Riegler, H. *Chem Phys Lett* **1996,** 260, (1-2), 82-86.
47. Merkl, C.; Pfohl, T.; Riegler, H. *Phys Rev Lett* **1997,** 79, (23), 4625-4628.
48. Schollmeyer, H.; Ocko, B.; Riegler, H. *Langmuir* **2002,** 18, (11), 4351-4355.
49. Holzwarth, A.; Leporatti, S.; Riegler, H. *Europhys Lett* **2000,** 52, (6), 653-659.
50. Nozaki, K.; Saihara, R.; Ishikawa, K.; Yamamoto, T. *Jpn J Appl Phys 1* **2007,** 46, (2), 761-769.
51. Volkmann, U. G.; Pino, M.; Altamirano, L. A.; Taub, H.; Hansen, F. Y. *J Chem Phys* **2002,** 116, (5), 2107-2115.
52. Mo, H.; Taub, H.; Volkmann, U. G.; Pino, M.; Ehrlich, S. N.; Hansen, F. Y.; Lu, E.; Miceli, P. *Chem Phys Lett* **2003,** 377, (1-2), 99-105.
53. Cai, Y. G. *Langmuir* **2009,** 25, (10), 5594-5601.
54. Bardon, S.; Ober, R.; Valignat, M. P.; Vandenbrouck, F.; Cazabat, A. M.; Daillant, J. *Phys Rev E* **1999,** 59, (6), 6808-6818.
55. Ma, X.; Gui, J.; Smoliar, L.; Grannen, K.; Marchon, B.; Bauer, C. L.; Jhon, M. S. *Phys Rev E* **1999,** 59, (1), 722-727.
56. Xu, H.; Shirvanyants, D.; Beers, K.; Matyjaszewski, K.; Rubinstein, M.; Sheiko, S. S. *Phys Rev Lett* **2004,** 93, (20).
57. Endres, F.; Freyland, W. *J Phys Chem B* **1998,** 102, (50), 10229-10233.
58. Gasparotto, L. H. S.; Borisenko, N.; Bocchi, N.; El Abedin, S. Z.; Endres, F. *Phys Chem Chem Phys* **2009,** 11, (47), 11140-11145.
59. Gnahm, M.; Pajkossy, T.; Kolb, D. M. *Electrochim Acta* **2010,** 55, (21), 6212-6217.

60. Mezger, M.; Schroder, H.; Reichert, H.; Schramm, S.; Okasinski, J. S.; Schoder, S.; Honkimaki, V.; Deutsch, M.; Ocko, B. M.; Ralston, J.; Rohwerder, M.; Stratmann, M.; Dosch, H. *Science* **2008,** 322, (5900), 424-428.
61. Yokota, Y.; Harada, T.; Fukui, K. I. *Chem Commun* **2010,** 46, (45), 8627-8629.
62. Zhang, X.; Zhong, Y. X.; Yan, J. W.; Su, Y. Z.; Zhang, M.; Mao, B. W. *Chem Commun* **2012,** 48, (4), 582-584.
63. Dou, Q.; Sha, M. L.; Fu, H. Y.; Wu, G. Z. *J Phys-Condens Mat* **2011,** 23, (17).
64. Fedorov, M. V.; Lynden-Bell, R. M. *Phys Chem Chem Phys* **2012,** 14, (8), 2552-2556.
65. Rivera-Rubero, S.; Baldelli, S. *J Am Chem Soc* **2004,** 126, (38), 11788-11789.
66. Rivera-Rubero, S.; Baldelli, S. *J Phys Chem B* **2006,** 110, (31), 15499-15505.
67. Rivera-Rubero, S.; Baldelli, S. *J Phys Chem B* **2006,** 110, (10), 4756-4765.
68. Law, G.; Watson, P. R. *Chem Phys Lett* **2001,** 345, (1-2), 1-4.
69. Gannon, T. J.; Law, G.; Watson, P. R.; Carmichael, A. J.; Seddon, K. R. *Langmuir* **1999,** 15, (24), 8429-8434.
70. Bowers, J.; Vergara-Gutierrez, M. C.; Webster, J. R. P. *Langmuir* **2004,** 20, (2), 309-312.
71. Sloutskin, E.; Ocko, B. M.; Tamam, L.; Kuzmenko, I.; Gog, T.; Deutsch, M. *J Am Chem Soc* **2005,** 127, (51), 18333-18333.
72. Carmichael, A. J.; Hardacre, C.; Holbrey, J. D.; Nieuwenhuyzen, M.; Seddon, K. R. *Mol Phys* **2001,** 99, (10), 795-800.
73. Li, L. B.; Groenewold, J.; Picken, S. J. *Chem Mater* **2005,** 17, (2), 250-257.
74. Xie, X. N.; Chung, H. J.; Sow, C. H.; Wee, A. T. S. *Mat Sci Eng R* **2006,** 54, (1-2), 1-48.
75. Klauk, H.; Gundlach, D. J.; Bonse, M.; Kuo, C. C.; Jackson, T. N. *Appl Phys Lett* **2000,** 76, (13), 1692-1694.
76. Fujita, J.; Ohnishi, Y.; Ochiai, Y.; Matsui, S. *Appl Phys Lett* **1996,** 68, (9), 1297-1299.
77. Rennon, S.; Bach, L.; Reithmaier, J. P.; Forchel, A.; Gentner, J. L.; Goldstein, L. *Appl Phys Lett* **2000,** 77, (3), 325-327.
78. Cappella, B.; Sturm, H. *J Appl Phys* **2002,** 91, (1), 506-512.
79. King, W. P.; Kenny, T. W.; Goodson, K. E.; Cross, G.; Despont, M.; Durig, U.; Rothuizen, H.; Binnig, G. K.; Vettiger, P. *Appl Phys Lett* **2001,** 78, (9), 1300-1302.
80. Sugimoto, Y.; Abe, M.; Hirayama, S.; Oyabu, N.; Custance, O.; Morita, S. *Nat Mater* **2005,** 4, (2), 156-U36.
81. Snow, E. S.; Campbell, P. M. *Appl Phys Lett* **1994,** 64, (15), 1932-1934.
82. Li, Y.; Maynor, B. W.; Liu, J. *J Am Chem Soc* **2001,** 123, (9), 2105-2106.
83. Lyuksyutov, S. F.; Vaia, R. A.; Paramonov, P. B.; Juhl, S.; Waterhouse, L.; Ralich, R. M.; Sigalov, G.; Sancaktar, E. *Nat Mater* **2003,** 2, (7), 468-472.
84. Day, H. C.; Allee, D. R. *Appl Phys Lett* **1993,** 62, (21), 2691-2693.
85. Dagata, J. A.; Perez-Murano, F.; Martin, C.; Kuramochi, H.; Yokoyama, H. *J Appl Phys* **2004,** 96, (4), 2386-2392.
86. Siles, P. F.; Archanjo, B. S.; Baptista, D. L.; Pimentel, V. L.; Yang, J. J.; Neves, B. R. A.; Medeiros-Ribeiro, G. *J Appl Phys* **2011,** 110, (2).
87. Sagunova, I. V.; Shevyakov, V. I.; Gavrilov, S. A.; Belov, A. N. *Semiconductors+* **2010,** 44, (13), 1709-1713.

88. Kamada, K.; Hirata, S.; Enomoto, N.; Hojo, J. *Solid State Ionics* **2009,** 180, (20-22), 1226-1230.
89. Pellegrino, L.; Pallecchi, I.; Bellingeri, E.; Canu, G.; Siri, A. S.; Marre, D.; Yanagisawa, Y.; Ishikawa, M.; Matsumoto, T.; Tanaka, H.; Kawai, T. *J Nanosci Nanotechno* **2010,** 10, (7), 4471-4476.
90. Sugimura, H.; Hanji, T.; Hayashi, K.; Takai, O. *Adv Mater* **2002,** 14, (7), 524-526.
91. Maoz, R.; Frydman, E.; Cohen, S. R.; Sagiv, J. *Adv Mater* **2000,** 12, (10), 725-731.
92. Liu, S. T.; Maoz, R.; Sagiv, J. *Nano Lett* **2004,** 4, (5), 845-851.
93. Maoz, R.; Cohen, S. R.; Sagiv, J. *Adv Mater* **1999,** 11, (1), 55-61.
94. Maoz, R.; Frydman, E.; Cohen, S. R.; Sagiv, J. *Adv Mater* **2000,** 12, (6), 424-429.
95. Gao, P.; Cai, Y. G. *Langmuir* **2008,** 24, (18), 10334-10339.
96. Cai, Y. G. *Langmuir* **2008,** 24, (1), 337-343.
97. Brzoska, J. B.; Shahidzadeh, N.; Rondelez, F. *Nature* **1992,** 360, (6406), 719-721.
98. Maoz, R.; Sagiv, J. *J Colloid Interf Sci* **1984,** 100, (2), 465-496.
99. Maoz, R.; Sagiv, J.; Degenhardt, D.; Mohwald, H.; Quint, P. *Supramolecular Science* **1995,** 2, 9-24.
100. Evans, R. D.; More, K. L.; Darragh, C. V.; Nixon, H. P. *Tribol T* **2005,** 48, (3), 299-307.
101. Winn, A. J.; Dowson, D.; Bell, J. C. *Tribol Int* **1995,** 28, (6), 383-393.
102. Winn, A. J.; Dowson, D.; Bell, J. C. *Tribol Int* **1995,** 28, (6), 395-402.
103. Sainbayar, A.; Vosmerikov, A. V.; Nordov, E.; Golovko, A. K. *J Petrol Sci Eng* **2005,** 46, (4), 233-242.
104. Dneprovsky, K. S.; Golovko, A. K.; Lomovsky, O. I.; Vosmerikov, A. V. *Petroleum and Coal* **1999,** 41, 166-168.
105. Peters, B. L.; Lane, J. M. D.; Ismail, A. E.; Grest, G. S. *Langmuir* **2012,** 28, (50), 17443-17449.
106. Qian, H.; Fiedler, N.; Moore, D. F.; Weisel, C. P. *Ann Occup Hyg* **2010,** 54, (4), 417-426.
107. Wu, Z.; Ehrlich, S. N.; Matthies, B.; Herwig, K. W.; Dai, P. C.; Volkmann, U. G.; Hansen, F. Y.; Taub, H. *Chem Phys Lett* **2001,** 348, (3-4), 168-174.
108. Schollmeyer, H.; Struth, B.; Riegler, H. *Langmuir* **2003,** 19, (12), 5042-5051.
109. Basu, S.; Satija, S. K. *Langmuir* **2007,** 23, (16), 8331-8335.
110. Taub, H.; Herwig, K. W.; Matthies, B.; Hansen, F. Y. *Inorg Mater+* **1999,** 35, (8), 847-851.
111. Herwig, K. W.; Matthies, B.; Taub, H. *Phys Rev Lett* **1995,** 75, (17), 3154-3157.
112. Diama, A.; Matthies, B.; Herwig, K. W.; Hansen, F. Y.; Criswell, L.; Mo, H.; Bai, M.; Taub, H. *J Chem Phys* **2009,** 131, (8).
113. Bai, M.; Knorr, K.; Simpson, M. J.; Trogisch, S.; Taub, H.; Ehrlich, S. N.; Mo, H.; Volkmann, U. G.; Hansen, F. Y. *Epl-Europhys Lett* **2007,** 79, (2).
114. Trogisch, S.; Simpson, M. J.; Taub, H.; Volkmann, U. G.; Pino, M.; Hansen, F. Y. *J Chem Phys* **2005,** 123, (15).
115. Van, L. P.; Kyrylyuk, V.; Polesel-Maris, J.; Thoyer, F.; Lubin, C.; Cousty, J. *Langmuir* **2009,** 25, (2), 639-642.
116. Ajaev, V. S. *J Fluid Mech* **2005,** 528, 279-296.
117. Glasner, K. B. *Phys Fluids* **2003,** 15, (7), 1837-1842.

118. Bhushan, B.; Kulkarni, A. V.; Koinkar, V. N.; Boehm, M.; Odoni, L.; Martelet, C.; Belin, M. *Langmuir* **1995,** 11, (8), 3189-3198.
119. Carpick, R. W.; Agrait, N.; Ogletree, D. F.; Salmeron, M. *Langmuir* **1996,** 12, (13), 3334-3340.
120. Flater, E. E.; Ashurst, W. R.; Carpick, R. W. *Langmuir* **2007,** 23, (18), 9242-9252.
121. Horcas, I.; Fernandez, R.; Gomez-Rodriguez, J. M.; Colchero, J.; Gomez-Herrero, J.; Baro, A. M. *Rev Sci Instrum* **2007,** 78, (1).
122. Chowdhury, D.; Maoz, R.; Sagiv, J. *Nano Lett* **2007,** 7, (6), 1770-1778.
123. Tsuzuki, S.; Honda, K.; Uchimaru, T.; Mikami, M. *J Phys Chem A* **2004,** 108, (46), 10311-10316.
124. Schreiber, F. *Prog Surf Sci* **2000,** 65, (5-8), 151-256.
125. Wasserman, S. R.; Whitesides, G. M.; Tidswell, I. M.; Ocko, B. M.; Pershan, P. S.; Axe, J. D. *J Am Chem Soc* **1989,** 111, (15), 5852-5861.
126. McDermott, M. T.; Green, J. B. D.; Porter, M. D. *Langmuir* **1997,** 13, (9), 2504-2510.
127. Green, C. P.; Lioe, H.; Cleveland, J. P.; Proksch, R.; Mulvaney, P.; Sader, J. E. *Rev Sci Instrum* **2004,** 75, (6), 1988-1996.
128. Green, C. P.; Sader, J. E. *J Appl Phys* **2002,** 92, (10), 6262-6274.
129. Sader, J. E.; Chon, J. W. M.; Mulvaney, P. *Rev Sci Instrum* **1999,** 70, (10), 3967-3969.
130. Mandelkern, M.; Elias, J. G.; Eden, D.; Crothers, D. M. *J Mol Biol* **1981,** 152, (1), 153-161.
131. Carpick, R. W.; Ogletree, D. F.; Salmeron, M. *Appl Phys Lett* **1997,** 70, (12), 1548-1550.
132. DelRio, F. W.; Jaye, C.; Fischer, D. A.; Cook, R. F. *Appl Phys Lett* **2009,** 94, (13).
133. Wang, M. J.; Liechti, K. M.; Srinivasan, V.; White, J. M.; Rossky, P. J.; Stone, M. T. *J Appl Mech-T Asme* **2006,** 73, (5), 769-777.
134. Mishra, M.; Egberts, P.; Bennewitz, R.; Szlufarska, I. *Phys Rev B* **2012,** 86, (4).
135. Oleksowicz, S.; Mruk, A. *Tribol T* **2011,** 54, (5), 691-700.
136. Achanta, S.; Drees, D.; Celis, J. P. *Surf Coat Tech* **2008,** 202, (24), 6127-6135.
137. Liu, X. F.; Wang, L. P.; Pu, J. B.; Xue, Q. J. *Appl Surf Sci* **2012,** 258, (20), 8289-8297.
138. Arora, H.; Cann, P. M. *Tribol Int* **2010,** 43, (10), 1908-1916.
139. Yu, B.; Liu, Z. L.; Zhou, F.; Liu, W. M.; Liang, Y. M. *Mater Lett* **2008,** 62, (17-18), 2967-2969.
140. Lee, J. H.; Kang, S. W.; Song, D.; Won, J.; Kang, Y. S. *J Membrane Sci* **2012,** 423, 159-164.
141. Mutelet, F.; Moise, J. C.; Skrzypczak, A. *J Chem Eng Data* **2012,** 57, (3), 918-927.
142. Han, D.; Row, K. H. *Molecules* **2010,** 15, (4), 2405-2426.
143. Castiglione, F.; Ragg, E.; Mele, A.; Appetecchi, G. B.; Montanino, M.; Passerini, S. *J Phys Chem Lett* **2011,** 2, (3), 153-157.
144. Sutto, T. E. *J Electrochem Soc* **2007,** 154, (10), P101-P107.
145. Kobayashi, Y.; Mita, Y.; Seki, S.; Ohno, Y.; Miyashiro, H.; Terada, N. *J Electrochem Soc* **2007,** 154, (7), A677-A681.
146. Tamam, L.; Ocko, B. M.; Reichert, H.; Deutsch, M. *Phys Rev Lett* **2011,** 106, (19).

147. Mezger, M.; Schramm, S.; Schroder, H.; Reichert, H.; Deutsch, M.; De Souza, E. J.; Okasinski, J. S.; Ocko, B. M.; Honkimaki, V.; Dosch, H. *J Chem Phys* **2009,** 131, (9).
148. Atkin, R.; Warr, G. G. *J Phys Chem C* **2007,** 111, (13), 5162-5168.
149. Nakakoshi, M.; Shiro, M.; Fujimoto, T.; Machinami, T.; Seki, H.; Tashiro, M.; Nishikawa, K. *Chem Lett* **2006,** 35, (12), 1400-1401.
150. Ao, M. Q.; Xu, G. Y.; Pang, J. Y.; Zhao, T. T. *Langmuir* **2009,** 25, (17), 9721-9727.
151. Getsis, A.; Mudring, A. V. *Cryst Res Technol* **2008,** 43, (11), 1187-1196.
152. Hu, H.; Martin, J. C.; Xiao, M.; Southworth, C. S.; Meng, Y. Z.; Sun, L. Y. *J Phys Chem C* **2011,** 115, (13), 5509-5514.
153. Hansma, H. G.; Revenko, I.; Kim, K.; Laney, D. E. *Nucleic Acids Res* **1996,** 24, (4), 713-720.
154. Lu, L. B.; Cai, Y. G. *Langmuir* **2011,** 27, (10), 5953-5960.
155. Wang, H. Z.; Lu, Q. M.; Ye, C. F.; Liu, W. M.; Cui, Z. J. *Wear* **2004,** 256, (1-2), 44-48.
156. Zhang, X. N.; Lu, L. B.; Cai, Y. G. *Langmuir* **2012,** 28, (25), 9593-9600.
157. Lu, J.; Delamarche, E.; Eng, L.; Bennewitz, R.; Meyer, E.; Guntherodt, H. J. *Langmuir* **1999,** 15, (23), 8184-8188.

VITA

LINGBO LU

Education:

Sep. 2004-Mar. 2007	**Master of Engineering, Applied Chemistry** Shanghai Jiao Tong University, Shanghai, China
Sep. 2000-Jun. 2004	**Bachelor of Engineering, Chemical Engineering** Shanghai Jiao Tong University, Shanghai, China

Publication:

1. Zhang, Xiaoning; Lu, Lingbo; Cai, Yuguang, Surface Properties of Ionic Liquid Adsorbate Layer Are Influenced by the Dipole of the Underneath Substrate *Langmui*r; **2012**; 28, 9593-9600
2. Liu, Wen; Lu, Lingbo; Li, Yulong; Cai, Yuguang; Sekulic, Dusan. P, Preferential spreading of molten metal over an anisotropically microstructured surface *EPL*; **2012**; 97, 46003
3. Lu, Lingbo; Cai, Yuguang, Molecular Tilting and Its Impact on Frictional Properties of n-Alkane Self-Assembled Monolayers *Langmui*r; **2011**; 27, 5953-5960
4. Lu, Lingbo; Cai, Yuguang *Scanning Probe Microscopy in Nanoscience and Nanotechnology*; **2011**; Chapter 13
5. Lu, Lingbo; Zander, Kari J; Cai, Yuguang, Stability of the parallel layer during alkane spreading and the domain structures of the standing-up layer *Langmuir*; **2010**; 26, 5624-5631
6. Lu, Lingbo; Yuguang Cai, Role of Vapor-Phase Mass Transport During the Spreading of a Long-Chain Alkane Drop *Langmui*r; **2009**; 25, 13914-13917
7. Lu, Lingbo; Liu, Yang; Li, Jingshan, A real-time maintenance scheduling policy in serial production lines **2010**; WCICA
8. Lu, Lingbo; Li, Jingshan; Gisler, Paula, Improving financial performance by modeling and analysis of radiology procedure scheduling at a large community hospital *J. Med. Sys.*; **2009**
9. Lv, Lingbo; Zeng, Xiangqiong; Deng, Yu; Deng, Zhao; Ren, Tianhui, Synthesis and Tribochemical Study of Dimercapto-monoamino-s-triazine Derivatives as Li Grease Additives *Lubrication Engineering* **2006**, *184*, 116-119
10. Wu, Hua; Zeng, Xiangqiong; Lu, Lingbo; Ren, Tianhui, Tribological performance and chemistry of films for di-n-butyl dithiocarbamate derivatives in rapeseed oil *Chinese Science Bulletin*; (English edition) **2007**, *52*, 194-199; (Chinese edition) **2006**, *51*, 2237-2241
11. Wu, Hua; Li, Jing; Yi, Hongling; Zeng, Xiangqiong; Lv, Lingbo; Ren, Tianhui,

The tribological behavior of diester-containing polysulfides as additives in mineral oil *Tribology International* **2007**, *40*, 1246-1252

Lingbo Lu

8/01/2013